ASTROBIOLOGY
Volume 21, Number 1, 2021

DOI: 10.1089/ast.2019.2072

A Reconstructed Subaerial Hot Spring Field in the ~3.5 Billion-Year-Old Dresser Formation, North Pole Dome, Pilbara Craton, Western Australia

Tara Djokic,[1,2] Martin J. Van Kranendonk,[1–4] Kathleen A. Campbell,[5] Jeff R. Havig,[6] Malcolm R. Walter,[1] and Diego M. Guido[7]

Abstract

Recent discoveries of geyserite and siliceous sinter with textural biosignatures in the ~3.5 Ga Dresser Formation of the Pilbara Craton, Western Australia, extended the record of inhabited subaerial hot springs on Earth by ~3 billion years, back to the time when siliceous sinter deposits are known to have formed on Mars (*e.g.*, at Columbia Hills, Gusev Crater). Here, we present more detailed lithostratigraphic, petrographic and geochemical data collected from 100 measured sections across a ~14 km strike length in the Dresser Formation. The data indicate deposition of a wide range of hot spring and associated deposits in a restricted interval that directly overlies a hydrothermally influenced volcanic caldera lake facies, with shoreline stromatolites. Hot spring deposits show abrupt lateral facies changes and include associated channelized clastic deposits that support fluvial, subaerial hot spring deposition. All Dresser hot spring and associated lithofacies have direct analogs with proximal, middle, and distal apron hot spring facies that are characteristic of those from New Zealand, Yellowstone National Park, USA, and Argentina. Rare earth element and yttrium geochemistry shows that the Dresser geyserite shares identical patterns with Phanerozoic hot spring sinters. This geochemical data further supports textural and contextual evidence that indicate the Dresser geyserite formed as a subaerial hot spring sinter. Further, the Dresser hot spring deposits are temporally associated with a diverse suite of textural biosignatures that indicate a thriving microbial community existed within in a Paleoarchean hot spring field. The results presented here underscore the importance of continued study of the early geological record for astrobiological research. In particular these findings reinforce the long-standing hypothesis that hydrothermal systems are optimal places to search for past life on Mars. Key Words: Archean hot springs—Biosignatures—Dresser Formation Pilbara Craton—Western Australia—Mars. Astrobiology 21, 1–38.

1. Introduction

Investigations of the early geological records on Earth help identify potentially habitable environments for early life and, thus, aid in the exploration for life beyond Earth. Recent discoveries of geyserite and siliceous sinter accompanied by textural biosignatures in the ~3.5 Ga Dresser Formation of the Pilbara Craton, Western Australia (Fig. 1), have extended the record of inhabited subaerial hot springs on Earth by ~3 billion years (Djokic *et al.*, 2017). These findings are relevant to the search for life on Mars given that silica deposits interpreted as representing hot spring sinters of similar age to the Dresser deposits have been identified from remote sensing (Skok *et al.*, 2010) and Spirit Rover data (Ruff and Farmer, 2016; Ruff *et al.*, 2020).

[1]Australian Centre for Astrobiology, PANGEA Research Centre, School of Biological, Earth and Environmental Sciences, University of New South Wales, Kensington, New South Wales, Australia.
[2]Australian Research Council Centre of Excellence for Core to Crust Fluid Systems (CCFS), The University of Western Australia, Perth, Western Australia, Australia.
[3]Big Questions Institute, University of New South Wales Australia, Kensington, New South Wales, Australia.
[4]Pheasant Memorial Laboratory, Institute for Planetary Materials, Okayama University, Misasa, Tottori, Japan.
[5]Centre for Fundamental Inquiry, School of Environment and Te Ao Mārama, University of Auckland, Auckland, New Zealand.
[6]Department of Earth Sciences, University of Minnesota, Minneapolis, Minnesota, USA.
[7]CONICET and Facultad de Ciencias Naturales y Museo, Instituto de Recursos Minerales (INREMI), Universidad Nacional de La Plata, La Plata, Argentina.

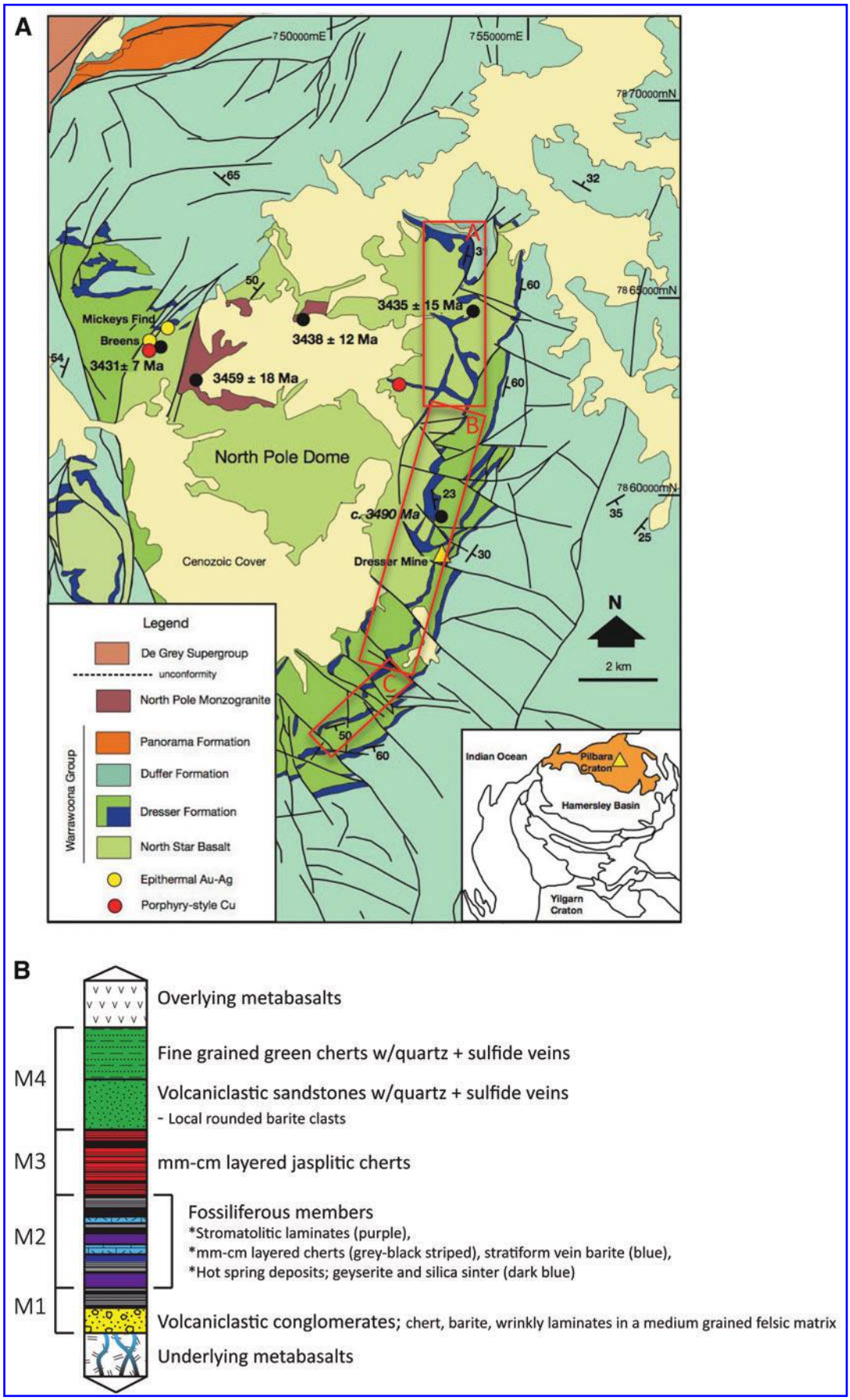

FIG. 1. **(A)** Geological map of the Dresser Formation in the North Pole Dome (modified from Harris *et al.*, 2009). The lower chert-barite sequence (DFc1) of the Dresser Formation is the blue chert horizon highlighted by inset red boxes A, B, and C. Inset boxes also correspond to detailed geological maps: Supplementary Fig. S1A–C. **(B)** Generalized stratigraphy of DFc1.

Subaerial (land-based) hot springs are surface manifestations of magmatic/volcanic systems. Subsurface circulation of magmatically heated meteoric water within the country rock, mixed with contributions from magmatic fluids, produces diverse hot springs and associated discharge aprons at the land surface (Pirajno, 2009). These hot springs exhibit a temperature range ~100°C to ambient, and may have variable pH (acidic to alkaline), ionic concentrations, metal content, and settings (*e.g.*, pools, terraces, geysers, fumaroles; White *et al.*, 1964; Walter, 1976; Bignall and Browne, 1994; Fouke *et al.*, 2000; Guidry and Chafetz, 2003a). Many hot springs are situated in fluvio-lacustrine environments and support diverse communities of microorganisms, the variability of which is controlled by temperature, pH, and chemistry (Renaut and Owen, 1988; Renaut *et al.*, 2002; Jones *et al.*, 2007; Guido and Campbell, 2011; Power *et al.*, 2018).

Although subaerial hot spring settings around the world can vary depending on climate, geology, and tectonics, they commonly produce a range of comparable abiotic and biologically mediated textures that are controlled by fluid temperature, fluid chemistry, water flow rate, microbial consortia, and host rock composition. In near-neutral pH alkali-chloride settings, these textures are characterized spatially in proximal vent to distal apron facies assemblages (Fig. 2; Cady and Farmer, 1996; Guido and Campbell, 2011; Campbell *et al.*, 2015a, 2015b).

Preservation of these deposits, including associated microbial communities, occurs rapidly as a result of silica precipitation driven by cooling and evaporation of the thermal spring fluid discharge, as well as by microbial mediation, resulting in a biomediated sinter apron terrace that blankets the surrounding landscape (White *et al.*, 1964). Local to regional hydrothermal alteration may also occur, leading to pervasive silicification, sulfidization, and/or steam-heated acid-sulfate alteration (*e.g.*, producing clay and other alteration minerals) of the underlying lithology (*e.g.*, volcaniclastic sediments, volcanic units, and/or travertines; Campbell *et al.*, 2004; Guido and Campbell, 2009, 2012; Sillitoe, 1993, 2015; Guido and Campbell, 2017).

The preservation of microbial communities in hot spring environments may be universal if the degree of subsequent alteration is not too severe. A high preservation potential in siliceous hot spring (sinter) deposits is supported by the following observations: (1) Silicification is extremely rapid (*i.e.*, occurs within living microbial mats); (2) silica is chemically inert; and (3) biosignatures, including biomolecules, are preserved deep into the geological record (Cady and Farmer, 1996; Trewin, 1996; Walter *et al.*, 1998; Djokic *et al.*, 2017; Teece *et al.*, 2020).

Previous work on the Dresser Formation revealed evidence for subaerial hot spring deposits and documented their local context within an epithermal environment (Van Kranendonk and Pirajno, 2004; Van Kranendonk *et al.*, 2008, 2018; Harris *et al.*, 2009; Djokic *et al.*, 2017). In this article, we provide more detailed lithostratigraphic observations for the hot spring occurrences and describe a hitherto unrecognized, diverse suite of ~3.5 Ga hot spring and associated deposits from the Dresser Formation. Stratigraphic, petrographic and geochemical data presented here illustrate the characteristics and distributions of the Dresser hot spring deposits, their spatial relationships to mineralized remnants of hot spring pools, and their similarities to Phanerozoic (fossil and modern) hot spring deposits from New Zealand, Yellowstone National Park, USA and Argentina.

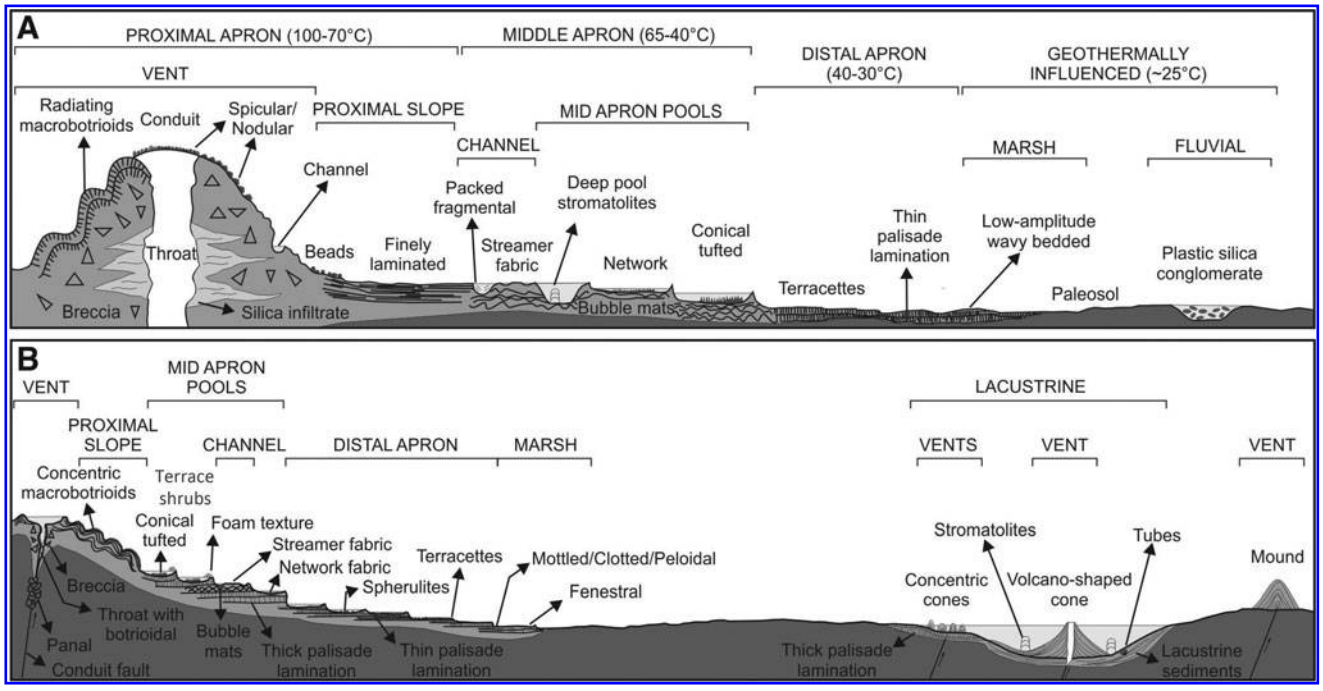

FIG. 2. Proximal to distal vent facies model from **(A)** siliceous and **(B)** travertine precipitating hot springs. Modified from Guido and Campbell (2011).

2. Geology of the Dresser Formation

The Dresser Formation is located in the North Pole Dome (NPD) of the Pilbara Craton, Western Australia (Fig. 1; Van Kranendonk *et al.*, 2007). The formation is formally defined as two main, relatively thin (~1–250 m) units of silicified sedimentary rocks (cherts) that bound a relatively thick (up to ~2 km) unit of doleritic and pillowed komatiitic basalt (Nijman *et al.*, 1999; Van Kranendonk, 2006; Van Kranendonk *et al.*, 2007, 2008, 2018).

The basal chert unit of the Dresser Formation (here referred to as DFc1) is the focus of this study, and it is recognized as containing stromatolites (*e.g.*, Walter *et al.*, 1980; Buick and Dunlop, 1990; Van Kranendonk, 2006, 2011). This unit is characterized by a complex stratigraphy, 1–288 m thick (Supplementary Figs. S1 and S2) that includes: bedded gray–white–black and jasplitic cherts; units of wrinkly laminated to domical and coniform stromatolites; a unit of interbedded carbonate-chert couplets that contain evaporitic aragonite crystal casts; sandstone and conglomerate; felsic ash; chert-barite breccia; and hot spring geyserite and sinter terracettes (Buick, 1985; Van Kranendonk *et al.*, 2008, 2018; Djokic, 2015; Djokic *et al.*, 2017; Djokic and Van Kranendonk, 2018; Otálora *et al.*, 2018). Thick, bedding-parallel, units of coarse crystalline barite were originally interpreted as baritized evaporative gypsum beds, but they have since been demonstrated to be intrusive sills of hydrothermal fluids (Nijman *et al.*, 1999; Van Kranendonk *et al.*, 2008).

DFc1 is underlain by pillowed and massive komatiitic basalts (North Star Basalt) that are cut by a complex network of weakly radiating hydrothermal veins up to 2 km long and 30 m thick. These veins are composed dominantly of black chert in their lower parts, but they transition to barite ± quartz ± pyrite toward the surface (Nijman *et al.*, 1999; Van Kranendonk *et al.*, 2008, 2018; Tadbiri, 2017). The black chert ± barite veins have been shown to be contemporaneous with DFc1 sedimentation (Nijman *et al.*, 1999; Van Kranendonk and Pirajno, 2004; Van Kranendonk, 2006; Van Kranendonk *et al.*, 2008; Poole, 2013; Djokic, 2015), and thus they have been identified as representing the mineralized circulation pathways of subsurface epithermal hydrothermal fluids (~100–350°C: Van Kranendonk and Pirajno, 2004; Van Kranendonk, 2006; Harris *et al.*, 2009). Overlying DFc1 are doleritic to pillowed basaltic volcanics that lack chert-barite veins and mark the end of pervasive hydrothermal conditions (Van Kranendonk *et al.*, 2008).

3. Previous Paleoenvironmental Interpretations of DFc1

The initial interpretation of DFc1 suggested that stromatolites grew in a quiet, shallow water marine environment (Groves *et al.*, 1981; Buick, 1985; Buick and Dunlop, 1990; Barley, 1993). This was based on the identification of four main lithostratigraphic assemblages characterized by two volcanogenic (arenite and lutite) and two chemical (carbonate and sulfate ± stromatolites) sedimentary units that included up to 22 sedimentary lithofacies with a suite of shallow water features (*e.g.*, Buick, 1985; Buick and Dunlop, 1990). Two shallowing-upward depositional cycles of evaporitic marine sedimentation were inferred, comparable to the modern semi-enclosed, hypersaline basin of Shark Bay, Western Australia, where communities of dominantly phototrophic microorganisms construct calcareous stromatolites (Buick and Dunlop, 1990; Jahnert and Collins, 2012).

These earlier studies interpreted the hydrothermal veins as having been emplaced either after the deposition of DFc1 (*e.g.*, Hickman, 1984; Buick, 1985) or during younger weathering (Hocking and Cockbain, 1990). Stratiform barite within DFc1 was interpreted to have formed through baritization of originally evaporative gypsum (Buick *et al.*, 1981; Buick, 1985; Buick and Dunlop, 1990; Barley, 1993).

Further geological work that focused on the relationship between facies distributions and stratigraphic contacts with the chert-barite veins led to a tectonically active, volcanic caldera interpretation of the environment of deposition (Nijman *et al.*, 1999; Van Kranendonk, 2000, 2006). Critical observations include: (1) Almost all chert-barite veins cross-cutting the underlying basalts disperse into, and terminate at, barite mound complexes within DFc1, or are eroded and unconformably overlain by DFc1 sediments; (2) syn-depositional growth faults control both DFc1 thickness variations and the geometry of veins; (3) sedimentary facies change abruptly across active growth faults; (4) uplapping of bedded chert and diamictite occurs onto vein-derived barite mounds; (5) eroded hydrothermal material (including barite+chert) occurs in sandstone and diamictite at multiple stratigraphic levels within DFc1; (6) hydrothermal veins pass laterally into bedded sediments; and (7) alteration of the footwall was of epithermal type and linked to the distribution of the hydrothermal veins (Nijman *et al.*, 1999; Van Kranendonk and Pirajno, 2004; Van Kranendonk, 2006; Van Kranendonk *et al.*, 2008, 2018; Poole, 2013; Djokic, 2015).

These findings collectively demonstrated the syn-depositional nature of chert-barite hydrothermal veins relative to DFc1, where barite, chert, and associated sulfides were viewed as primary hydrothermal precipitates derived from Si, Ba, and sulfide-rich fluids that vented onto a shallow (<50 m depth) seafloor, possibly as white smokers in a caldera-type setting (Nijman *et al.*, 1999; Van Kranendonk and Pirajno, 2004).

Van Kranendonk and Pirajno (2004) showed that basalts as deep as 1.5 km beneath DFc1 had experienced zoned, advanced argillic (50–200°C; kaolinite–pyrophyllite–alunite–barite), argillic (kaolinite), phyllic (quartz–white mica–rutile±chlorite±epidote), and propylitic (250–350°C; chlorite–carbonate–epidote) alteration, characteristic of epithermal hydrothermal systems (*e.g.*, Pirajno, 2009). Late-stage epithermal quartz textures were also observed within the cores of chert-barite veins, indicating low temperatures (~150–300°C) and shallow depths. This observation was later augmented by fluid inclusion data, indicating that near-neutral pH, alkali-chloride fluids typical of epithermal systems may have fed land-based hot springs inhabited by life (Harris *et al.*, 2009).

Based on regional stratigraphy, geochemistry, and geochronology, the Dresser Formation was deduced as forming within an oceanic plateau equivalent to the Phanerozoic Kerguelen Plateau, arising from hot spot magmatism (Van Kranendonk and Pirajno, 2004). Such a model is consistent with other regional geological and geochemical data from across the Pilbara Craton (Smithies *et al.*, 2007; Van Kranendonk *et al.*, 2007).

Van Kranendonk (2006) and Van Kranendonk *et al.* (2008) developed a four-stage depositional model for DFc1 that supported a volcanic caldera setting. In this model, Stage 1 resulted from magma-driven uplift, which caused the onset of shallow water deposition of stromatolites, cross-bedded sandstone, and bedded carbonates. Stages 2 and 3 included multiple episodes of hydrothermal fluid circulation accompanied by minor felsic volcanic eruptions during caldera development, under shallow water to subaerial conditions. Finally, stage 4 represented caldera collapse, marked by deposition of a fining upward succession of conglomerate and siltstone composed of mafic volcaniclastics, as well as by cessation of hydrothermal veining.

As for the stromatolites and other microbially induced sedimentary structures preserved in DFc1, a variety of metabolic pathways have been inferred based on morphological diversity, environmental associations, and stable isotopes. Phototrophy has been suggested from the presence of domical and conical stromatolites (Walter *et al.*, 1980; Buick and Dunlop, 1990; Van Kranendonk, 2011), whereas the association of broad domical stromatolites with inferred subaqueous hydrothermal vents was used to suggest active chemotrophy during the formation of some stromatolites (Van Kranendonk, 2006, 2011). Carbon isotopic data from hydrothermal black chert veins and sulfur isotope data from microscopic pyrite (sulfide) inclusions along barite (sulfate) growth zones were used to suggest anaerobic methanotrophs (Ueno *et al.*, 2006) and sulfate-reducing microbes (Shen *et al.*, 2009), or microbes that cycled elemental sulfur (Philippot *et al.*, 2007).

Biogenicity of the stromatolites is strongly supported by the recent discovery of organic remnants trapped in nanoporous pyrite (Baumgartner *et al.*, 2019).

Recent research has provided a direct connection between shallow subaqueous to subaerial hydrothermal activity and life. Surficial deposits of hot spring geyserite and sinter terracettes were discovered, associated with a variety of textural biosignatures in a few, thin, isolated exposures of DFc1 (Djokic *et al.*, 2017).

4. Methods

4.1. Field mapping

Local sites detailed in this study (16N, 1S, 24S; Supplementary Fig. S1) were selected based on data collected from more than 100 measured transects across DFc1 from 2013 to 2016, which revealed the presence of hot spring deposits. The measured sections and detailed mapping were undertaken from across the entire ~14 km of strike-length of DFc1, as exposed on the eastern flank of the NPD (Fig. 1, Supplementary Figs. S1 and S2). The Global Positioning System coordinates were collected for all measured sections.

4.2. Optical microscopy

Optical microscopy was undertaken on a Nikon Eclipse Ci POL microscope with a Nikon DS-Vi1 camera by using standard polished thin sections (30 μm thick) at the University of New South Wales.

4.3. Scanning electron microscopy-energy dispersive spectroscopy

Rock samples with freshly broken surfaces were either prepared with an evaporative carbon coating or wrapped in copper tape at the Electron Microscopy Unit (EMU) of the Mark Wainwright Analytical Centre at the University of New South Wales, Australia. Samples were examined by using Hitachi S-3400N scanning electron microscopy (SEM), operating from 10 to 50 kV, and fitted with a Bruker SDD-EDS XFlash 6-30 detector.

4.4. Electron microprobe-wavelength dispersive spectroscopy

A polished thin section of stromatolitic intraclast conglomerate (see Section 5.1.2.2) from site 16N (Supplementary Figs. S1 and S2) was investigated by transmitted light microscopy before electron microprobe-wavelength dispersive spectroscopy (EMP-WDS) analysis to locate a single clast with a dark coating/rind, suspected of containing Ti. Analysis of the desired location in the single intraclast was conducted on a JEOL JXA-8500F EPMA by using an accelerating voltage of 15 kV, 20 nA beam current, and beam diameter of 1 μm. Note that because the energy resolution of energy dispersive spectroscopy (EDS) does not allow Ba and Ti X-rays to be fully resolved, qualitative WDS mapping was undertaken to distinguish the distributions of these two elements over the area of interest. Analytical parameters used were 15 kV accelerating voltage, 50 nA beam current, and a dwell time of 30 ms per pixel. The system was calibrated by using natural and synthetic mineral standards. Analysis was performed by using an oxide matrix correction (oxygen calculated by stoichiometry, H_2O calculated by difference; results in oxide mass percent). Calibration was tested by using secondary silicate mineral standards, with accuracy for NaO, MgO, Al_2O_3, SiO_2, SO_3, CaO & TiO_2 $\leq \pm 2\%$ relative, and K_2O, MnO, FeO, BaO & Cl $\leq \pm 5\%$ relative.

4.5. Trace element geochemistry

Samples were either lightly crushed or in the case of the sinter/geyserite samples were milled to a powder in an agate mill. Cleaning of the agate mill between samples involved powdering a small amount of the subsequent sample, which was then blown out with an air gun before the mill was cleaned with ethanol and dried. Generally, between 140 and 470 mg of samples (25 mg for sinter/geyserite samples) were digested with an HF-HNO_3 mixture in capped Teflon vials on a hotplate overnight at 135°C, then evaporated to dryness, refluxed twice with concentrated HNO_3, and finally dissolved overnight in dilute HNO_3. The solutions were transferred to transparent polycarbonate tubes and diluted with 18.2 megohm, deionized water.

An aliquot of each solution was further diluted with a dilute HNO_3 solution containing an internal standard mixture to give total dilution factors ranging from 100 to 3500. This procedure was based on a visual estimate of the mass of solids that remained after digestion. These estimates were informed by previous experience in digesting similar rock types (*e.g.*, Van Kranendonk *et al.*, 2003).

Analytical and drift correction procedures are comprehensively described in Eggins *et al.* (1997). The method uses a natural rock standard for calibration, internal drift correction using multi-internal standards (Li^6, Sr^{84}, Rh, Re, and U^{235}), external drift monitors, and aggressive washout procedures. Differences in the methods of this study from the Eggins *et al.* (1997) technique were applied as follows:

(1) Sm^{147}, Tm, In, and Bi were not used as internal standards as these are analyses; and (2) two digestions of the USGS standard W-2 were used for instrument calibration. The preferred concentrations utilized for W-2 were mostly derived by analyzing them against synthetic standards and a literature survey of isotope dilution analyses (Kamber *et al.*, 2003, 2005; Babechuck *et al.*, 2010). Because only a single calibration standard was used, data were more easily normalized to other sets of preferred values for standards.

Samples were analyzed at the School of Earth Sciences, University of Melbourne, on an Agilent 7700×. The instrument was tuned to give barium oxide levels of 0.067%. Four replicates of 100 scans per replicate were measured for each isotope. Long sample wash-out times of 6 min with solutions of 0.5% Triton X-100, 0.025% HF in 5% HNO_3, and 2% HNO_3 and long sample uptake times of 120 s were used.

Samples with Ba/Eu ratios greater than 4000 were reanalyzed for rare earth element and yttrium (REE and Y) under conditions with a Ba oxide level of 0.019% by using the dilution gas mode and He mode with a 2 mL/min He flow to the collision cell.

5. Lithostratigraphy of DFc1

Mapping was conducted along the ~14 km exposure of the Dresser Formation lower chert-barite sequence (DFc1) on the eastern flank of the NPD. These strata are tilted eastward with an average dip of about 45° (Fig. 1, Supplementary Fig. S1). Good exposure allows detailed mapping of facies distributions, local unconformities, and growth fault control on sedimentation at both regional (km) and local (m) scales. The stratigraphic thickness of DFc1 is highly variable, ranging from ~1 to 288 m thickness (Fig. 1, Supplementary Figs. S1 and S2; Nijman *et al.*, 1999; Van Kranendonk *et al.*, 2008). Clear contacts between bounding basaltic units above and below DFc1 can be seen in many places.

Based on 100 measured sections, the ~14 km N-S trending exposure of DFc1 is divided here into four members, M1–M4. With the exception that in some places M3 is interbedded with M2, these members are observed in sequence from base to top (Supplementary Figs. S1 and S2; Djokic, 2015). The division of these members is based on characteristic lithological assemblages comprising sedimentary±hydrothermal units that can be traced across the study area (Supplementary Fig. S2).

M1 is characterized dominantly by a range of bedded cherts (including jaspilitic chert), clastic sedimentary rocks, which include felsic volcanic ash deposits, and local stromatolites. M2 is characterized by bedded cherts, a distinctive unit of bedded carbonate-chert couplets, abundant stromatolites, and hot spring deposits. M3 is defined by bedded chert with a dominant (>80%) component of jasplitic (hematite-rich) chert that is in some places cut by chert-barite veins. M4 marks the final stage of sediment deposition for DFc1, characterized by green-gray volcaniclastic units. Hydrothermal chert±barite veins are synchronous with M1 and M2, are lacking in M3, and are absent from M4.

5.1. Members M1–M4

5.1.1. Member 1. M1 outcrops in only a few locations (12N, 13N, 14N, 17N, 21S; Supplementary Figs. S1 and S2), with thicknesses that reach a maximum of ~10 m. M1 is composed of a variety of bedded chert units, rippled sandstone, stromatolites, and chert-barite breccia (Supplementary Fig. S3). Toward the base of M1 is a distinct chert-barite breccia that consists of a variety of cobble- to boulder-sized (cm-decimeter) clasts supported within a sandy, gravelly, and pebbly matrix (30–50% of the unit) (Supplementary Fig. S3C–G). The boulders range from angular to some that are rounded and are derived from the surrounding, local stratigraphy; so, they include: coarsely crystalline barite (1–5 cm length crystals in 1–2 cm-thick isopachous beds); gray, white, and black-colored, cm-bedded chert; jaspilitic (hematite-bearing) chert that is defined by opaque red to translucent red layering; massive gray-colored chert; and stromatolites. The matrix includes stromatolitic intraclasts, pumice fragments, and hydrothermal alteration minerals, *i.e.*, sericite (Supplementary Fig. S3D–G).

Bedded chert units in M1 (and overlying members) typically display mm- to cm-thick, gray, white, and black-colored, layered chert that commonly includes thin (1–2 mm) horizons of mm-sized, rhombic, diagenetic carbonate casts (weathered) at the tops of cm-thick chert beds (Supplementary Fig. S3A).

Stratigraphically, the rippled sandstone in M1 is typically confined to decimeter-thick layers and is commonly associated with stromatolites. The chert-barite breccia is observed at multiple stratigraphic levels and, in some places, disconformably overlies the North Star Basalt (*e.g.*, at locality 14N; Supplementary Figs. S1 and S2). Bedded gray–white–black chert units are meters thick and extensive throughout the lower two assemblages (M1 and M2).

5.1.2. Member 2. M2 is widespread throughout DFc1, ranging between ~0.5 and 10 m in thickness (Supplementary Fig. S2). It displays a highly diverse suite of dominantly subaerial to shallow-water sedimentary rocks and a morphologically diverse array of stromatolitic forms (detailed in Section 5.3). Lithofacies include: a well-bedded unit consisting of repeated carbonate-chert couplets with diagenetic aragonite crystal casts (Van Kranendonk *et al.*, 2003; Otálora *et al.*, 2018); bedded gray–white–black chert; minor jasplitic chert; tabular edgewise conglomerate (EC); rounded pebble to cobble conglomerate; massive or rippled sandstone; and localized hot spring deposits, including geyserite and sinter terracettes (see also Djokic *et al.*, 2017). Facies characteristically show abrupt lateral facies changes on the order of tens of cm to up to 100 m over the extent of the study area (Supplementary Fig. S2).

Near the base of M2 is a widespread, distinctive evaporitic unit composed of interbedded carbonate-chert couplets referred to as ''zebra rock'' (Van Kranendonk *et al.*, 2003, 2008). This evaporitic unit is up to ~40 cm thick, and it is defined by alternating layers of Mn-rich ankerite (~2–3 cm thick) and pale green chert (~1–2 cm thick), which contain radiating, acicular, diagenetic crystal splays or ''rosettes'' (<5 cm in diameter) (Van Kranendonk *et al.*, 2003, 2008, 2018). Crystal splays have pseudohexagonal crystal outlines, which were previously inferred as replacive after gypsum (Buick and Dunlop, 1990), but have more recently been identified as replacive after aragonite (Otálora *et al.*, 2018; Supplementary Fig. S4). Primary ankerite is only preserved in one outcrop (see Van Kranendonk *et al.*, 2003;

site 4NW; Supplementary Figs. S1 and S2), whereas at all other localities the ankerite has been entirely silicified and ''zebra rock'' is primarily identified by the presence of the diagenetic crystal splays.

Contacts between couplets show gradational transitions from carbonate horizons into overlying chert beds, but with sharp contacts from the top of each chert layer to the overlying carbonate. The aragonite crystal casts are present in both compositional components of the couplets. Although laterally discontinuous, the ''zebra rock'' is distributed across DFc1 and is consistently overlain by a sequence comprising stromatolitic facies, inferred hot spring deposits, and other shallow water units such as edgewise and pebble conglomerates, described below (Supplementary Fig. S2).

5.1.2.1. Hot spring deposits. Hot spring geyserite has been identified at three widely separated localities within M2 (16N, 1S, 24S: Supplementary Figs. S1 and S2; see also Djokic *et al.*, 2017). This characteristic sinter deposit (Campbell *et al.*, 2015a) is observed in the Dresser Formation either as <5 cm-thick discontinuous beds within cherty, layered rocks or as angular intraclasts ($\sim$20–500 μm wide and up to $\sim$5 mm long) within conglomerate that outcrops laterally across distances of only a few meters.

Distinctive features of the geyserite include microscopically thin (50 μm), alternating black–white siliceous laminae that are enriched in anatase (low-temperature polymorph of TiO_2) and kaolinite-illite, respectively (Fig. 3; Djokic *et al.*, 2017). Macrotextures include: well-laminated botryoidal to nodular geyseritic textures that are separated by nonlaminated, homogeneous troughs containing microscopic grains of quartz and other indiscriminate silicified matrix material (Fig. 3B); columnar and/or stratiform textures (Fig. 3B–D), including slump structures (Fig. 3D); and laminae overgrowths (see Djokic *et al.*, 2017).

Sinter terracettes with microbial palisade fabric were identified at locality 1S (Supplementary Figs. S1 and S2; see also Djokic *et al.*, 2017) in a $\sim$10 cm-thick unit, which also preserves geyserite. The terracettes are either completely silicified or composed of fine hematitic laminae interbedded with microquartz (Fig. 4A, B). This sinter unit is characterized by centimeter-scale, wavy to convex bedding and by individual laminae that display fine elongated quartz crystals (<10 μm thick, up to 600 μm long) that are oriented perpendicular to bedding and wrap around both convex and stratiform parts of the layering (Fig. 4A–E). In one example, the vertical quartz fabric is present in three successive layers that show an increasing degree of recrystallization from the top down, with epithermal microquartz textures overprinting the lower bedding (Fig. 4E). The distinct vertical quartz crystals have been interpreted as representing microbial palisade fabric that forms when filamentous bacteria growing in densely packed, vertical micropillars are entombed on the outflow aprons of hot spring pools (Weed, 1889; see also Djokic *et al.*, 2017).

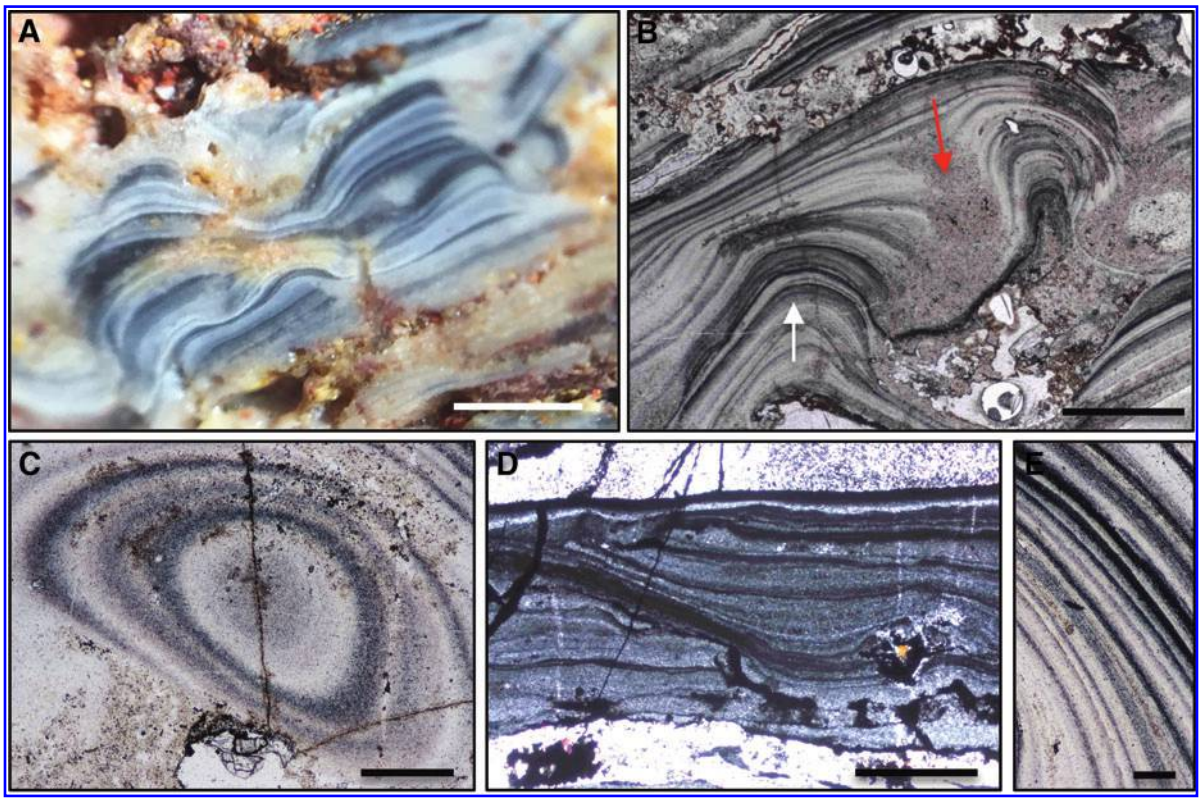

FIG. 3. Dresser Formation geyserite. Scale bar measurements and polarized light indicated. **(A)** Botryoidal features in hand sample (2 mm). **(B)** Botryoids (white arrow) separated by equigranular troughs (red arrow) (1 mm, ppl). **(C)** Plan view of botryoid (1 mm, ppl). **(D)** Slump structures (1 mm, xpl). **(E)** Distinct fine scale black and white laminations characteristic of geyserite (100 μm, xpl). ppl, plane polarized light; xpl, crossed polarized light.

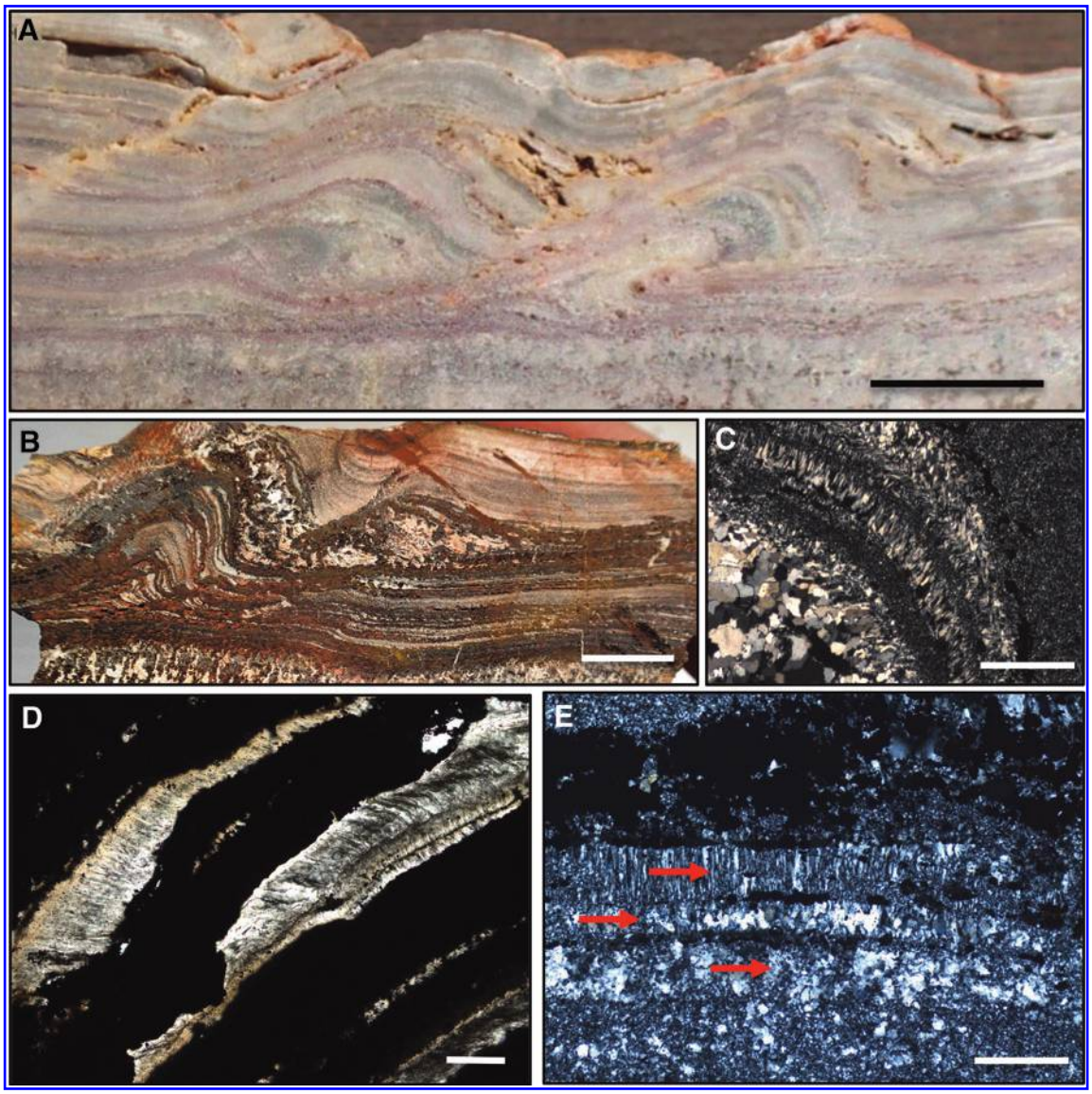

FIG. 4. Dresser terracettes with palisade fabric. Scale bar measurements and polarized light indicated. **(A)** Silicified terracette (shrub-like structures at base) in cross-section showing convex bedding migrating to the right (1 cm). **(B)** Non-silicified, hematitic layering preserved in terracettes (1 cm) and interbedded with shrub-like structures. **(C,D)** Palisade fabric (**C**—1 mm, xpl; **D**—500 μm, ppl). **(E)** Three layers of palisade fabric with increasing recrystallization down section (1 mm, xpl).

5.1.2.2. Clastic sedimentary rocks. Stromatolitic intraclast conglomerate and a variety of ECs are common and widespread throughout M2. Such conglomerates are observed interbedded with the hot spring deposits. These units are characterized by long, thin, angular, or contorted and commonly finely laminated clasts. Internal laminae are generally planar. These conglomerate layers are on average 10's of centimeters thick, to a maximum of ~50 cm thick, lack internal beds, and extend one to several meters laterally along strike (Supplementary Fig. S2).

Stromatolitic intraclast conglomerate displays small, contorted to curved, and dumbbell-shaped clasts, 1–6 mm long and 1–3 mm thick, that are well rounded to angular (Fig. 5A, B). There are at least two types of clasts among different outcrops. Some clasts exhibit very thin (<10 μm), alternating gray–white laminations with faint grading between light and darker laminae (Fig. 5B). Other clasts are homogeneously light gray in color, fine-grained, and display faint or no internal layering. These latter clasts commonly have dark, opaque (possibly due to organics; see Buick, 1985) rinds that are similar to the fine anatase laminae of the geyserite. The rinds coat either only one side of the clasts or the entire clast (Fig. 5C, D). Some of these clasts display internal cracks (~10 μm wide) that are commonly filled with white mica (sericite), and they terminate into dark, irregular bedding-parallel seams (Fig. 5C). Clasts that lack internal bedding have granular cores composed of Fe-oxides/hydroxides, white mica, and microquartz (Fig. 5D). These clasts commonly have rinds with thin (<10 μm), opaque microquartz inner mantles and thicker (up to 50 μm) outer mantles of microquartz±Ti (Fig. 5D, E). Many clasts have an undulating or wavy edge on one side and a

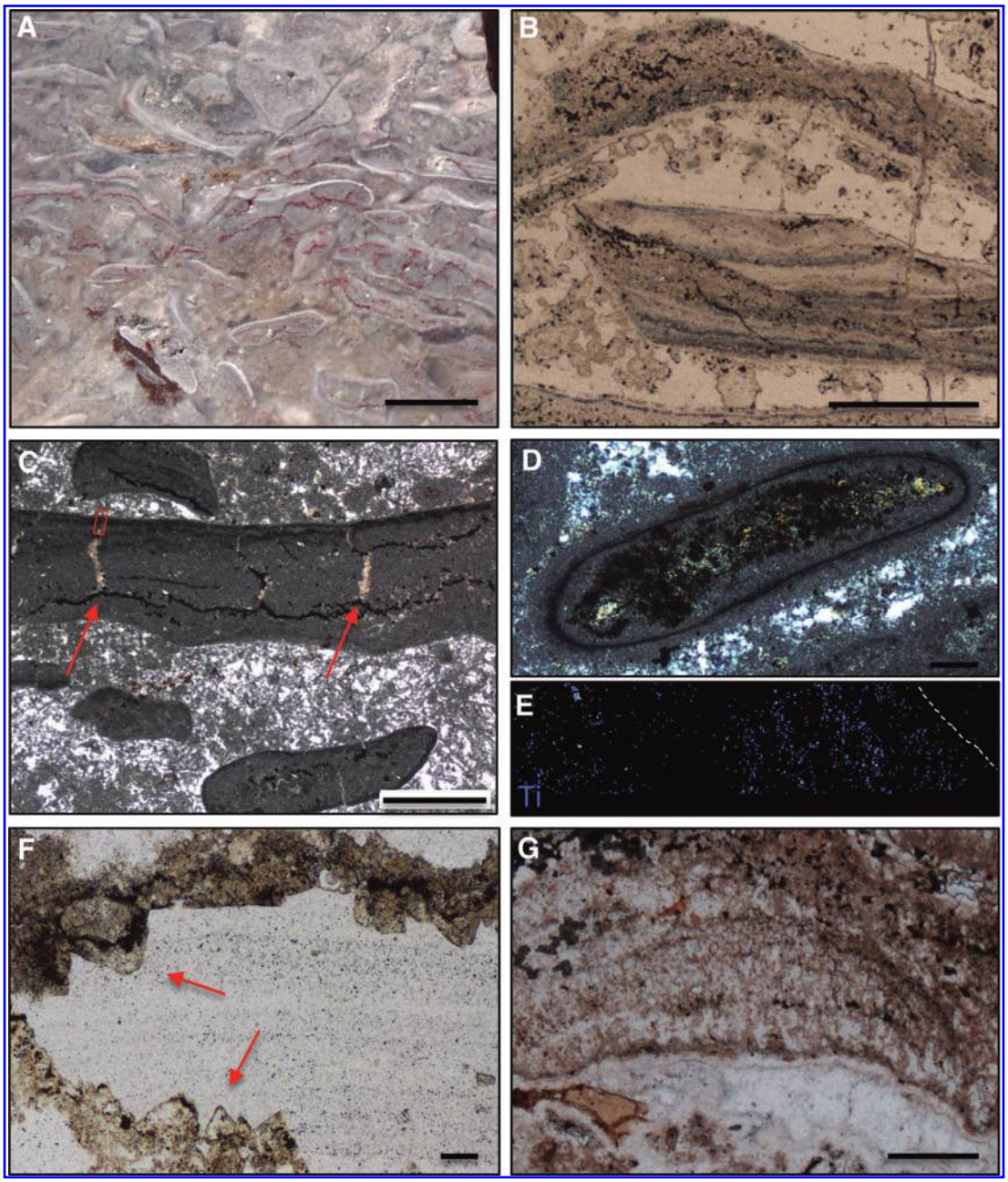

FIG. 5. Examples of Dresser stromatolitic intraclast conglomerate. Scale bar measurements and polarized light indicated. **(A)** Hand sample showing curved, contorted, and dumbbell-shaped clasts (5 mm). **(B)** Intraclasts containing faint graded; beds (1 mm, ppl). **(C)** Intraclasts without bedding and that contain internal mica-filled cracks terminating into dark seams (red arrows) (1 mm, xpl). Red inset box—**(E)**. **(D)** Intraclasts with core of mica and clotted Fe-oxide, and which are coated with dark and light siliceous rinds (100 μm, xpl). **(E)** Electron microprobe-wavelength dispersive spectroscopy map showing Ti concentration indicating anatase at the edge of an intraclast. See inset box in **(C)**. Dashed line marks the edge of the clast. **(F)** Carbonate rhombs growing into the edge of clasts; red arrows (100 μm, ppl). **(G)** Intraclasts of filamentous nature (10 μm, ppl).

straight edge on the other side (Fig. 5C). In some examples, diagenetic carbonate rhombs partially replaced and/or grew from the external matrix into the outer edges of semi-lithified intraclasts (Fig. 5F). Rare clasts displaying sinuous filamentous structures composed of microquartz surrounded by light brown Fe-oxide/hydroxide haloes are also observed (Fig. 5G; 17NW: Supplementary Figs. S1 and S2).

At locality 16N, a stromatolitic intraclast conglomerate is interbedded with tabular ECs and rounded pebble conglomerate (detailed below). These three units are also locally interbedded with layered chert, sandstone, and/or stromatolites.

The ECs include two main types, each with slight variations. The first type (EC-i) is composed of highly elongated, siliceous clasts (1–10 mm × 0.5–30 cm—exhibiting high

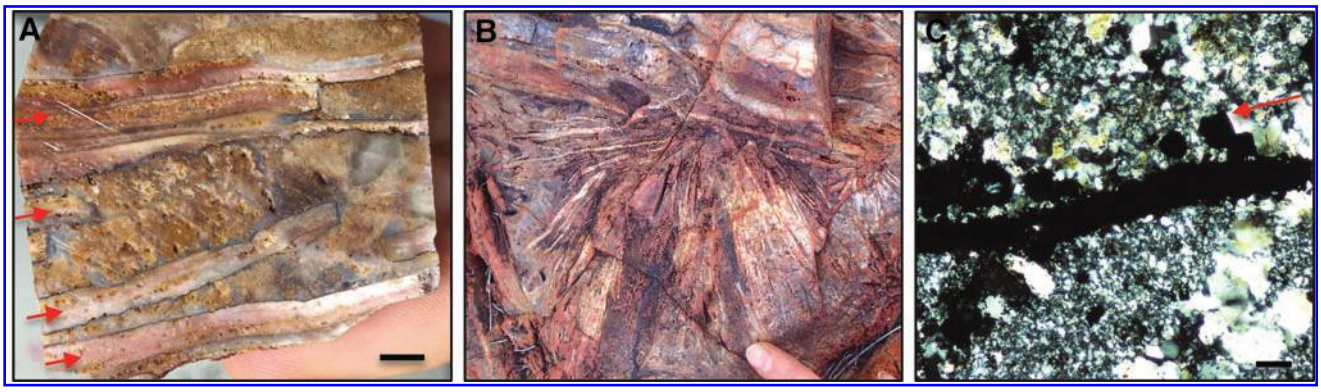

FIG. 6. EC-i. Scale bar measurements and polarized light indicated. **(A)** Gently curved, elongated platy clasts; red arrows (5 mm). **(B)** Clasts stacked in fanning arrays. **(C)** Fe-oxide/hydroxide crust that coats edgewise clasts with euhedral pyrite at border (red arrow) on edge of clasts (100 μm, xpl). EC-i, edgewise conglomerate-i.

aspect ratios of up to 40:1) that are platy or tabular, to gently curved and locally contorted (Fig. 6). Clasts vary in color (*i.e.*, white, gray, black, red, and brown) and exhibit thin (mm), dense to porous internal laminae. The highly tabular clasts are oriented vertically on their narrow edge (*i.e.*, edgewise), and they are typically stacked as fanning bundles or as irregular plates that radiate in all directions (Fig. 6B). Clasts are derived from the immediately underlying lithology, as seen by the occurrence of chert beds preserved in lift-off position and stacked over other clasts (see Sections 6.1, 6.3).

These conglomerates are preserved as channelized lenses (up to 3 m wide × 3 m long) with sharp margins. Petrographic analysis of weathered surface outcrops shows that the chert clasts are coated by ferruginous oxides/hydroxides (~100 μm thick), contain thin laminae of Fe oxyhydroxides, and lie within a matrix of micro- to macroquartz±barite± rhombic carbonate±euhedral pyrite±Fe-oxides/hydroxides (Fig. 6C).

The second type of EC (EC-ii) is characterized by very thin (<0.5 mm), up to 5 mm-long, black-weathered ferruginous clasts (Fig. 7A) that locally (locality 24S: Supplementary

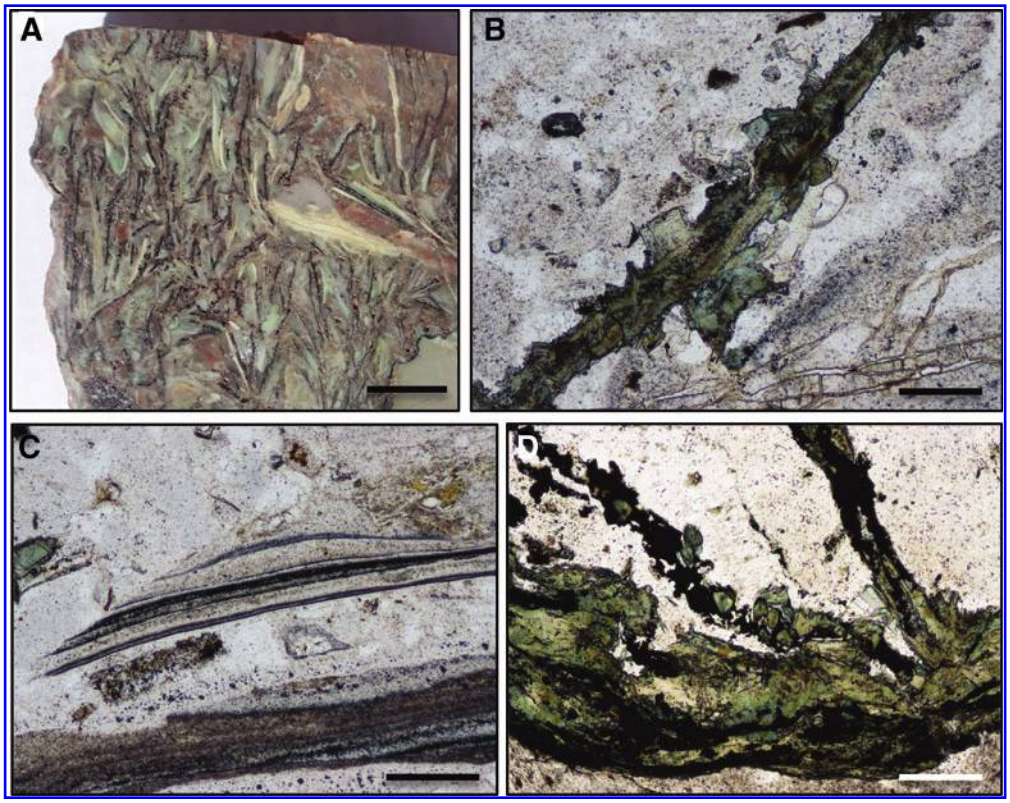

FIG. 7. EC-ii. Scale bar measurements and polarized light indicated. **(A)** Hand sample of EC-ii (1 cm) with distinct long black ferruginous clasts containing **(B)** tourmaline (200 μm, xpl), which are intermixed with **(C)** angular geyserite clasts (1 mm, ppl). **(D)** Tourmaline clasts that are still attached to, but lifting-off from, the underlying unit (200 μm, xpl). EC-ii, edgewise conglomerate-ii.

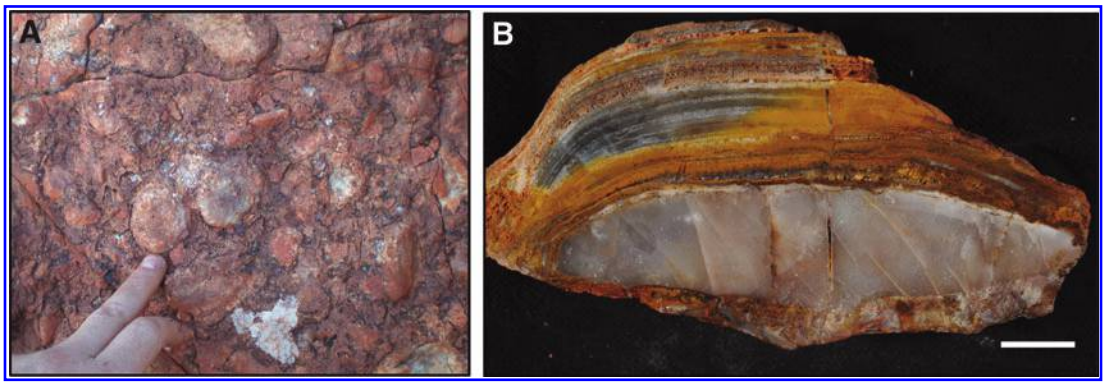

FIG. 8. Rounded pebble-to-cobble conglomerate in the Dresser Formation. Scale bar measurement indicated. **(A)** Outcrop image. **(B)** Cross-section showing white translucent chert pebble overlain by tourmaline-bearing wrinkly laminates (1 cm). Compare with Guido and Campbell (2019), their Figs. 2D and 3.

Fig. S1) contain packed, micron-sized, dark green tourmaline crystals (Fig. 7B). In addition to these tourmaline-bearing clasts are angular geyseritic clasts (cf. ''sintraclasts'' of Jones and Renaut, 2003), shards of felsic volcanic glass, sand-sized volcanic grains (Fig. 7) and, rarely, clasts that resemble the bedded clasts from the stromatolitic intraclast conglomerate (*i.e.*, Fig. 5). The elongated clasts are typically imbricated edgewise but may be stacked at various other angles. The tourmaline-rich clasts derive from an underlying unit of finely laminated, tourmaline-bearing ferruginous crusts (<3 cm thick), demonstrated by clasts that are still attached, but lifting off from the underlying unit (Fig. 7D; Djokic, 2015).

The rounded pebble to cobble conglomerate is widespread within M2, but is laterally discontinuous, occurring in outcrops that extend for only a few meters along strike (Supplementary Fig. S2). Units are 10–20 cm thick and contain well-rounded, pebble- to cobble-sized clasts, up to 6 cm in diameter, composed almost exclusively of translucent white chert (Fig. 8). This unit is typically overlain by the thin (1 mm) ferruginous layers described earlier, and it is interbedded with EC.

A breccia unit of angular to sub-angular, blocky clasts (~2–4 mm diameter) was observed at locality 16N (Supplementary Figs. S1 and S2). Clasts consist of a core of fine-grained, subhedral to euhedral Fe-oxides±barite, rimmed by several coatings of Fe-oxide laminae alternating with fine-grained silica (Fig. 9). This unit is ~5 cm thick, overlies the pebble conglomerate, and is located <3 m laterally away, and <1 m up-section, from geyserite (Djokic *et al.*, 2017).

5.1.3. Member 3. M3 is up to 6 m thick and composed of black–white–gray chert and red jasplitic (*i.e.*, hematite-bearing) bedded chert (Supplementary Fig. S5). Although this unit is widespread, it is laterally discontinuous, typically outcropping as lenses no more than a few hundred meters along strike. At two locations, M3 appears to be fault controlled, displaying up to ~6 m-thick sections ~100–250 m across, bound by major listric growth faults (Supplementary Fig. S2). M3 generally not only lies on bedded cherts and sandstone of M2 but also lies above thinner sections of clastic sedimentary deposits from M1–M2. Overlying M3 is either lithologies of M4 or pillow basalt of the Dresser Formation.

5.1.4. Member 4. M4 is up to ~150 m thick and is composed of green, silicified volcaniclastic conglomerate, sandstone, and siltstone, fining upward from base to top through a series of repeated depositional cycles (Supplementary Fig. S6). Some clasts contain pyroxene spinifex texture and are, thus, probably derived from uplift and erosion of underlying komatiitic basalts (Buick, 1985; Van Kranendonk, 2006). Sandstones are composed mainly of green, sub-angular to sub-rounded sand grains ~0.5–1 mm in diameter, but they may also contain sand- to pebble-sized clasts of barite±volcanic ash±intraclasts (Supplementary

FIG. 9. Distinct breccia unit found only at site 16N (Supplementary Fig. S2) in DFc1. Scale bar measurements and polarized light indicated. **(A)** Outcrop image (5 mm). **(B)** Thin section image showing angular clasts with Fe-oxide-rich coatings (5 mm). Inset box; **(C)** close-up micrograph of single clast showing internal Fe-oxide-hydroxide core with silicified mantle and Fe-oxide rind (1 mm).

Fig. S6A). Bedding typically does not show evidence of grading or cross-stratification, and the depositional thickness of the unit is controlled by active growth faults (Poole, 2013; Van Kranendonk *et al.*, 2018). This unit is cut by thin, zoned, quartz-sulfide veins, rather than by the chert-barite veins in the underlying units (Poole, 2013).

5.2. Hydrothermal veins

Hydrothermal chert-barite veins are common in the lower two members (M1–M2) in DFc1, but they also extend up into M3. These veins penetrate deep (up to ~2 km) into the volcanic strata underlying DFc1 as a distinct boxwork pattern of veins, with individual veins ~1–30 m thick (see Van Kranendonk, 2006: Fig. 6b). These lower parts of the veins are composed dominantly of fine-grained, black, siliceous organic-rich chert. However, black siliceous chert veins may also appear as m-thick sills within the DFc1 sedimentary units.

Locally, the veins are uncomfortably overlain by DFc1 sedimentary rocks (*e.g.*, 11N: Supplementary Fig. S2).

The upper avg. ~75 m of the chert-barite veins commonly contain coarse grained gray barite ± chert ± epithermal quartz. Epithermal quartz textures consist of colloform to inward-radiating quartz and stalactite-like textures, up to 6 cm long, which are observed as either cavity-fill structures or sills (see Harris *et al.*, 2009).

These chert-barite veins intrude up into, and along bedding within the sedimentary rocks of DFc1. Coarsely crystalline barite outcrops as either subsets (cm thick) of layered parallel horizons (cm-m thick) within bedded sedimentary rocks or mound-like masses (up to 5 m^2). Barite layers that are bedding parallel link spatially to feeder hydrothermal chert-barite veins that cross-cut sedimentary bedding. Large barite mounds contain internal, curled, layers of coarsely crystalline barite, and the mounds are not only intrusive into but also onlapped by sedimentary units (see Section 6.2; see also Nijman *et al.*, 1999).

5.3. Stromatolite distribution

Stromatolites are widespread across the map area but restricted to shallow-water units of M2, and locally in M1. Their distribution is markedly patchy, outcropping as thin (<10 cm) layers over short distances of a few meters to tens of meters (Supplementary Fig. S2). In only one area are stromatolites traceable laterally for a few hundred meters (*e.g.*, 1N–8N; Supplementary Fig. S2). Stromatolite morphologies are highly variable, including wrinkly laminated to small (cm) or large (decimeter) domes and cones, as well as elongated, pustular, and shrub-like forms. Some morphological types are restricted to only a few outcrops (*e.g.*, elongated forms at 24S and 2S.A; pustular mats at 24S; domes with incipient branches at 6S; shrubs at 1S: Supplementary Fig. S2; see also Section 6).

Most surface outcrops of stromatolites are composed of finely laminated, Fe oxyhydroxides, chert, and barite. In fresh drill core samples, these stromatolites were found to consist of pyrite±sphalerite±chert±carbonate (Van Kranendonk *et al.*, 2008; Baumgartner *et al.*, 2019). Some coniform to irregularly domical stromatolites of M2 are found in thinly bedded chert, which may derive from silicification of primary carbonate.

Thick, wrinkly laminated stromatolites commonly lie on rippled sandstones that immediately overlie the ''zebra rock''. Stromatolites are also interbedded with, or capped by thin units of EC. More distinct and variably distributed stromatolite morphologies are found together with a variety of pebble conglomerate and ECs, and with geyserite deposits at different stratigraphic levels within M2 (*e.g.*, 24S). Stromatolites may or may not contain layer-parallel units of intrusive, hydrothermal barite and/or early diagenetic barite crystals.

6. Stratigraphy of Hot Spring Deposits

Hot spring geyserite and siliceous sinter terracettes are known from three well-exposed localities in M2 (*i.e.*, 16N, 1S, 23S: Supplementary Figs. S1 and S2; see also Djokic *et al.*, 2017). Detailed lithostratigraphic observations of these three key localities are presented here to aid interpretation of the complete setting of the inferred Dresser hot spring deposits.

6.1. Geyserite discovery locality (16N)

The ''geyserite discovery locality'' (local area of 16N: Supplementary Figs. S1 and S2) is located ~3 km north of the Dresser Mine. Covering an area of ~150 m^2, the best exposures are found within the south-east area of a moderately dipping (~40°) ridge of bedded cherts that are truncated to the north and south by faults. This ridge exposes between ~1 and ~15 m-thick sections of the stratigraphy, including a diverse array of lithologic units belonging to M1–M4 (Fig. 10). Another possible outcrop containing geyserite was discovered at approximately the same stratigraphic level ~40 m to the west, on the edge of the adjacent ridge (MVK14-034: Fig. 10).

At locality 16N, a well-exposed, ~3 m-thick section (16N: Fig. 10) contains geyserite along with a variety of sedimentary units and hydrothermal barite (Fig. 11). At the base of the section is a ~30 cm-thick, channelized unit of wrinkly laminated stromatolites that is composed of 1–3 mm-thick, wavy ferruginous (Fe oxyhydroxides) laminae interbedded with ~1 cm-thick units of microquartz (Fig. 12A–C). Wrinkly stromatolitic laminae are locally interbedded with, but in some places are cross-cut by, units containing the silicified remnants of small, lath-shaped (<10 μm long) crystals (Fig. 12C–F). These crystals are locally oriented perpendicular to bedding, but they are typically randomly distributed (Fig. 12D, E). Within the microquartz layers are beds with sand grains and minor intraclasts (Fig. 12G, H). Toward the bottom of the wrinkly laminates are thin (1–2 cm) units of finely crystalline, stratiform barite that transition along strike into veins that cut up through the stratigraphy into overlying units (Fig. 12A). Veins of barite and mesoquartz also cross-cut the wrinkly laminated+microquartz bedding (Fig. 12I).

Exceptionally well-preserved, botryoidal-stratiform geyserite was collected from a small ~4 × 2 cm-sized exposure (Fig. 3; Djokic *et al.*, 2017) that could not be traced along strike. The geyserite contains finely laminated (anatase+kaolinite-illite), siliceous, botryoidal features with smooth, rounded or turbinate to columnar shapes (Fig. 3B). Troughs between inferred geyserite botryoids are composed of a fine-

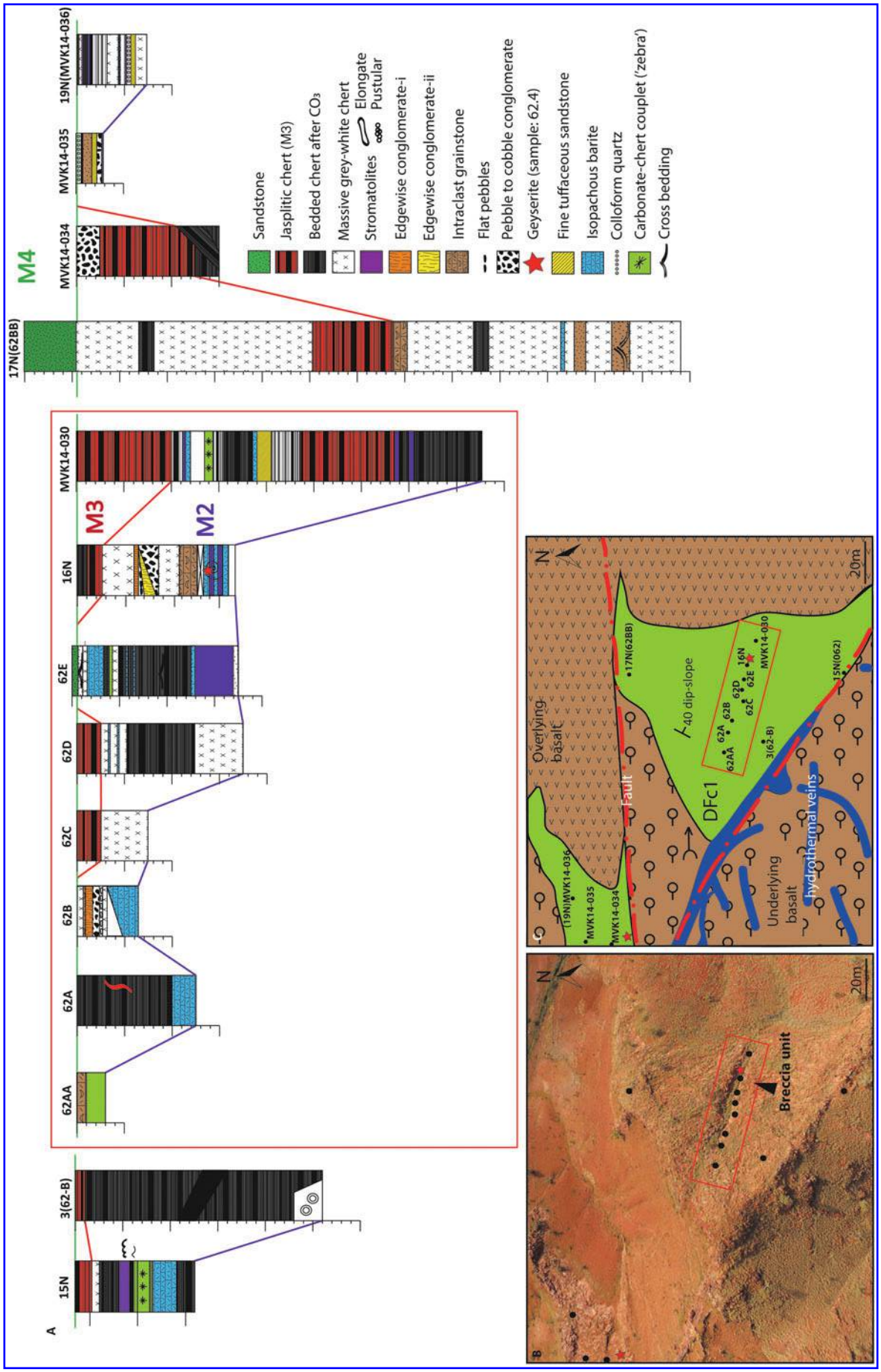

FIG. 10. (**A**) Lateral and temporal stratigraphy for local area around site 16N. (**B**) Aerial photograph of local outcrop area centered on the main ridge and gully. (**C**) Geological map of (**B**) with labeled locations of all stratigraphic sections measured and presented in (**A**).

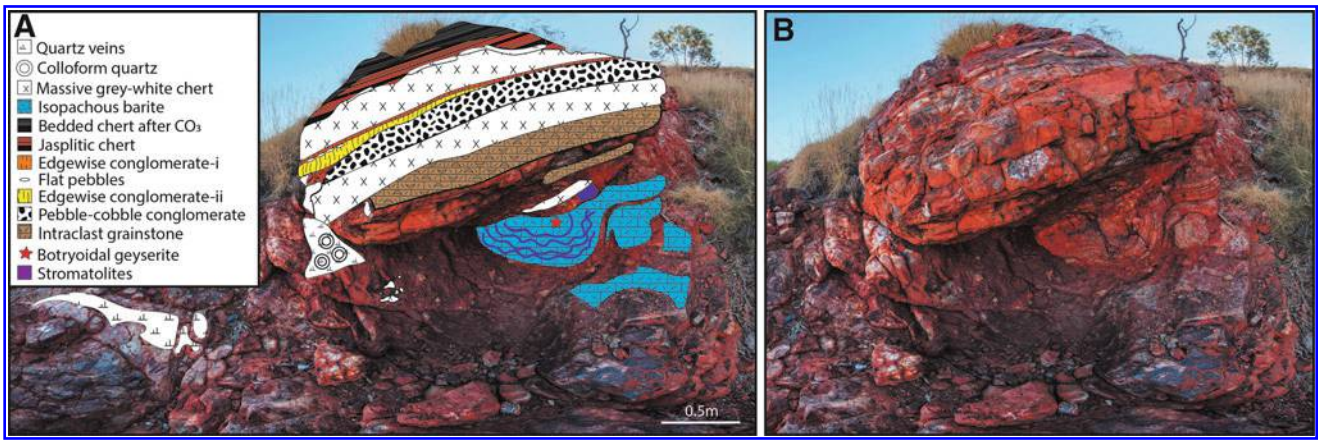

FIG. 11. Outcrop of measured section 16N **(A)** with and **(B)** without geological units illustrated.

grained (<25 μm), nonlaminated matrix of microquartz± kaolinite-illite (Fig. 3B; Djokic *et al.*, 2017).

Centimeter-thick ferruginous layers between beds of the botryoidal geyserite contain the mineralized remnants of round to collapsed bubbles rimmed by anatase and filled by later hydrothermal microquartz and barite (Fig. 13; Djokic *et al.*, 2017). Some bubbles preserve inward-radiating anatase crystal splays oriented from the rim toward the center of the spherical cavity (Djokic *et al.*, 2017).

Underlying the geyserite are wrinkly laminated stromatolites. Overlying the geyserite, from base to top, are: stromatolitic intraclast conglomerate (~40 cm thick); massive gray chert (~40 cm thick); a lens of rounded chert pebble conglomerate (up to 50 cm thick by ~2 m long); a lens (up to ~20 cm thick by ~1.5 m) of EC-ii; a ~5–10 cm-thick unit of rounded, white chert pebble conglomerate; and a thin (~10 cm) unit of EC-i. Overlying these units is a ~0.5 cm-thick unit of massive gray chert that is capped by a stratiform epithermal quartz vein, and overlain by a ~0.5 cm-thick unit of jasplitic chert of M3 (Fig. 11A).

Units here vary along strike over distances of only a few meters (Fig. 10). For example at 16N, stromatolitic intraclast conglomerate, EC-i and -ii, and pebble conglomerate extend for <10 m^2 and pass along strike into a breccia unit, described in Section 5.1 (Figs. 9 and 10B).

Approximately 60 m to the south of 16N, locality 15N lacks conglomerate or other hot spring deposits between the underlying unit of carbonate-chert couplets and the overlying jasplitic chert of M3 (Fig. 10). Approximately 15 m to the west of 16N, ECs are altogether absent and replaced by very fine-grained, cross-bedded sandstone, as well as by massive and bedded chert (*e.g.*, site 62E: Fig. 10).

In general, the most laterally discontinuous and thinnest units at the ''geyserite locality'' are ECs (usually ~5–20 cm thick) and stromatolitic intraclast conglomerate (max. 0.5 m thick). Pebble-to-cobble conglomerates are also thin (~10–15 cm) and are sparsely distributed as lensoidal, inferred channel deposits.

6.2. The barite curl (1S)

The ''barite curl'' locality lies at the topmost part of a wide (~5–10 m), very long (at least 250 m) black chert-barite vein located at the southern edge of the main Dresser Mine area. The locality is named after a ~10×3 m mass of coarse crystalline barite positioned at the very top of this vein. The barite mass is composed of two inward-curling sets of ~5–20 cm-thick, parallel to discordant, coarse-crystalline barite layers that are separated by thin seams of oxidized pyrite (Fig. 14; see also Djokic *et al.*, 2017). Individual barite layers within this mass are thick (~20 cm) at the center of each of the curls but become thinner toward the overlying sedimentary succession (Figs. 14C–F and 15A), where the tops of the coarse barite crystals have grown up into the base of these sedimentary layers. Wedge-shaped blocks, up to ~2 m long, of bedded gray–white chert with discordant, coarsely crystalline vein barite and gossan are suspended within the barite curl (Fig. 14C–F).

The sedimentary succession overlying the barite mass can be traced laterally for ~10 m along strike and includes, from base to top (Figs. 14G and 15A): a thinly (mm) bedded hematite-rich unit; sinter terracettes that contain internal palisade fabric with small, low-amplitude, domical stromatolites (Fig. 4; see also Djokic *et al.*, 2017); mm-thin beds of stratiform geyserite (Fig. 15B); and up to three beds of upward-branching, hematitic, shrub-like structures that lie within silicified beds of volcanic ash and volcanogenic sandstone (Fig. 15C, D). This succession is overlain by a 30–50 cm-thick unit of cm-bedded jasplitic chert of M3, and then by pillow basalt. A few meters to the southeast, at locality 1S (Fig. 14G), a small channelized deposit (~10 cm wide by <10 cm thick) of EC overlies the upward-branching, hematitic microbialites (Fig. 14H).

6.3. Stromatolite creek (site 23S)

The ''Stromatolite creek'' locality is situated ~3 km southwest of the Dresser Mine, and it is exposed over an area ~120×50 m along the edge of a small, unnamed creek bed (23S: Supplementary Figs. S1 and S2). This locality contains a diverse, ~3 m-thick succession that includes sedimentary, hot spring, and microbial facies of M2 that vary along strike over short distances of <5 m (Fig. 16). The generalized M2 stratigraphy includes, from base to top: the ''zebra rock''; black–white–gray bedded chert; stromatolites,

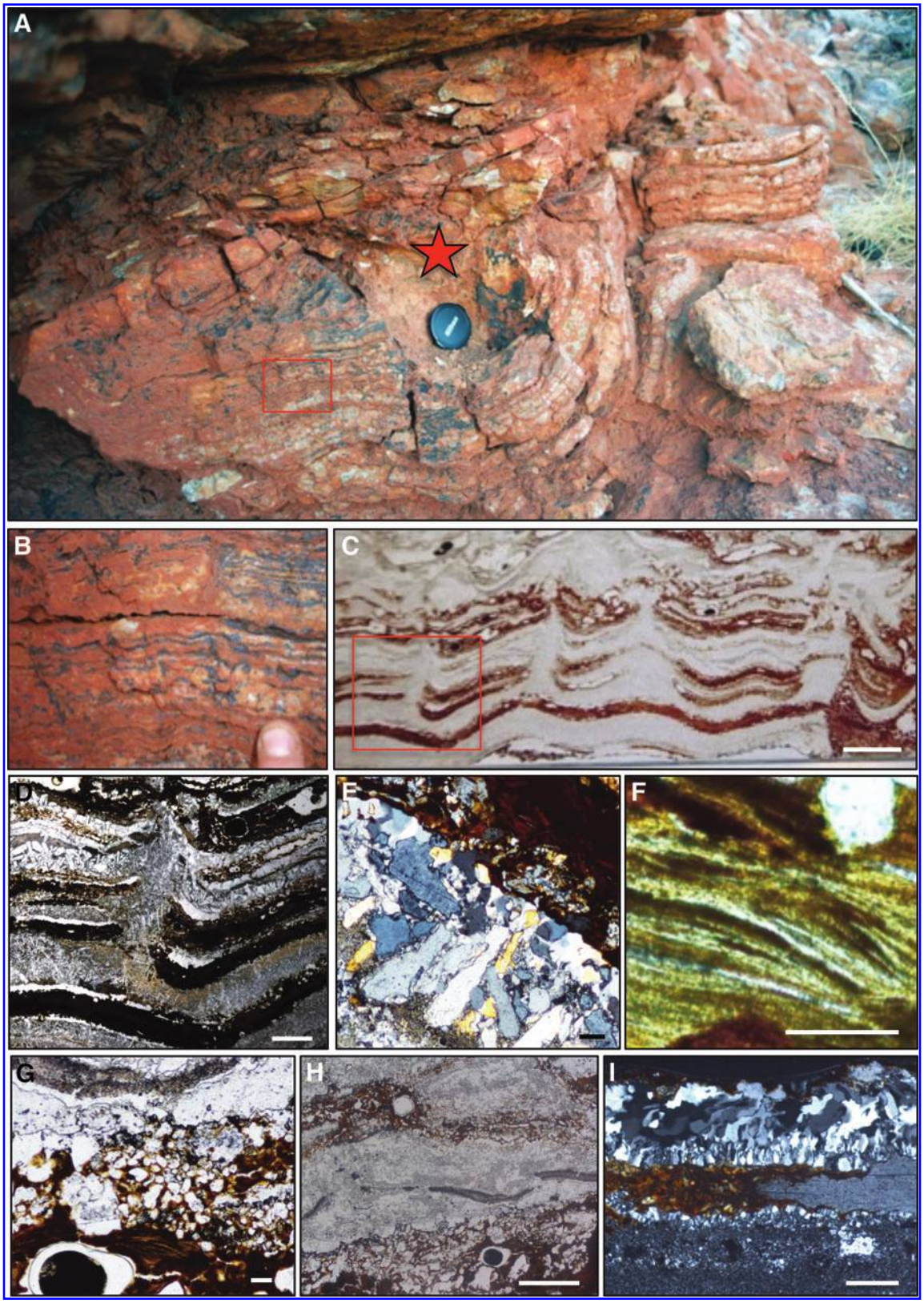

FIG. 12. Location of Dresser geyserite at 16N. Scale bar measurements and polarized light indicated. **(A)** Outcrop photo shows position where geyserite was discovered (star). Inset box; **(B)** black-red weathered wrinkly laminated stromatolites in outcrop. **(C)** Thin section of stromatolitic laminates (2 mm). Inset box; **(D)** wrinkly laminates cross-cut and interbedded by lath-shaped crystals (1 mm, ppl). **(E)** Silicified lath-shaped crystals (100 μm, xpl). **(F)** Internal microscopic laminae of stromatolitic unit (50 μm, ppl). **(G)** Sand grains (100 μm, ppl). **(H)** Intraclasts, possibly of sinter, interbedded with the wrinkly laminated stromatolites (1 mm, ppl). **(I)** Veins of barite cross-cutting stromatolitic laminae (300 μm, xpl).

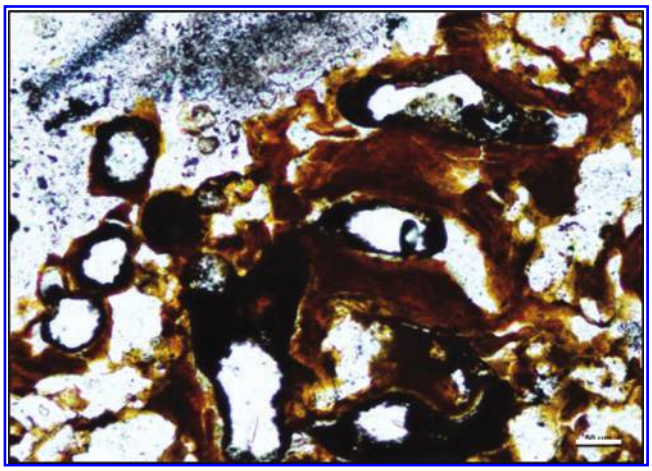

FIG. 13. Mineralized remnants of round to collapsed, and squashed bubbles within stromatolites associated with geyserite at site 16N (scale, 50 μm).

EC-i and -ii; and pebble-to-cobble conglomerate. Jasplitic chert of M3, and green sandstone of M4 overlie this succession.

A spectacular plan-view exposure of EC-i is exposed in a ~5×3 m, triangular-shaped outcrop. In this exposure, straight and curved or plastically deformed edgewise clasts (~1–2×5–40 cm) display distinct fanning arrays that are typically ~15–40 cm^2 (Fig. 17). Both types of EC at this locality display channelized distributions (Fig. 16C). For example, EC-i cuts down into stromatolites and pebble conglomerate, and it passes laterally northward into a channelized section of EC-ii.

A wide range of microbialite textures with a patchy distribution is present, and they outcrop as relatively thin units (<10 cm) that show variable morphology up-section and along strike (Figs. 16C and 18–20). This variability includes: irregularly undulating layers; distinct wrinkly-irregular layers with tear-like pockets and small, rounded, pore spaces now filled with microquartz (Fig. 18A); and randomly oriented polygonal desiccation cracks (Fig. 18B).

Pustular mat-like structures show either clumped, stubby pustules or layered, columnar to bulbous structures with internal, Fe-rich, mm-thick layering (Fig. 19).

Distinctive, elongated domical and conical stromatolites that are 2–3 cm wide and 5–10 cm long (Fig. 20) outcrop in patches over a distance of ~25 m and flank channelized ECs (Fig. 16C). Composed of fine-scale ferruginous laminae (Fig. 20C), the elongated stromatolites are separated by sediment fill that consists of ribbons and more equant shards of silicified felsic volcanic tuff, together with less abundant volcanic sand grains. The felsic volcanic ash blankets (~3 cm) these stromatolites and appears to have resulted in their demise at this locality (Fig. 20D). At the southwestern edge of the valley (locality 24S), ~3 cm-high, coniform stromatolites that exhibit Fe-rich, eggshell-like laminae are preserved within hydrothermal barite (Fig. 20E).

7. Trace Element Geochemistry

REE + Y were analyzed from the interpreted Dresser hot spring sinter deposits to complement field and petrographic data pertaining to their origin as terrestrial hot spring deposits. For comparison, REE + Y were analyzed from Phanerozoic subaerial hot spring sinters, including modern samples from New Zealand and Yellowstone National Park (USA), and Devonian sinters from the Drummond Basin in Australia.

In addition, REE + Y were analyzed from a partially silicified, stromatolitic dolomite sample from the ~3.4 Ga Strelley Pool Formation for comparison with documented Archean seawater signatures (see Van Kranendonk *et al.*, 2003; Bolhar *et al.*, 2005; Allwood *et al.*, 2010).

REE + Y data are presented in both Mud of Queensland (MUQ)- and Chondrite- normalized diagrams. The use of MUQ normalization as an upper continental crust estimate (Kamber *et al.*, 2005) to recognize marine precursors in this study is based on the rationale presented in Bolhar *et al.* (2005). To summarize, MUQ derives from riverine catchments that incorporate a high basaltic contribution, which may better reflect Archean environments that were dominated by basaltic rocks. This contrasts to the more widely used PAAS (Post-Archean Average Shale: McLennan, 1989), which derives from weathering of more intermediate igneous compositions. As well as the input from riverine catchment waters, REE + Y patterns of marine precipitates reflect seawater scavenging processes and hydrothermal fluid-rock interactions at oceanic spreading ridges (Elderfield, 1988; Van Kranendonk *et al.*, 2003 and references therein).

Chondrite-normalized REE + Y plots (Taylor and McLennan, 1985) are provided for comparison of the putative Dresser geyserite with Phanerozoic hot spring deposits. This is based on the observation that REE + Y patterns of Phanerozoic sinters reflect their igneous host rock composition due to water–bedrock interaction (Lewis *et al.*, 1997). Since REE + Y data for igneous rocks are often normalized to abundances in chondritic meteorites (*i.e.*, a commonly inferred bulk composition of Earth: Mason and Moore, 1966), we will also chondrite-normalize putative Dresser hot spring sinters.

MUQ-normalized REE + Y plots of Dresser botryoidal geyserite ($n = 2$: GEYSERITE-1; GEYSERITE-2) display relatively flat patterns with slightly enriched LREE (Pr/Yb = 1.19, 1.59; Nd/Yb = 0.80, 1.05), relatively depleted Ce, a weak La anomaly (La/La* = avg. 1.17), absent Gd or Er anomalies, and low Y/Ho ratios (~28.7, 31.4) (Fig. 21A; Supplementary Table S1). Samples show absent to small positive Eu anomalies (Eu/Eu* = 1.52**, 2.03), but due to the high abundance of barium in GEYSERITE-1** (Ba/Eu >100,000), the positive Eu may be unreliable by up to 20%. This error can be caused by potential isobaric interference on Eu by Ba (*e.g.*, $^{135}Ba^{16}O$ and $^{137}Ba^{16}O$ on ^{151}Eu and ^{153}Eu, respectively; Greaves *et al.*, 1989). For comparison, MUQ-normalized REE + Y plots of Phanerozoic hot spring sinter deposits ($n = 14$: Devonian-Carboniferous Drummond Basin, Australia; modern-Pleistocene Taupo and Coromandel volcanic zones, New Zealand; modern-recent sites at Yellowstone National Park (USA) exhibit similar, relatively flat patterns (Pr/Yb = avg. 1.12; Nd/Yb = avg. 0.99) with absent, or weakly positive La (La/La* = avg. 1), Gd and Er anomalies, and low, but variable Y/Ho ratios (avg. ~27) (Fig. 21A; Supplementary Fig. S7; Supplementary Table S1).

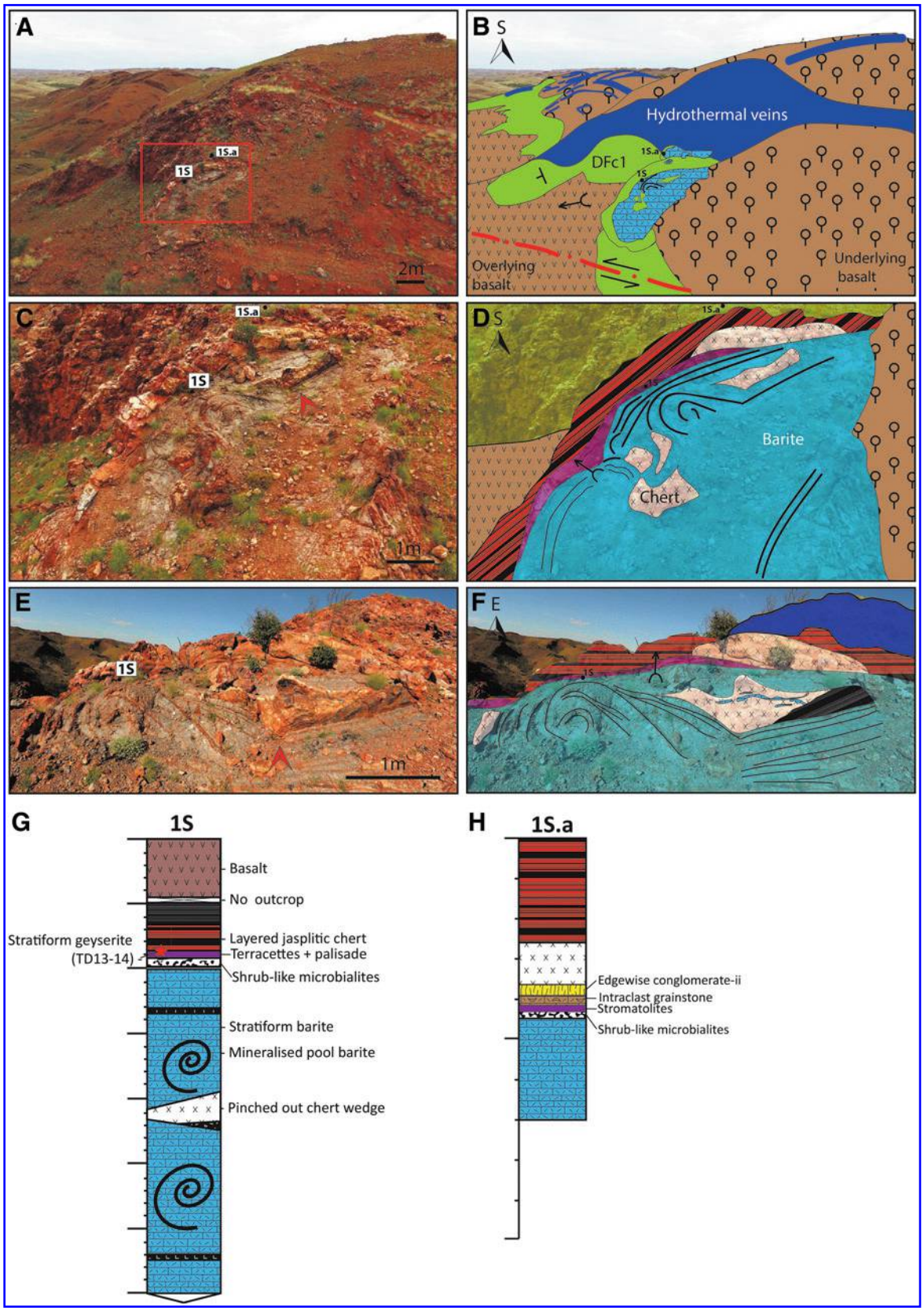

FIG. 14. Outcrop of site 1S. **(A)** Aerial view looking south toward site 1S, showing location of measured sections. **(B)** Geological map of **(A)**. **(C)** Close up view of inset box from **(A)**. **(D)** Geological map of **(C)**. **(E)** Close up view of the barite curl at site 1S showing pinched out chert wedge. **(F)** Geological units in **(E)**. **(G,H)** Stratigraphy at site 1S.

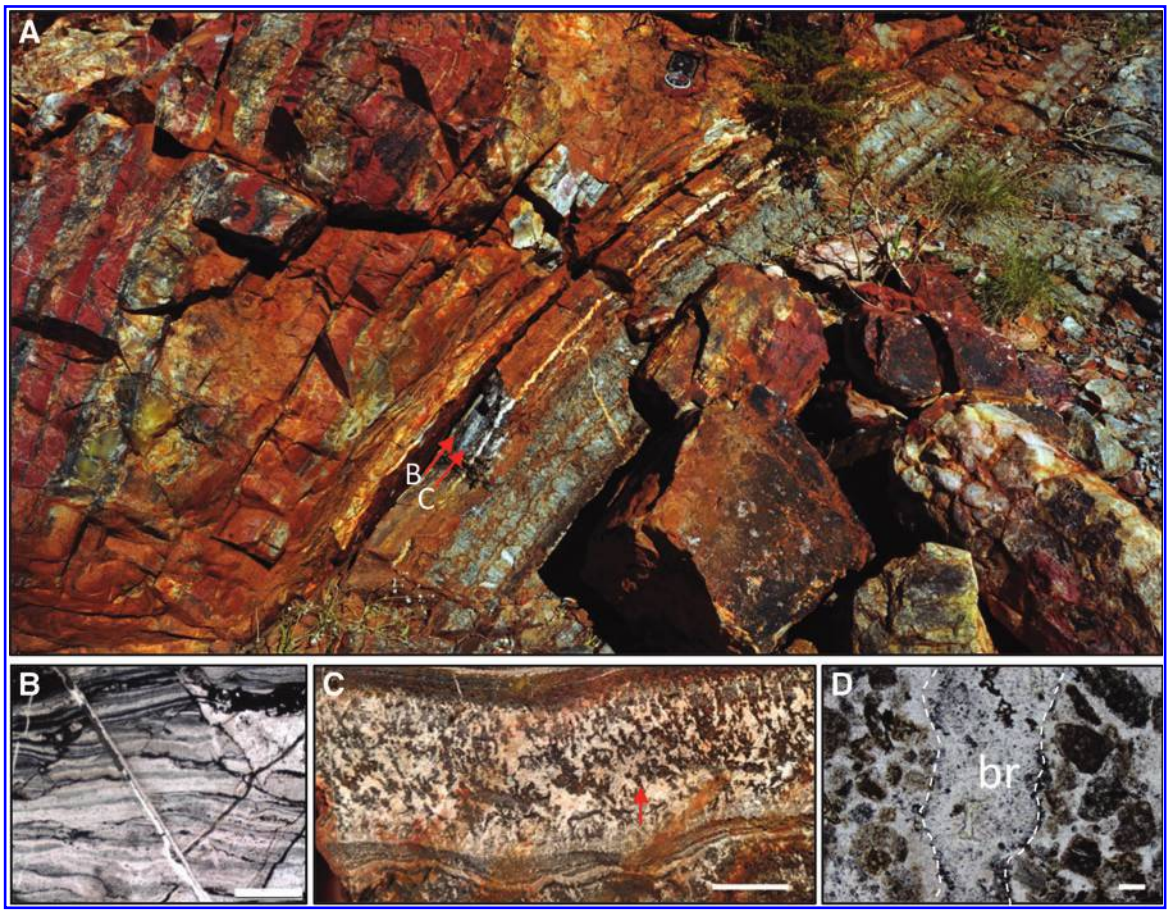

FIG. 15. Key textures at measured section 1S. Scale bar measurements and polarized light indicated. **(A)** Outcrop photo. Red arrows indicate location of parts **(B)** and **(C)** of this figure. **(B)** Thin (mm) beds of stratiform geyserite (1 mm, ppl). **(C)** Hand sample displaying upward-branching, hematitic, shrub-like microbialites (1 cm). **(D)** Single branch (br) of shrub growing upward through sediment (100 μm, ppl).

Chondrite-normalized Dresser geyserite REE + Y patterns are also remarkably similar to the Phanerozoic sinters (Fig. 21A). Dresser geyserite and the Phanerozoic sinters display consistently distinct LREE enrichment compared with MREE and HREE (*i.e.*, La/Lu = avg. 19.9 and ~10.6, respectively: Supplementary Table S1; Supplementary Fig. S7).

Each suite of the Phanerozoic sinters varies slightly from one another as a result of deposition associated with different host rocks (Ewers *et al.*, 1992; Christianson, 2001; Wilson and Rowland, 2016). New Zealand and Yellowstone National Park sinters, for example, display negative Eu anomalies, whereas Devonian Drummond Basin sinters have no Eu anomaly and show variable behavior of Ce and Y (Fig. 21A; Supplementary Fig. S7). However, a key point from these data is that all Phanerozoic sinter samples have REE + Y patterns that closely resemble those of their igneous host rocks (*e.g.*, Hopf, 1993; Christianson, 2001; Supplementary Fig. S7).

In contrast to the Dresser geyserite and Phanerozoic sinters, the MUQ-normalized REE + Y plot of a Strelley Pool Formation marine stromatolitic dolomite is characterized by a typical Archean seawater pattern (Fig. 21; *e.g.*, Van Kranendonk *et al.*, 2003) that displays depleted LREE, enriched HREE relative to MREE (Pr/Yb = 0.10; Nd/Yb = 0.12), small positive Gd and Er anomalies, a positive La anomaly (La/La* = 3.35), and superchondritic Y/Ho (81) (Fig. 21B; Supplementary Table S1).

Chondrite-normalized REE + Y plots of Dresser geyserite also markedly contrast with Strelley Pool Chert stromatolites. Dresser geyserite shows enrichment in LREE (La/Lu = 16.5, 21.9) and flattening out over MREE to HREE, whereas the Strelley Pool sample is depleted in LREE (La/Lu = 1.21, apart from a positive La anomaly) and shows enriched HREE (Fig. 21B).

8. Discussion

8.1. A terrestrial origin of Dresser putative geyserite?

Previous studies have indicated a submerged hydrothermal vent setting for at least part of DFc1 based on the presence of barite veins that curl upward and over into stromatolitic horizons (Van Kranendonk, 2006, 2011). These observations were used to suggest that microbial communities may have exploited chemical-rich fluids made available from a white smoker-type hydrothermal vent setting. Therefore, here we will consider more carefully whether the interpreted subaerial hot spring geyserite deposits of DFc1 (Djokic *et al.*, 2017) could instead represent the product of subaqueous hydrothermal venting.

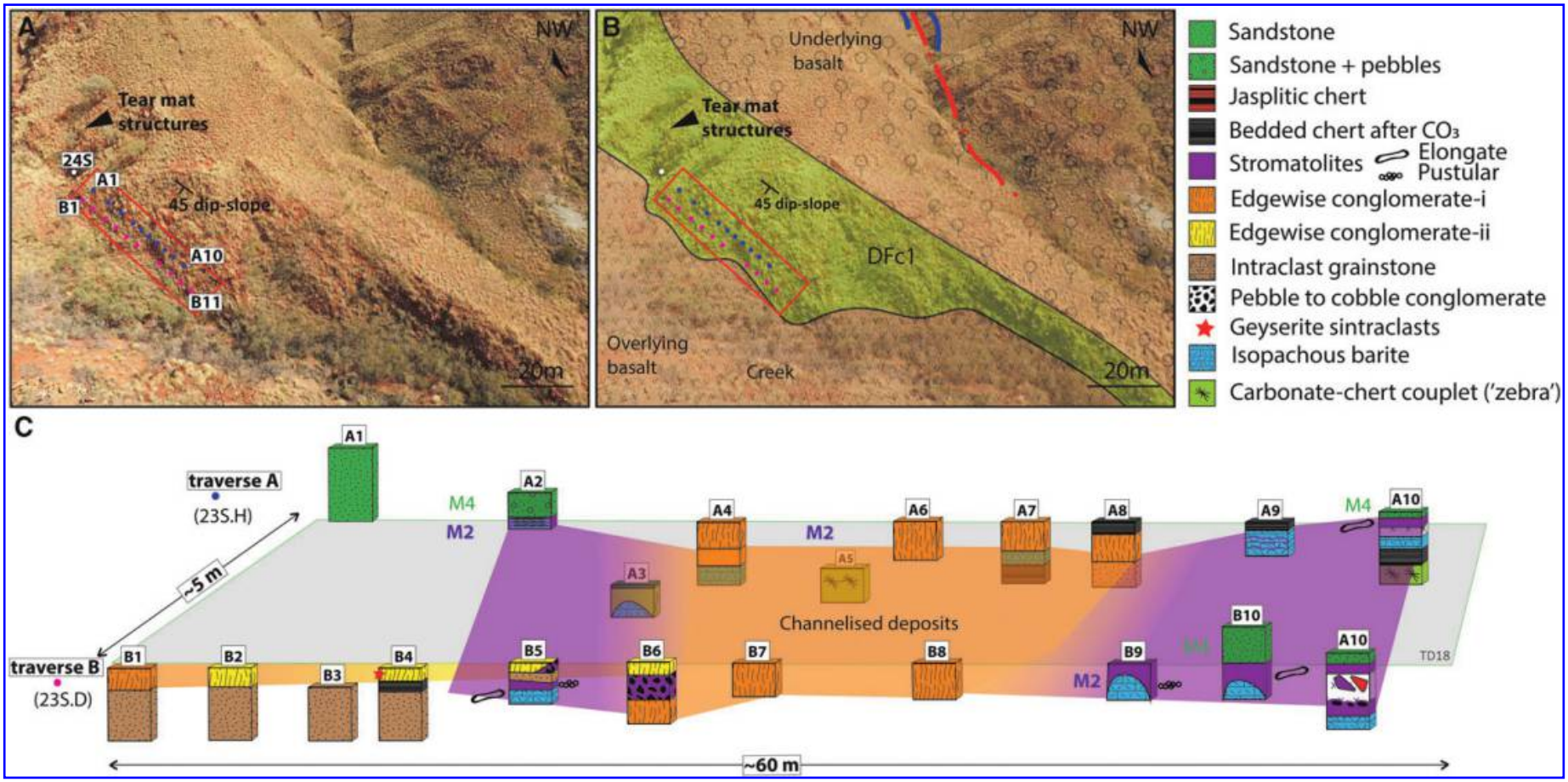

FIG. 16. Outcrop of site 23S. **(A)** Aerial view of site 1S, showing location of measured sections. **(B)** Geological map of **(A)**. **(C)** Lateral and vertical stratigraphy for area around site 23S, showing channelized deposits.

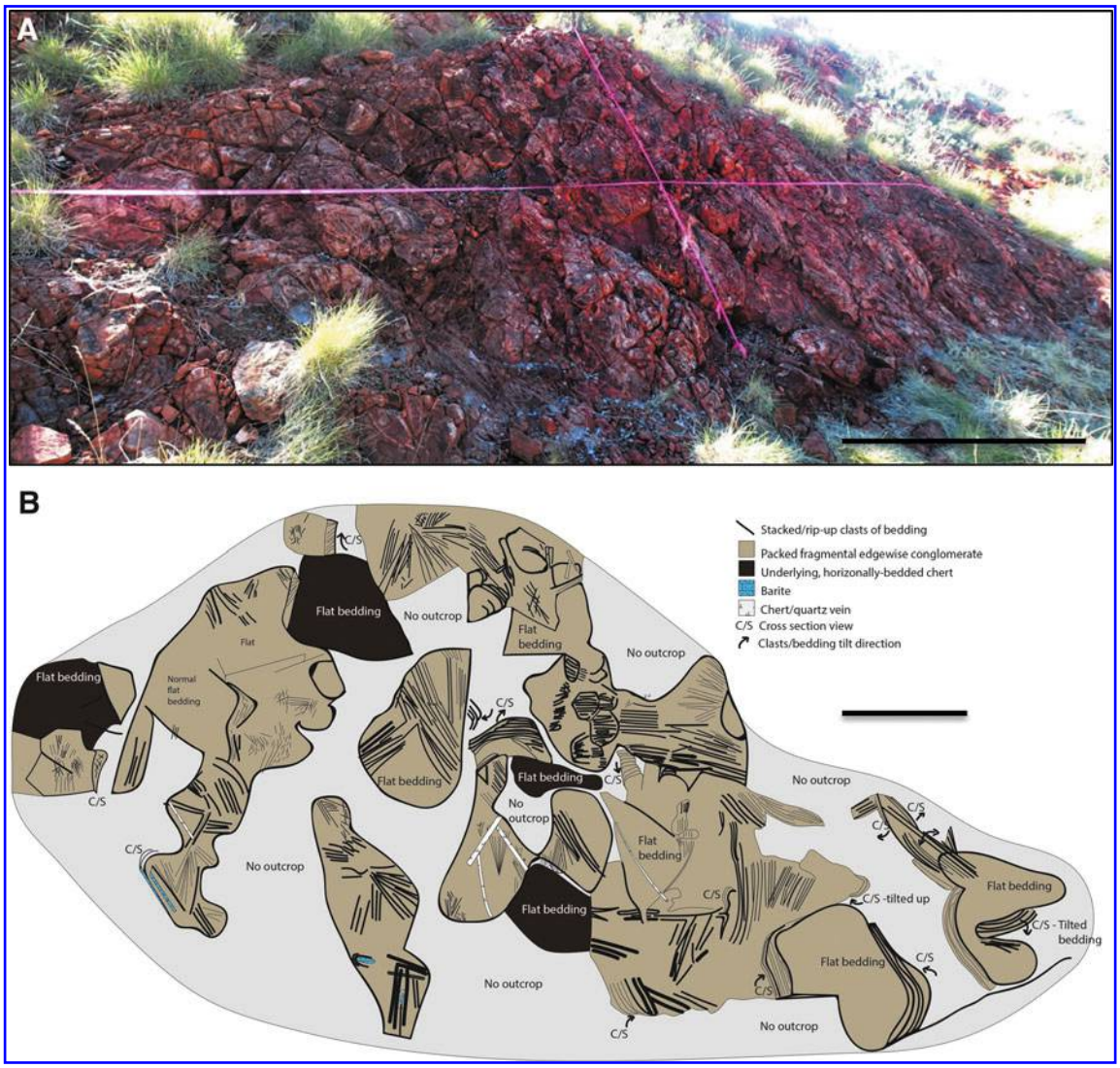

FIG. 17. **(A)** Outcrop image of large triangular panel of EC-i at site 23S (scale bar, ~1 m). **(B)** Diagram illustrating the clast orientation of the EC-i panel. (scale bar, ~0.5 m).

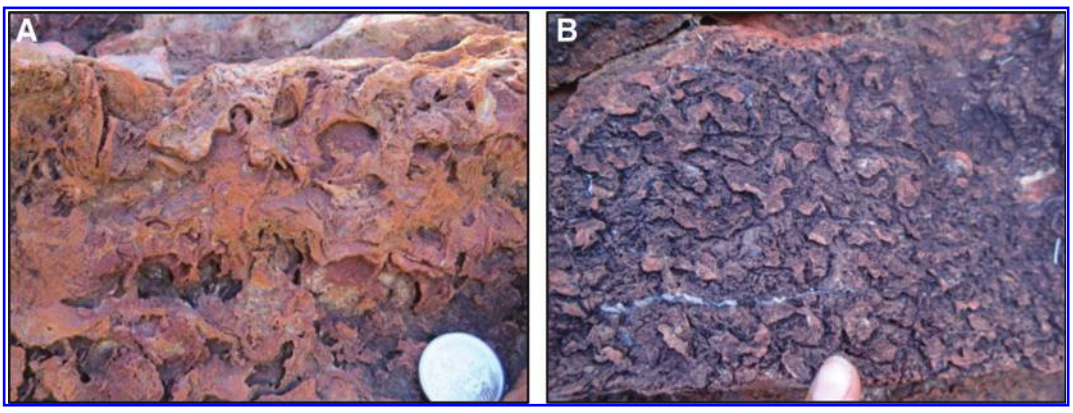

FIG. 18. Microbial mat structures from site 23S with **(A)** distinct wrinkly-irregular layers, tear-like pockets, and small, rounded, open spaces or **(B)** randomly oriented polygonal desiccation cracks.

FIG. 19. Pustular mats at site 23S. Scale bar measurements indicated. **(A,B)** Clumped stubby pustules (Cp). Hand sample of layered columnar (Lc) to bulbous structures in **(C)** oblique plan view (1 cm), and in **(D)** cross-section (1 cm).

Silica-rich (opal-A) deposits from known subaqueous hydrothermal environments include Si-rich, chimney structures at marine hydrothermal vents (Dekov *et al.*, 2015), passive silica laminates on hydrothermal lake floors (Renaut and Owen, 1988), and stromatolitic aggregates in marginal marine settings (*e.g.*, Canet *et al.*, 2005).

First, it has been shown that seawater is integral to the growth of Si-chimney structures and their composition, which includes strong mineralogical zonation from their cores to their outer crusts (Sun *et al.*, 2012; Dekov *et al.*, 2015). In contrast, Dresser geyserite lacks such compositional zoning, and it instead displays distinctive botryoidal textures with extremely fine grained (1–10 μm thick), microlaminated, dark/light couplets (2–30 μm thick) that are indicative of rapid precipitation through evaporative processes (Fig. 3; Campbell *et al.*, 2015a; see also Djokic *et al.*, 2017).

Such textures are also distinct from hydrothermal opal-A silica deposits forming in sublacustrine springs and stromatolitic aggregates depositing within marginal marine settings. In the former, laminations are completely absent (Renaut and Owen, 1988), and in the latter, laminations contain abundant detrital grains (*e.g.*, Canet *et al.*, 2005). Both features are markedly inconsistent with the Dresser geyserite.

Moreover, a comparison of the Dresser geyserite REE + Y to that from a modern low-temperature (55–71°C), subaqueous, opal-A hydrothermal vent chimney (Dekov *et al.*, 2015) shows marked differences. Dresser geyserite displays flat MUQ-normalized patterns with absent or minor La, Y, and Eu anomalies (Fig. 21B). The very minor Eu anomaly for sample GEYSERITE-1 is also possibly due to high abundance of Ba (Greaves *et al.*, 1989). In contrast, the Si-chimney displays LREE depletion (Pr/Yb = 1.85; Nd/Yb = avg. 2.41) with positive La and Y anomalies that are characteristic marine features (cf. SPC.1: Fig. 21A), and a strong positive Eu anomaly indicating high-T hydrothermal input (Fig. 21A; Bolhar *et al.*, 2005). Chondrite-normalized Dresser geyserite REE + Y displays strong LREE enrichment (La/Lu = avg. 19.18) and absent Eu anomalies

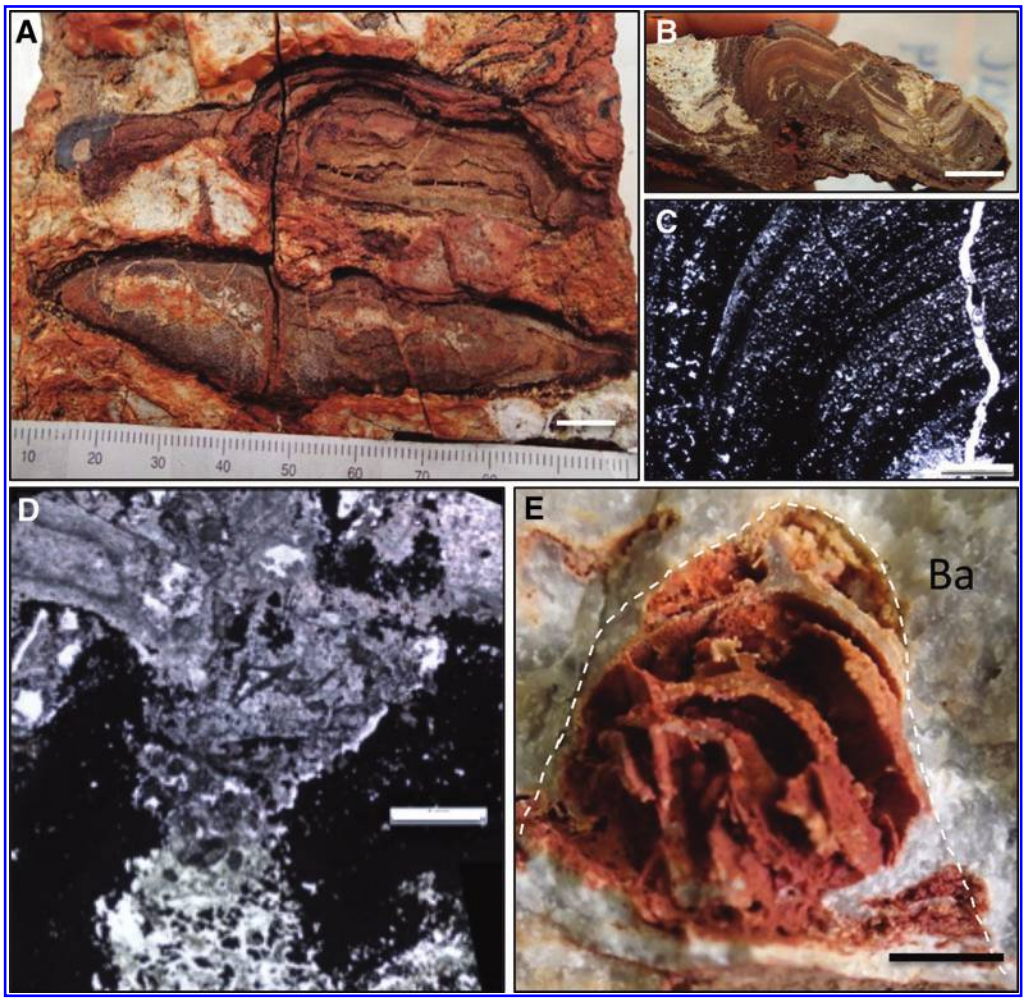

FIG. 20. Stromatolites at site 23S. Scale bar measurements and polarized light indicated. **(A)** Elongated domical and conical stromatolites (1 cm), and in **(B)** cross-section (1 cm). **(C)** Internal, fine-scale, black, dark brown, to cream–brown ferruginous laminae of elongated stromatolites (1 mm, ppl). **(D)** Sediment infill of ash and sand between elongated stromatolites (1 mm, ppl). **(E)** Coniform stromatolite with eggshell thin laminates set in barite (Ba) (1 cm).

compared with only slight LREE enrichment (La/Lu = 2.3) and a strong positive Eu anomaly (Eu/Eu* = 3.8) in the Si-chimney deposit (Dekov *et al.*, 2015). Likewise, REE + Y patterns of typical mid-ocean ridge (MOR) hydrothermal fluids are distinct from the Dresser geyserite (Fig. 21B; Douville *et al.*, 1999). Despite having both chondrite-normalized patterns with LREE enrichment, the strong Eu anomaly present in the MOR fluids is clearly absent in the Dresser geyserite. A strong Eu anomaly is characteristic of the high-T nature of MOR hydrothermal settings where vent sites are typically >200°C, and subsurface circulating fluids can reach ~700°C resulting in leaching of Eu from plagioclase (Elderfield, 1988; Douville *et al.*, 1999; Kelley *et al.*, 2002).

Instead, REE + Y patterns of the Dresser geyserite are remarkably similar to well-documented Phanerozoic subaerial sinter deposits, which display $LREE_{CHON}$ enrichment and lack positive Eu_{CHON} (Fig. 21A; also see Lewis *et al.*, 1997; Uysal *et al.*, 2011). The latter point is consistent with the temperatures exhibited by hydrothermal fluids in subaerial geothermal fields (typically 100°C at the surface and <300°C in the subsurface; for example, Harris *et al.*, 2009; Campbell *et al.*, 2015a).

Together, these observations discount a subaqueous and/or submarine hydrothermal vent origin (cf. Haymon *et al.*, 1981) for the Dresser geyserite, and they instead strongly support its formation as subaerial hot spring geyserite (Djokic *et al.*, 2017).

8.2. A terrestrial geothermal field in the Dresser Formation

The focus here is on the setting of the relatively thin and highly variable succession within M2 that contains the interpreted hot spring and associated facies. Detailed examination of M2 reveals common and widespread features of very shallow water, including ripples, desiccation cracks, and evaporative crystal splays (Fig. 18B; Supplementary Fig. S3B, Groves *et al.*, 1981; Buick and Dunlop, 1990; Van Kranendonk and Pirajno, 2004; Van Kranendonk, 2006). These features can form in either shallow marine or evaporative fluvio-lacustrine settings (Campbell *et al.*,

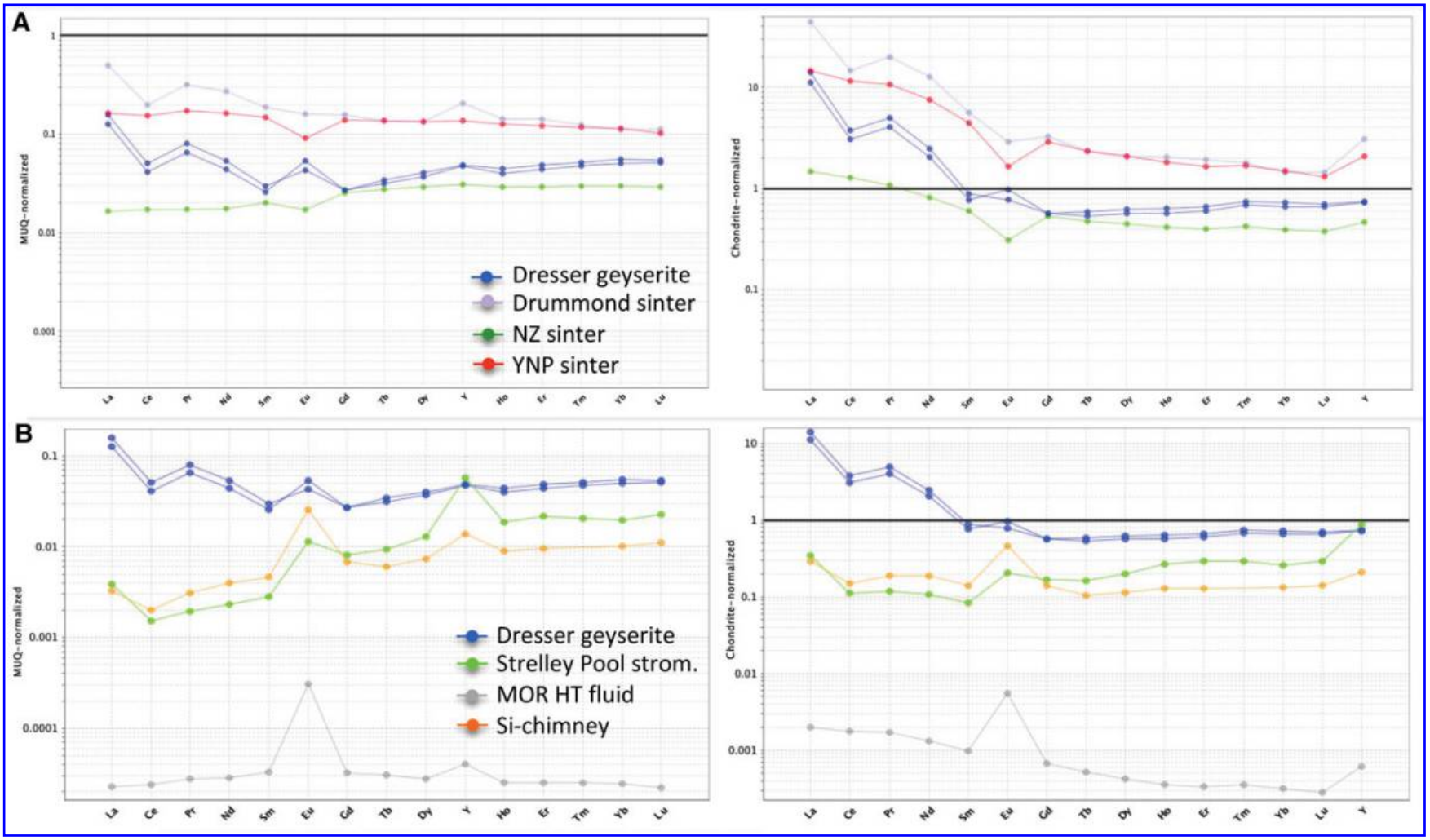

FIG. 21. **(A)** MUQ- and chondrite-normalized plots of Dresser geyserite samples versus Phanerozoic sinter samples from the Devonian Drummond Basin of Queensland Australia, New Zealand (NZ), and YNP, USA. For Phanerozoic sinter sample data see Supplementary Table S1: Drummond Basin sample 28.2/6/92; YNP sample NGB-8-18; NZ sample TD16-UMA-SINTER. **(B)** MUQ- and chondrite-normalized plots of Dresser geyserite samples versus plots of a partially silicified, Strelley Pool stromatolitic carbonate, a mid-ocean ridge hydrothermal fluid from the East Pacific Rise (MOR fluid) (Data from Douville *et al.*, 1999: sample ND17G2), and a submarine Si-rich hydrothermal vent chimney (Si-chimney) (Data from Dekov *et al.*, 2015). MOR, mid-ocean ridge; MUQ, Mud of Queensland; YNP, Yellowstone National Park.

2004; Guido and Campbell, 2009; Jahnert and Collins, 2012).

At the base of M2, rippled sandstone is overlain by the carbonate-chert ''zebra rock''. Evaporative crystal casts in the ''zebra rock'' were recently interpreted as after aragonite (Van Kranendonk *et al.*, 2003; Otálora *et al.*, 2018). Textural evidence, $\delta^{13}C_{carb}$ values, and REE + Y data, combined with high Fe, Mn, Ba, and Zn contents of the ankerite within the ''zebra rock'' indicate evaporative concentration of anoxic Archean seawater that was heavily influenced by a hydrothermal fluid component (Van Kranendonk *et al.*, 2003, 2018, 2020; Lindsay *et al.*, 2005).

Such observations, in combination with the widespread ($\sim$10 km) distribution of the ''zebra rock'' across DFc1, support previous interpretations that suggest deposition occurred within an evaporative, semi-enclosed basin (cf. Buick, 1985). However, the strong hydrothermal component and less pronounced La and Y anomalies (Van Kranendonk *et al.*, 2003 cf. Allwood *et al.*, 2010) are inconsistent with a solely marine, lagoon setting.

Rather, a shallow alkaline volcanic lake (or lakes), subject to hydrothermal and fluctuating hydrological conditions, may better explain the origin of the ''zebra rock.'' Alkaline volcanic lakes are hydrothermally fed, can have high daily evaporation rates (*e.g.*, 20 mm/day: Dawson, 2008), produce evaporative carbonate crystals such as aragonite (*e.g.*, Lake Venere, Italy: Cangemi *et al.*, 2010; Christenson *et al.*, 2015), and span tens of kilometers (*e.g.*, Lake Natron, East African Rift Zone: Christenson *et al.*, 2015).

An upward transition from the ''zebra rock'' unit to rippled sandstone and stromatolites suggests, through the application of Walther's law, a shallowing upward sequence in which stromatolites occupied the shoreline of one or more caldera lakes (Supplementary Fig. S2).

The morphological variety of the stromatolites and their patchy distribution—as observed both regionally (Supplementary Fig. S2) and locally (Figs. 10, 14, and 16)—is consistent with a highly variable and unstable volcanic-hydrothermal environment (*e.g.*, Kremer *et al.*, 2012), rather than a marine setting. Djokic (2015) pointed out that Dresser stromatolites generally display morphological variation over lateral distances of one to tens of meters, as well as variable stromatolite morphologies up-section over centimeters to decimeters (Figs. 10, 14, and 16; Supplementary Fig. S2); whereas stromatolites from marine settings, both modern and fossil, display lateral continuity and zoning across hundreds of meters to hundreds of kilometers, in 10 to100-m thick successions, as a result of reef dynamics and water depth (*e.g.*, Hamelin Pool, Shark Bay and the c. 3.4 Ga Strelley Pool Formation of the Pilbara Craton, Western Australia: Walter, 1976; Allwood *et al.*, 2006; Van Kranendonk, 2011; Jahnert and Collins, 2012). The presence of channelized deposits of rounded pebble and ECs infer fluvial settings, including rivers, creeks, or streams (Figs. 10, 11, 16, and 17), which are a common component of Phanerozoic geothermal fields (Campbell *et al.*, 2004; Guido and Campbell, 2009; Drake *et al.*, 2014). Periodic, low-volume, felsic eruptives locally buried (and likely stifled) Dresser stromatolites within these inferred fluvial settings (*e.g.*, locality 23S: Fig. 20). In geothermal systems, fluvial and lacustrine settings (such as is interpreted for the Dresser Formation from channelized conglomerates and the ''zebra rock'') are common and are influenced by input from hydrothermal fluids, including a magmatic component (Walter, 1976; Renaut *et al.*, 2002; Guido and Campbell, 2011).

The overall abruptly, changing litho- and bio-facies associated with Dresser Formation hot spring deposits in M2 is strongly consistent with geothermal fields (Section 6; Supplementary Fig. S2). Studies of Phanerozoic subaerial hot spring systems show that fluid compositions may vary over short distances (10's–100's m) and over relatively short timeframes (years, to decades). Fluid fluctuations cause a highly variable temperature regime that periodically will promote or diminish microbial colonization (Guidry and Chafetz, 2003a).

Surface changes can occur relatively quickly (months to years), such that thermal features may transition from springs to fumaroles, or geysers to quiescent pools (Guidry and Chafetz, 2003a). For these reasons, hot spring facies models are complicated, resulting in confined and highly variable bio- and litho-facies distributions controlled by the ever-changing, variable, and unstable geothermal environment (Guidry and Chafetz, 2003a).

Djokic (2015) argued that the rapid (meter-scale) facies variability observed in M2 displays a similar complicated and variable model and distinguishes M2 as a hot spring setting. In Yellowstone National Park ''no models can completely describe the tremendous variability observed in all siliceous hot springs'' (Guidry and Chafetz, 2003a, p. 78; Walter, 1976). At site 16N in the Dresser Formation, the transition from botryoidal geyserite to hydrothermally influenced edgewise and pebble conglomerates to sinter breccia (Fig. 10) is an example of rapidly changing conditions in an ancient hot spring setting, that is, from geysers, to hydrothermally fed rivers/streams, to drying spring apron surfaces. Changing conditions can also be inferred for site 23S, based on the abrupt spatiotemporal distribution of a wide variety of microbial textures that accompany inferred fluvial conglomerates, and hot spring deposits (Figs. 10, 14, and 16). Similarly, abrupt lateral facies changes are observed regionally across DFc1 stratigraphy, where units can rarely be traced along strike for more than a few meters (Supplementary Fig. S2; Nijman *et al.*, 1999; Van Kranendonk *et al.*, 2008; Djokic, 2015).

Possible evidence for explosive hydrothermal activity similar to that which occurs in modern geothermal fields (Browne and Lawless, 2001) is indicated from the presence of the distinct chert-barite breccia that first appears in M1 (Supplementary Fig. S3C–G). Previous studies referred to this chert-barite breccia unit as a boulder breccia (Buick, 1985), diamictite (Van Kranendonk, 2006), or volcaniclastic conglomerate (Djokic, 2015). Van Kranendonk *et al.* (2008) suggested that the unit could have derived as a fault breccia during episodes of block faulting. However, the features of the chert-barite breccia (Supplementary Fig. S3C–G) are also consistent with hydrothermal eruption breccias that display similar angular, unsorted blocks of surrounding lithologies set within a hydrothermally altered, unsorted matrix (Browne and Lawless, 2001). Explosive hydrothermal eruptions can occur either through the direct interaction of magma and water (phreatomagmatic) or through indirect interaction (phreatic) of magmatic heat and water/steam (Tămaș and Milési, 2003). The resultant energy released during these subsurface interactions can blast the country rock apart leaving behind

meters to hundreds of meters, and in some cases kilometers, of eruption breccia piles (Browne and Lawless, 2001). Often, these events develop eruption craters, a feature that due to the restricted and patchy exposures of the chert-barite breccia is so far unknown. Therefore, explosive hydrothermal activity in DFc1 represented by the chert-barite breccia is a possibility, but more work is warranted.

Epithermal-style hydrothermal alteration of the underlying basalts produced the local development of steam-heated acid-sulfate alteration (advanced argillic) at the Dresser Mine and in local pockets elsewhere along strike (Van Kranendonk and Pirajno, 2004). This advanced argillic alteration type can be used to infer the circulation of highly acidic fluids that would likely have formed mud pools and/or fumaroles at the land surface (*e.g.*, Bignall and Browne, 1994). However, these surface features have not been identified in the Dresser Formation.

Hot spring geyserite and fluid inclusion data from epithermal quartz (Harris *et al.*, 2009; Djokic *et al.*, 2017) indicates $<\sim 120°C$, near-neutral Ph, alkali-chloride hydrothermal fluids circulated at other times, and in other parts of the system. Alkali-chloride hot springs on modern Earth result in the formation of large hot spring pools, which accords well with the interpretation of large barite masses at the tops of hydrothermal chert-barite veins as representing the mineralized remnants of hot spring pools (Van Kranendonk, 2006; Djokic *et al.*, 2017; Van Kranendonk *et al.*, 2018).

Together, these observations strongly support the deposition of M2 within a terrestrial geothermal field, where microbial life thrived at the edges of hot spring pools and within hydrothermally influenced fluvio-lacustrine settings.

Below, key comparisons are made between hot spring related facies in the Dresser Formation and well-described components observed in proximal, middle, and distal vent facies of modern geothermal springs (Fig. 2; Walter, 1976; Cady and Farmer, 1996; Guidry and Chafetz, 2003a; Hinman and Walter, 2005).

8.2.1. Proximal vent facies. Proximal vent facies in the Dresser Formation are identified by a range of surface deposits. Foremost is the observation of geyserite at three separate localities across DFc1 (See Section 6). Features of the Dresser geyserite are characteristic of geyserite precipitation from modern, near-neutral pH, alkali-chloride hot spring fluids (Figs. 3 and 22; Campbell *et al.*, 2015a; Djokic *et al.*, 2017). Botryoidal textures in modern hot springs form most proximal to geyser and/or hot spring vent pool rims due to boiling (>90°C) of silica-saturated (>300 ppm) fluids that eject onto the edge of the pool and precipitate noncrystalline opaline silica (opal-A) through air-cooled spray (Fig. 20A, C, G; Campbell *et al.*, 2015a). Subsequent diagenesis transforms opal-A to microcrystalline (micro-)quartz through a series of silica mineral phase transitions (Rodgers *et al.*, 2004; Campbell *et al.*, 2015a).

Microlaminations in the Dresser geyserite display variable thicknesses across morphological types (Figs. 3 and 20A, D). Such microlaminae are similar to those observed in modern geyserite, where accretion is controlled by the rate of evaporative wicking and drying on surfaces reached by splashing and surging vent effluent. For example, preferential growth occurs fastest on high relief structures such as geyserite spicules and columns, which exhibit rapid, dense, localized accretion due to oversaturation of silicic acid (H_4SiO_4) as hot fluid drains from their tops (Fig. 20A, B; Campbell *et al.*, 2015a). In contrast, wavy to stratiform silica sinter polymerizes more slowly in subaqueous vent pools, resulting in slower accumulation rates and less dense precipitation of siliceous laminations (Fig. 20D, E; Walter, 1976; Lynne and Campbell, 2004; Campbell *et al.*, 2015a; Watts-Henwood *et al.*, 2017). This variation in silica precipitation is seen in Dresser geyserite, where the tops of botryoids show more densely precipitated microlaminations than in stratiform geyserite (Figs. 3B and 22A, D). Other textural features identical to modern geyserite include slump structures (Fig. 22D–F) and pool rim overgrowths (Djokic *et al.*, 2017).

Modern hot spring geyserite only occurs in vent mounds and at the edges of boiling pools, or as geyser eggs/beads or sintraclasts on the closely adjacent hot spring apron (Fig. 22G; White *et al.*, 1964; Walter, 1976). Similarly, Dresser geyserite is only found in cm-area patches (16N, 1S, 24S: Supplementary Fig. S1 and S2; Djokic *et al.*, 2017), or as sinter clasts intermixed in fluvial deposits (16N, 1S, 24S; Figs. 7C, 10, and 16).

The sparse distribution of Dresser geyserite, its association with riverine and fluvio-lacustrine sedimentary deposits (Djokic, 2015, this study; Djokic *et al.*, 2017), the numerous textural and mineralogical features identical to modern geyserite, and a non-marine, hydrothermal REE + Y pattern are all consistent with its formation in the proximal vent facies of subaerial hydrothermal springs (Fig. 22; Cady and Farmer, 1996; Guidry and Chafetz, 2003a; Campbell *et al.*, 2015a).

Former bubbles situated in layers interbedded with the Dresser botryoidal geyserite (Site 16N) were interpreted to have been trapped within microbial exopolymeric substance (EPS), similar to that observed in the mid-apron facies of modern sinter terraces (Fig. 13; Djokic *et al.*, 2017). Coated bubbles of carbon dioxide, methane, and/or oxygen are well known to rapidly mineralize in modern hot and cold springs (*e.g.*, Chafetz and Folk, 1984; Bonny and Jones, 2008a references therein).

The ancient bubbles described here may have been trapped in a lower temperature niche that occurred directly adjacent to and was physically protected from the higher-temperature, proximal vent facies forming geyserite, as occurs today in Yellowstone National Park (Fig. 22C; Supplementary Video S1) and New Zealand's Taupo Volcanic Zone (*e.g.*, Currie, 2005).

More recently, the bubbles were interpreted as volcanic glass vesicles, which form through the release of gas within volcanic rocks (Wacey *et al.*, 2018).

However, none of the Dresser bubbles are associated with volcanic rock. Indeed, at least two of the three examples of Dresser bubbles are from putative microbial units (Djokic *et al.*, 2017; Wacey *et al.*, 2018). The third occurrence is from a chert-barite breccia that also contains stromatolitic fragments (*i.e.*, chert-barite breccia: Supplementary Fig. S3B). Therefore, we maintain that the bubbles were preserved due to trapping in a sticky microbial exudate, *i.e.*, EPS.

8.2.2. Middle apron facies

8.2.2.1. Middle apron discharge channel facies. Middle apron hot springs facies in the Dresser Formation include discharge channel deposits (thermally influenced streams and creeks) represented by edgewise and stromatolitic intraclast

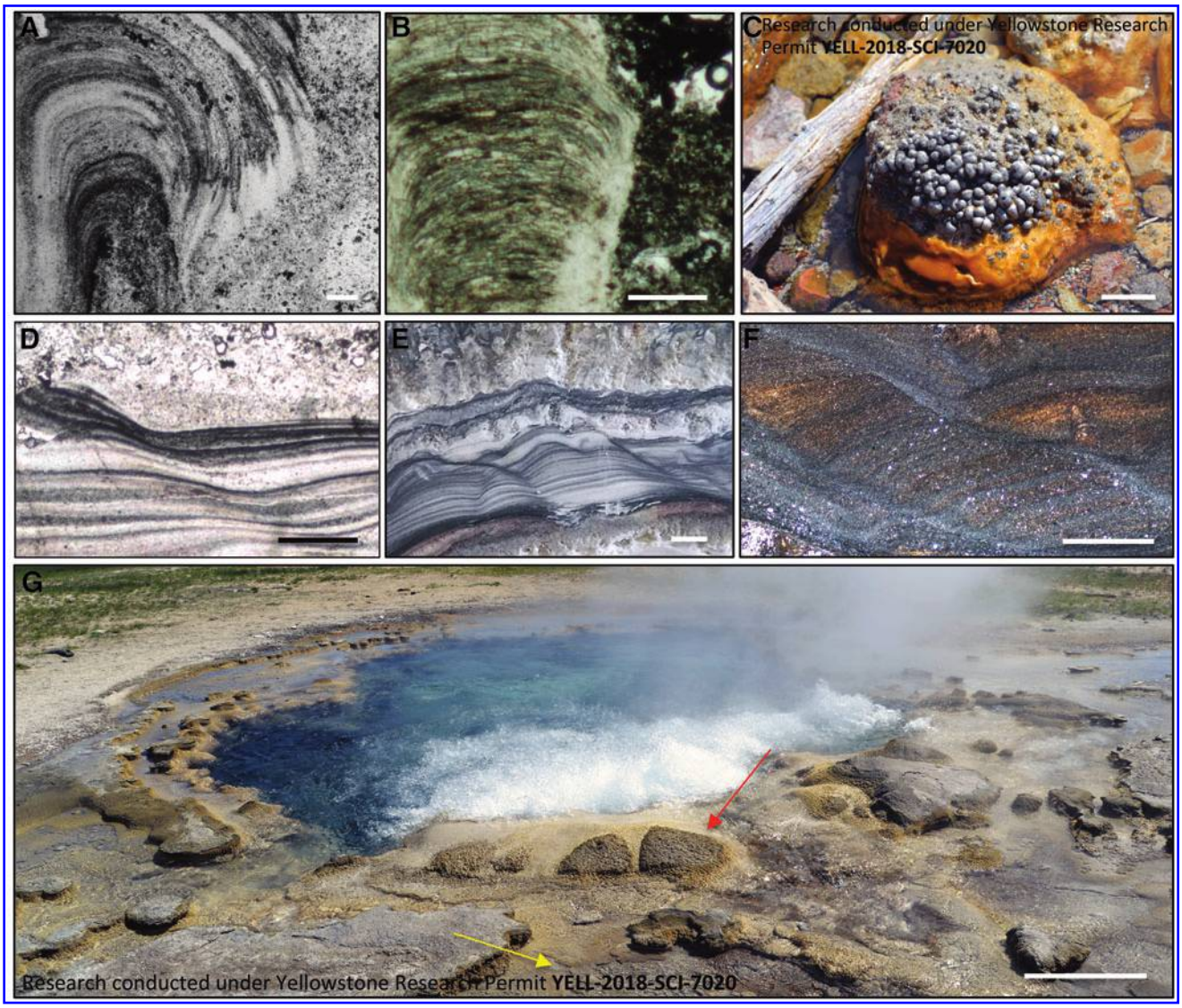

FIG. 22. Proximal vent facies—ancient and modern comparisons. Scale bar measurements and polarized light indicated. **(A)** Dresser geyserite cornices (100 μm, ppl) compared with **(B)** geyserite cornice from NZ sinter (250 μm, ppl). **(C)** Botryoidal geyserite with orange microbial mats growing in low-temperature niches at the base of a cobble adjacent to Boulder Geyser Creek, Lower Geyser Basin, YNP, USA (2 cm). **(D)** Slump textures in Dresser stratiform geyserite (500 μm, ppl) compared with **(E)** slump structures associated with NZ stratiform geyserite (500 μm). **(F)** Petrographic image of slump structures in **(E)** (500 μm, xpl). **(G)** Hot spring geyser pool in Lower Geyser Basin, YNP, USA. Red arrow—splash zone; columnar geyserite forming. Yellow arrow—pooling water; stratiform geyserite forming (0.5 m).

conglomerates. These Dresser conglomerate units are directly comparable with ''packed fragmental'' sinters from the modern Waimangu Volcanic Valley and c. 9.4 ka Mangatete sinter deposits of New Zealand (Fig. 23; Drake *et al.*, 2014: Fig. 5c; Guido and Campbell, 2011, p. 43), as well as from the Devonian Drummond Basin (Walter *et al.*, 1996).

Clasts in modern packed fragmental deposits display high aspect ratios, bent and contorted shapes with/without very fine internal layering, and thin sets of siliceous rinds that are all features comparable to the Dresser deposits (Figs. 5A–D, 6, 7, and 23; cf. Fig. 23B–E). High aspect ratios indicate limited reworking or transport. The flexible nature of the Dresser clasts implies a microbial component acting as a binding agent, allowing soft microbial mats to deform and bend, but not completely break before, and/or while undergoing desiccation or fluvial reworking during a storm or flood event (Figs. 5A, 6A, and 23E; Drake *et al.*, 2014). The coatings or rinds on clasts in the packed fragmental deposits represent adhesion or precipitation of silica around the clasts, deriving from hot spring fluids that flow over the sinter apron (Figs. 5D cf. 23D–E; Jones and Renaut, 1997).

Buick (1985) suggested that the Dresser stromatolitic intraclast conglomerate (''stromatoloidal intraclast rudite'': Buick 1985; Buick and Dunlop, 1990) was composed of carbonate muds ± organics (Dunlop *et al.*, 1978; see also Buick, 1985) and derived from stromatolitic units such as the thick, Fe-oxide weathered, wrinkly laminated stromatolites common in DFc1, which are preserved as pyrite in unweathered drill core (Van Kranendonk *et al.*, 2008).

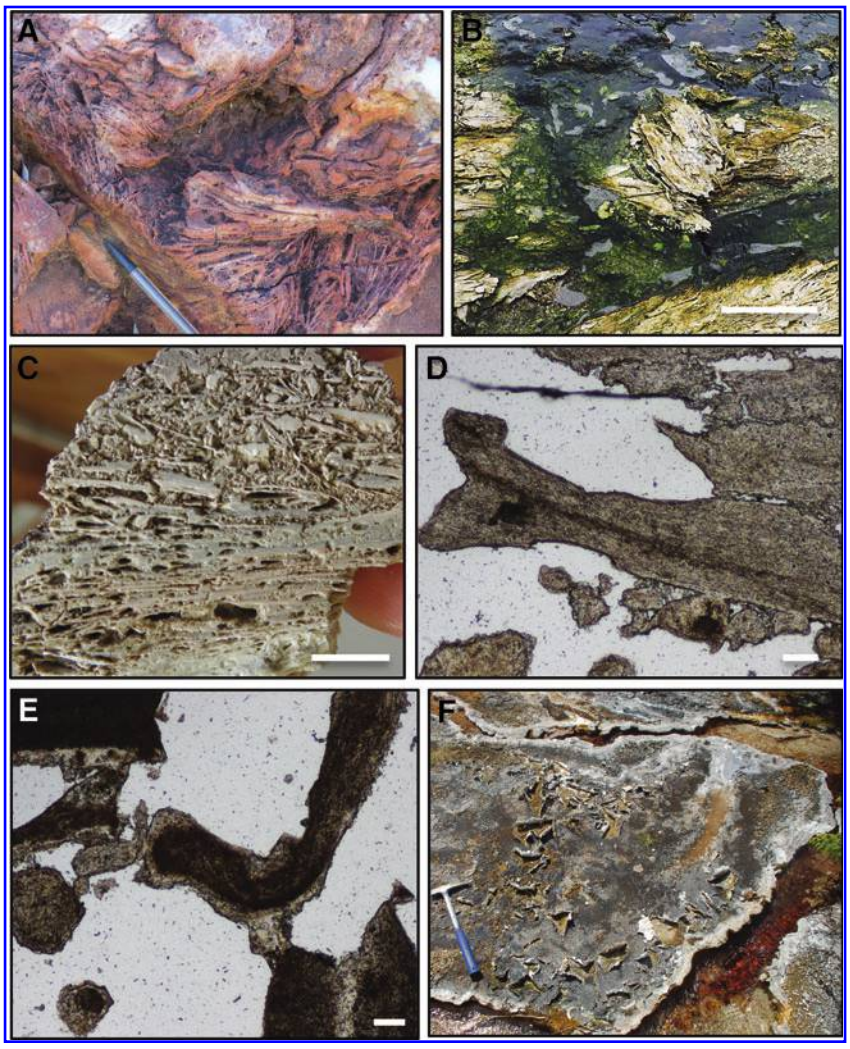

FIG. 23. Mid-apron sinter facies—ancient and modern comparison. Scale bar measurements and polarized light indicated. **(A)** Dresser geyserite EC-i compared with **(B)** packed fragmental facies at Waimangu Volcanic Valley, NZ (20 cm). **(C)** Hand sample of ~9 ka Mangatete packed fragmental sinter, NZ (1 cm). **(D)** Irregular (100 µm, ppl) and **(E)** bent (100 µm, ppl) clasts within Mangatete packed fragmental sinter. (F) Desiccated microbial mats, NZ.

However, the intraclasts are compositionally distinct from the wrinkly laminated stromatolites (Van Kranendonk *et al.*, 2008: Fig. 10), and they instead consist of fine-grained micaceous muds scattered with grains of microquartz, and coated by rinds containing Ti inferred as anatase from petrographic analysis (Fig. 5C, D). We concur with the microbial origin suggested by Buick (1985), but we add that the clast coatings resemble hydrothermal mineral rinds or weathering of clast surfaces (Figs. 5B–D cf. 23D, E; see also Guido and Campbell, 2019).

In situ silicification of clasts within hydrothermal streams or outflows has been documented (*e.g.*, Jones and Renaut, 1997). Alternately, silicification of clast weathering rinds is also known to occur (*e.g.*, Heller *et al.*, 2001).

However, the concentration of anatase (TiO_2) in some Dresser stromatolitic intraclast rinds (Fig. 5E) draws a compositional link with anatase, also found in the Dresser geyserite, and supports the hypothesis of *in situ* precipitation of these rinds from similar hydrothermal fluids.

The angularity of geyserite sinter clasts within EC-ii (Fig. 7C) implies limited reworking of such clasts and infers deposition only a short distance downstream from a near-neutral pH alkali-chloride hot spring vent (cf. Jones and Renaut, 2003; Campbell *et al.*, 2015a). The restricted presence of tourmaline in the long, thin clasts of EC-ii (Fig. 7B, D) suggests close proximity to a boron rich hot spring vent (*e.g.*, Ghosh *et al.*, 2012; Steller *et al.*, 2019).

The textural and compositional differences of the Dresser units (EC-i, EC-ii, stromatolitic intraclast conglomerate) appear to be a function of inputs from compositionally varied hot spring vents and pools as are known to develop within the sedimentary environments of New Zealand and Yellowstone National Park.

Variable mineralogy is also common in modern hot spring deposits, with precipitation of accessory minerals, including carbonate, gypsum, halite, jarosite, and aluminosilicate, reported for sinter (Jones and Renaut 2003).

Variations in the textures of packed fragmental hot spring sinters are caused by microbial mats that have undergone variable degrees of *in situ* silicification, such as in the mats that colonize the banks of hot spring outflow-fed creeks and streams (Guido and Campbell, 2011; Drake *et al.*, 2014). Erosion and reworking of the variably silicified mats occur not only due to fluctuations in the water table and tectonic activity but also commonly from seasonal storms and floods (Jones and Renaut, 2012). During drying events particularly in summer, microbial mats become partly to completely silicified and desiccate, commonly curling up into bent

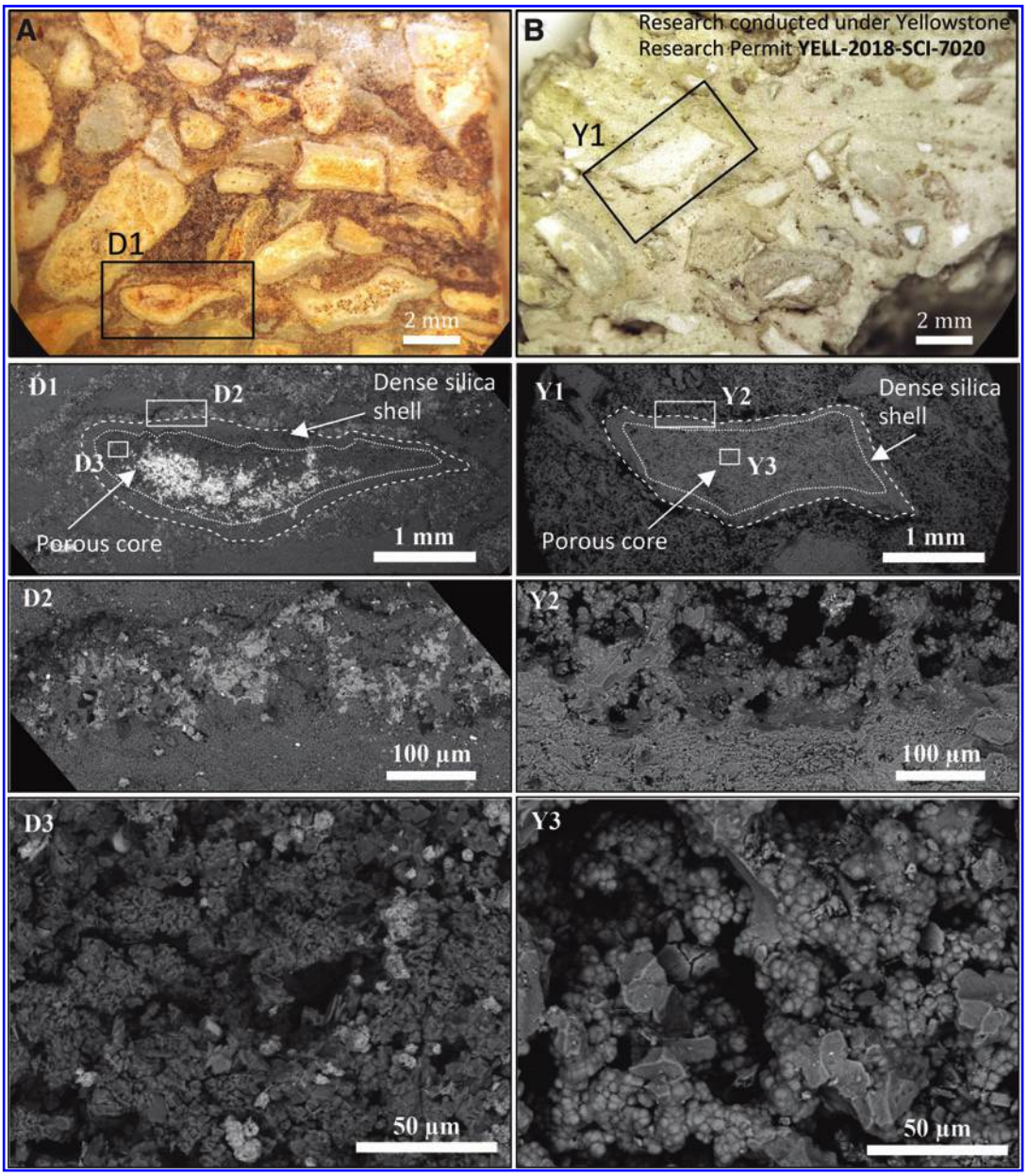

FIG. 24. **(A)** Hand sample image of Dresser Formation breccia unit (Fig. 9): hash, showing inset box indicating SEM image of single angular fragment (D1)—Dashed line represents outer edge (D2). Inner dotted line indicates transition between porous core (D3) composed of Fe-oxide (light gray)+barite (white) and the dense, fine-grained rim of silica (dark gray). **(B)** Hand sample image of sinter breccia from an extinct hot spring in Norris Geyser Basin, YNP, USA, showing inset box indicating SEM image of sinter breccia (Y1)—Outer dashed line represents outer edge of sinter fragment (Y2). Inner dotted line indicates transition between microbially derived porous sinter core now containing silica spheres (Y3) and the dense coating of silica. SEM, scanning electron microscopy.

fragments. During subsequent winter flooding and/or hot spring surge events, increased outflow flushes these dried-out mat fragments downstream, where they may settle at the bottom of creeks and/or accumulate in point bars as ''packed fragmental'' deposits (Fig. 23B; Supplementary Video S2; Drake *et al.*, 2014; Guido and Campbell, 2011). It is this latter formation mechanism that best explains the imbricated, fanning clast arrays in Dresser EC-i channelized deposits (Figs. 6A, 17, and 23A).

The final mid-apron facies deposit is the breccia unit described from the geyserite locality (16N), with porous Fe-oxide+barite-rich core zones of clasts that are coated by rims of fine-grained silica and Fe-rich silica (Figs. 9 and 24A). Although these blocky clasts resemble oncoids, they lack concentric layers coating a solid core (*e.g.*, Jones and Renaut, 1997; Peryt, 2012). Instead, this facies is more similar to brecciated intraclast sinter deposits known from New Zealand and Yellowstone National Park, which generate sinter fragments with the same internal primary porosity and external silica coatings (Fig. 24B).

These sinter breccias form when microbially precipitated sinter is broken up mechanically by periodic wetting and

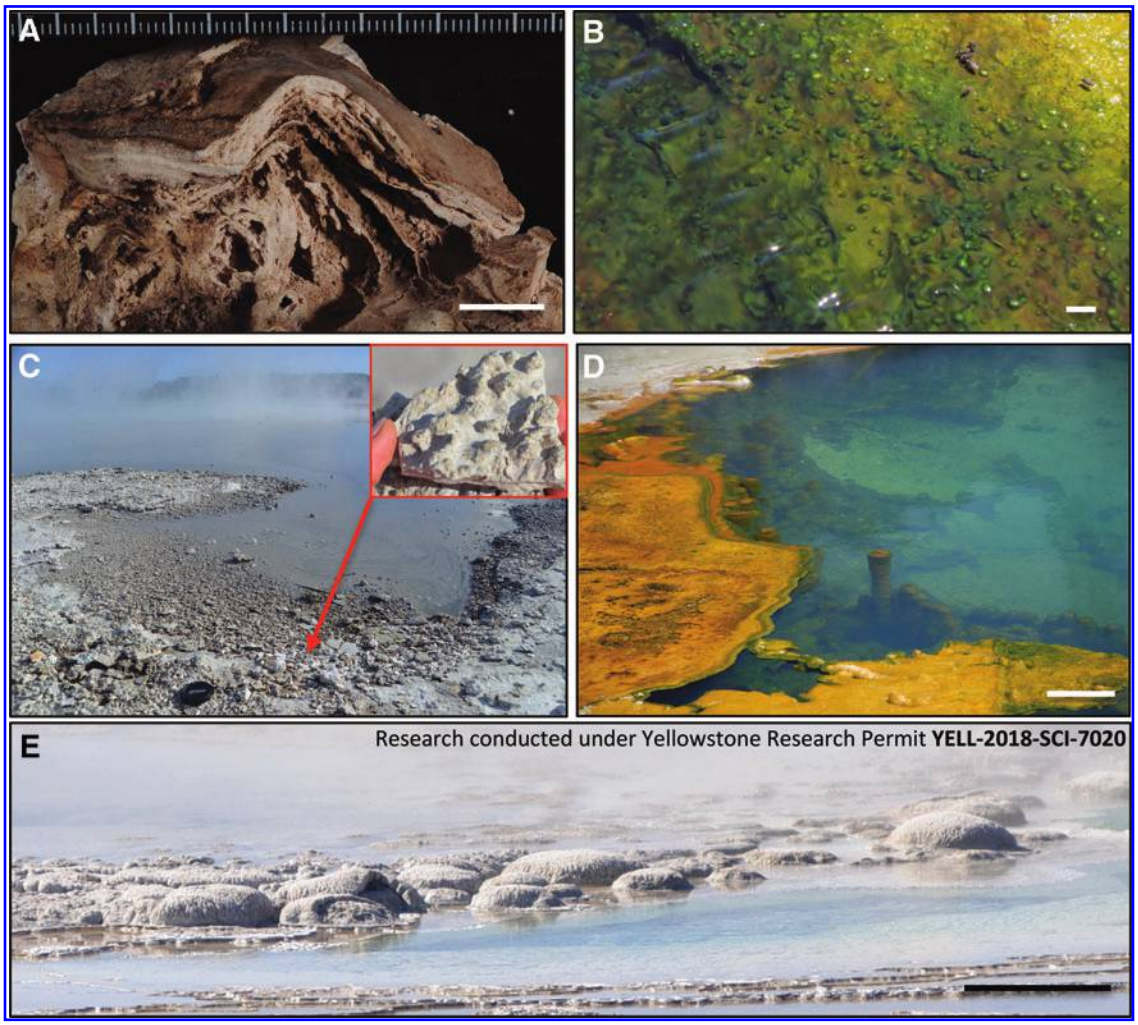

FIG. 25. Variety of stromatolite morphologies that occur in modern mid-apron pool facies of geothermal spring settings from NZ and YNP, USA. Scale bar measurements indicated. **(A)** Conical stromatolite from sinter buttress, Te Kopia, NZ (2 cm). **(B)** Pustular mats, Hot Water Creek, Waimangu Volcanic Valley, NZ (5 cm). **(C)** Pustular stromatolites, Lake Rotokawa shoreline, NZ. **(D)** Columnar stromatolites, Orakei Korako, NZ (20 cm). **(E)** Low, broad pustular domes at edge of Great Fountain Geyser, YNP (30 cm).

drying (caused by change in discharge channel direction or seasonal variations), or freeze-thaw (seasonal or diurnal), or faunal disruption. The breccia is subsequently coated by silica-rich hot spring waters within the mid-apron area (Hamilton *et al.*, 2019). This can occur relatively close to hot spring pools that intermittently discharge silica-rich water in between periods of mat growth and sinter brecciation (Guidry and Chafetz, 2003a). Primary porosity in sinter breccias is characteristic of microbial activity and may be caused by either accumulation of microbially produced gases and/or dissolution of organic matter.

8.2.2.2. Middle apron pool facies. Although the stratigraphically lowermost, and most widespread wrinkly laminated stromatolites may be related to hydrothermally fed marine or lacustrine evaporative basins, there is a variety of unique stromatolite morphologies in the upper stratigraphic levels of M2 that are consistent with formation in subaerial hot spring pool environments. These unique Dresser stromatolites are interbedded with hot spring deposits (Figs. 12, 15, 18, 19, and 20) and vary substantially over short lateral (*i.e.*, ~1–15 m) distances, for example, at site 24S.

Unique and variable stromatolite morphologies are consistent with middle apron facies of modern hot springs where stratiform, conical, pustular, columnar, and domical stromatolites are variably distributed over very short distances (10's of cm to m) (Fig. 25). Middle apron pool stromatolite facies are found on sinter terraces within, or at the edge of, mid-temperature pools, in hydrothermally influenced lakes, and/or in mid-apron channels (Walter *et al.*, 1972; Guido and Campbell, 2011; Hamilton *et al.*, 2019). Hot spring systems typically vary over months to years due to seasonal variations, plumbing blockage through cementation and/or tectonically influenced hydrodynamic fluctuations that cause channel migration on the apron or waning thermal fluid upflow (Fournier *et al.*, 1994; Guidry and Chafetz, 2003a; Soto *et al.*, 2019). These system fluctuations affect the buildup, or lack thereof, of microbially influenced deposits, which results in the highly variable and patchy distributions (Guidry and Chafetz, 2003a), as well as

deposits of broken-up, and resedimented mats (*e.g.*, EC-i and EC-ii).

The Fe-rich, shrub-like structures found at site 1S in DFc1 are morphologically identical to modern and fossil arborescent shrubby microbialites that form within travertine terrace pool deposits (Figs. 15C cf. 26E; Chafetz and Folk, 1984; Chafetz and Guidry, 1999; Guido and Campbell, 2017). This observation implies that the multiple horizons of Dresser shrub structures likely grew as shrubby microbialites within travertine terrace pools in mid- to distal apron areas. The local association of Dresser shrubs interbedded with sinter terracette deposits (Fig. 4; Djokic *et al.*, 2017) implies that fluid flow from nearby springs shifted between relatively deep terrace pools to relatively shallow terracettes. A well-studied modern example is that from Mammoth Hot Springs, Yellowstone National Park, where shrubs are found flooring terrace pond facies that variably shift in shape and depth across the local landscape (Fig. 26A–D; Pentecost, 1990; Fouke *et al.*, 2000).

Geyserite at the shrub locality (1S) supports a hot spring setting, and it has been documented that travertine and siliceous sinter can develop together in the same geothermal area (Smith *et al.*, 2010; Guido and Campbell, 2014).

Modern shrub morphology is indicated as resulting from bacterial clumping (Chafetz and Guidry, 1999) and typically shrubs are composed of thermogene carbonate (travertine). However, the final composition of shrubs can vary due to environmental factors, such as water chemistry, community composition, hydrothermal alteration, and/or diagenesis (*e.g.*, Guidry and Chafetz, 2003b; Guido and Campbell, 2017). In fact, shrub-like microbialites are known to exhibit variable compositions, for example, siliceous (Guidry and Chafetz, 2003b) and Mn- and Fe-rich (Chafetz *et al.*, 1998), as well as display variable diagenesis and silica replacement due to hydrothermal alteration (Guido and Campbell, 2017). Such factors may explain why the Dresser shrubs preserve both hematite and silica compositions (*e.g.*, Fig. 4A, B).

Tear mats in DFc1 are characterized by distinct rips, tears, or desiccation scars preserved on stromatolite bedding planes at site 24S (Fig. 18), where they closely underlie a deposit of EC-ii, which contains geyserite clasts. Tear structures and twisted, ropy morphology features of microbial mats in the mid-apron channel facies of modern hot springs form as a result of burst pockets of gas (*i.e.*, metabolic gas bubbles that accumulate between mat layers), periods of turbulent fluid discharge, and/or desiccation as spring flow ceases (Fig. 27; Guido and Campbell, 2009; Hamilton *et al.*, 2019).

8.2.3. Distal apron facies. Hot spring sinter terracettes with microbial palisade fabric were identified at locality 1S from their macroscopic and microscopic features (Djokic *et al.*, 2017). In Phanerozoic hot spring systems, vertically oriented microbial filaments lead to the development of palisade fabric on lithification, where they build up as terracettes along the mid- to distal hot spring apron (Campbell *et al.*, 2015b). Palisade fabric is commonly produced by cyanobacteria (*e.g.*, *Calothrix*) that cover distal areas of the sinter apron with brown to dark green mats, where water temperatures are <40°C and water depths are only a few mm (Cady and Farmer, 1996; Walter *et al.*, 1996; Guido and Campbell, 2011; Campbell *et al.*, 2015b). Given the antiquity of the Dresser Formation and its degree of recrystallization, we cannot conclude whether cyanobacteria formed

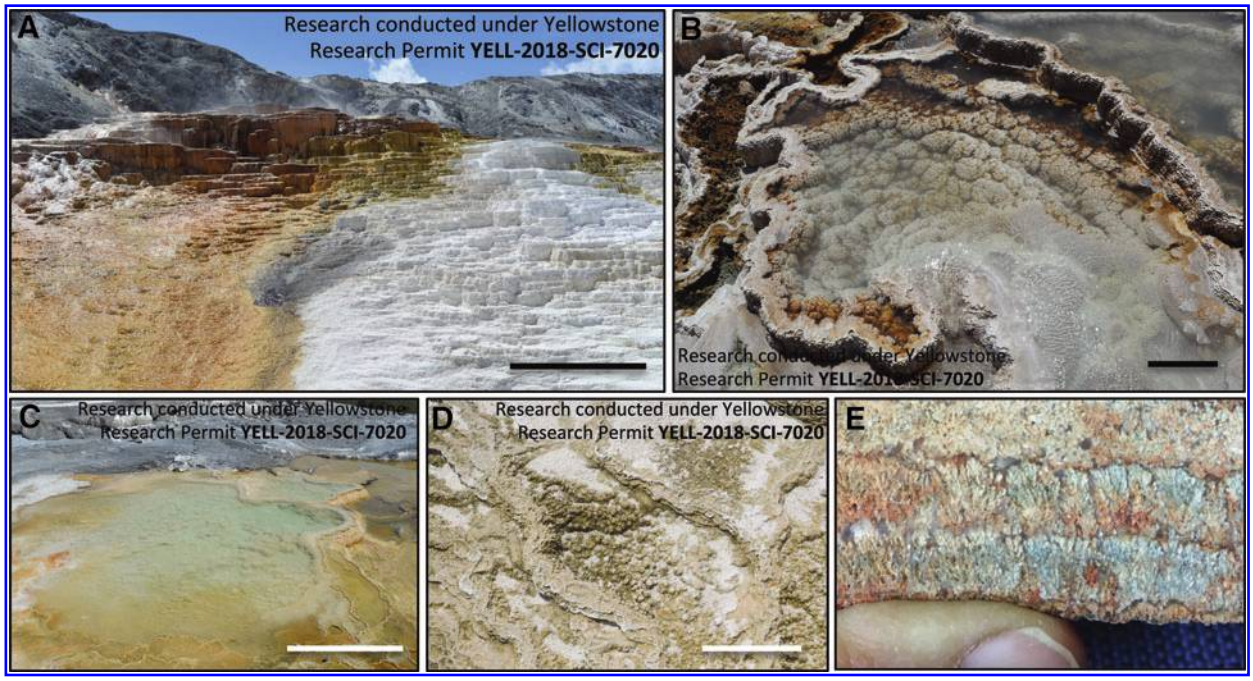

FIG. 26. Recent and modern travertine terrace deposits. Scale bar measurements indicated. **(A–D)** Mammoth Hot Springs, YNP, USA: **(A)** terrace slope. White area represents dried terrace. Orange and green areas of microbial growth are still exposed to spring discharge (1 m); **(B–D)** terrace pools with shrubs growing at their bases (**B**—25 cm; **C**—1 m; **D**–30 cm). **(E)** Hand sample of shrubs in Jurrasic travertine, El Macanudo, Argentina.

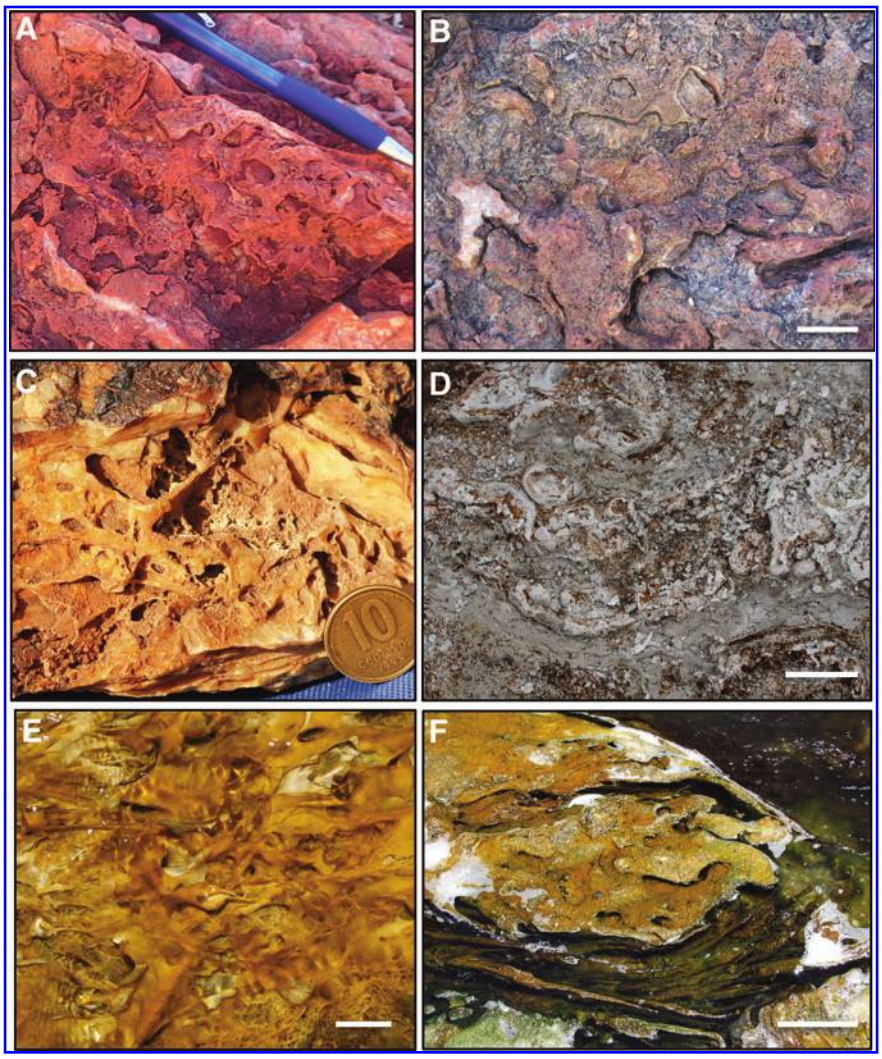

FIG. 27. Middle apron channel facies in ancient and Phanerozoic hot spring deposits. Scale bar measurements indicated. **(A,B)** Tear mat structures in the Dresser Formation (**B**—5 cm). **(C)** Jurassic wavy mat sinter, San Agustín, Argentine Patagonia. **(D)** Recent silicified microbial mat sinter, Orakei Korako, NZ (5 cm). **(E)** Formation of microbial mats under a few cm of water, NZ (2 cm). **(F)** Microbial mat buildup at edge of hydrothermally fed stream, Waimangu Volcanic Valley, NZ (25 cm).

the observed palisade fabric. However, the vertical arrangement suggests some form of phototrophy.

Rounded pebble to cobble conglomerate occupies thin (<20 cm), few-meter-wide channels at two (16N, 24S) of the three localities in DFc1 that contain known hot spring deposits. Although channelized pebble conglomerates can form in tidal flats (Reading, 2009), the abrupt lateral facies variations, association with strongly channelized EC deposits, and hot spring sinter (Fig. 16C) all point to a fluvial rather than a marine tidal and/or shoreline depositional environment. Recent studies have documented white silica pebble conglomerates encrusted by microbial laminates as a fluvial hot spring facies from Jurassic and Miocene deposits (Guido and Campbell, 2019). Although some of these pebbles show plastic deformation, which is unknown for the Dresser conglomerate, the paleoenvironment and thin, ferruginous layers inferred as microbial crusts draping the Dresser conglomerate are remarkably similar (Fig. 8B cf. Guido and Campbell, 2019).

8.2.4. Mineralized hot spring pools. Based on previous studies that are supported by results herein, it is suggested that at least some barite within DFc1 represents the mineralized remnants of subaerial hot spring pools (Djokic *et al.*, 2017), baritic travertine, and/or hydrothermal lake venting. The evidence is based on context, morphology, and an inferred origin from hydrothermal fluids (see also Van Kranendonk *et al.*, 2008).

All sites containing interpreted proximal hot spring vent facies (*e.g.*, geyserite at sites 16N, 1S and 23S) are located immediately above the tops of wide, deep (to avg. estimated 1 km) hydrothermal chert-barite veins (Supplementary Fig. S1). At the interfaces are large (to 10 m^2) barite masses displaying morphological features identical to those from mineralized vents of subaerial hot springs.

For example, the observation of curled masses of coarsely crystalline, isopachous barite layers that envelop wedges of overlying sedimentary rock (*e.g.*, locality 1S: Fig. 14C–F; Djokic *et al.*, 2017) is comparable to isopachous mineralization of subterranean hot spring cavities found on the edge of Lake Bogoria, Chemurkeu, Kenya Rift Valley (Renaut and Jones, 1997).

Angular blocks of bedded chert-barite filling an inferred subterranean hot spring conduit at sites 1S (Fig. 14C–F; Supplementary Fig. S2; Van Kranendonk, 2006: Fig. 13; Djokic *et al.*, 2017) and the barite gully are comparable to

collapse features that commonly occur along the rims of hot spring pools (Fig. 28).

Although rare, relatively small subaerial barite deposits have been documented from a variety of modern hot and cold springs (Cecile *et al.*, 1984; Bonny and Jones, 2008a, b). In these settings, the formation of barite may be restricted by the insolubility of barium in oxygenated fluids (*e.g.*, Bonny and Jones, 2008a), which have dominated Phanerozoic surface environments. In contrast, Archean fluid reservoirs would have been mainly anoxic, allowing for high concentrations of barium to be liberated from feldspars in volcanic rocks via hydrothermal leaching, and carried toward the surface (see Van Kranendonk and Pirajno, 2004).

When these fluids were supersaturated with Ba, and then exposed to sulfate, barite could precipitate (*e.g.*, Bonny and Jones, 2008b). The sheer volume of barite in the Dresser Formation (several million tons: Hickman, 1983) indicates that high volumes of Ba^{2+} and SO_4^{2-} were available.

Although the availability of Ba can be explained by reducing hydrothermal conditions, sulfate levels were generally vanishingly small in Earth's early oceans (Crowe *et al.*, 2014). In contrast, the high volume of barite in the Dresser Formation indicates an abundant source of sulfate, which may have derived from H_2SO_4 produced as a by-product of acid-sulfate, steam-heated alteration during deposition of the Dresser Formation (H_2S and/or SO_2 mixing with meteoric- or sea-water), and/or through photochemical oxidation of volcanogenic SO_2 (Fig. 29; Runnegar *et al.*, 2001; Van Kranendonk and Pirajno, 2004; Van Kranendonk, 2006; Van Kranendonk *et al.*, 2008). A more evolved (felsic) magmatic reservoir, as has been inferred for the Dresser Formation (Van Kranendonk *et al.*, 2008), could release a sufficient amount of SO_2 (Andres *et al.*, 1991), helping to explain the large volume of barite within the Dresser Formation.

Although the anoxic Archean volcanic-hydrothermal environment of the Dresser Formation was clearly conducive to forming large volumes of barite, the depositional history of barite precipitation remains complicated.

The formation of Dresser barite in a subaerial context is implied by evidence of mineralized hot spring pools (Figs. 14 and 28; Djokic *et al.*, 2017). In this scenario, mineralization could have occurred through precipitation of briny, volcanic lake waters into the hydrothermal plumbing of emergent hot spring pools that flank lake edges, such as exists in Lake Bogoria (Renaut and Jones, 1997).

In contrast, previous studies proposed that the barite precipitated within a collapsing caldera basin that was inundated by seawater (Van Kranendonk, 2006). The deeply penetrating nature of hydrothermal veins and large clearly intrusive deposits of barite within the Dresser Formation does imply voluminous fluid circulation, indicating the need for a large body of water such as a shallow sea or basin. In this scenario, once emerged hot spring pools become buried, or submerged under seawater, barite mineralizes the subsurface hot spring cavities through diagenetic processes.

The first scenario is supported by the fact that many Phanerozoic volcanic- hydrothermal lakes are flanked by compositionally varied deposits, for example, travertine (thermogene carbonate) or sinter (silica), which are often associated with stromatolites or microbial communities (Renaut and Jones, 1997; Kazmierczak and Kempe, 2006; Guido *et al.*, 2010; Guido and Campbell, 2012). Hydrothermal lake bottoms are also known to form compositionally diverse venting structures related to fluid chemistry (*e.g.*, Jones *et al.*, 2007; Guido and Campbell, 2012, 2014; Dekov *et al.*, 2014). Some barite structures documented elsewhere in the Dresser Formation have been suggested as possible vent structures, although such structures can also form in a shallow sea (Van Kranendonk, 2006).

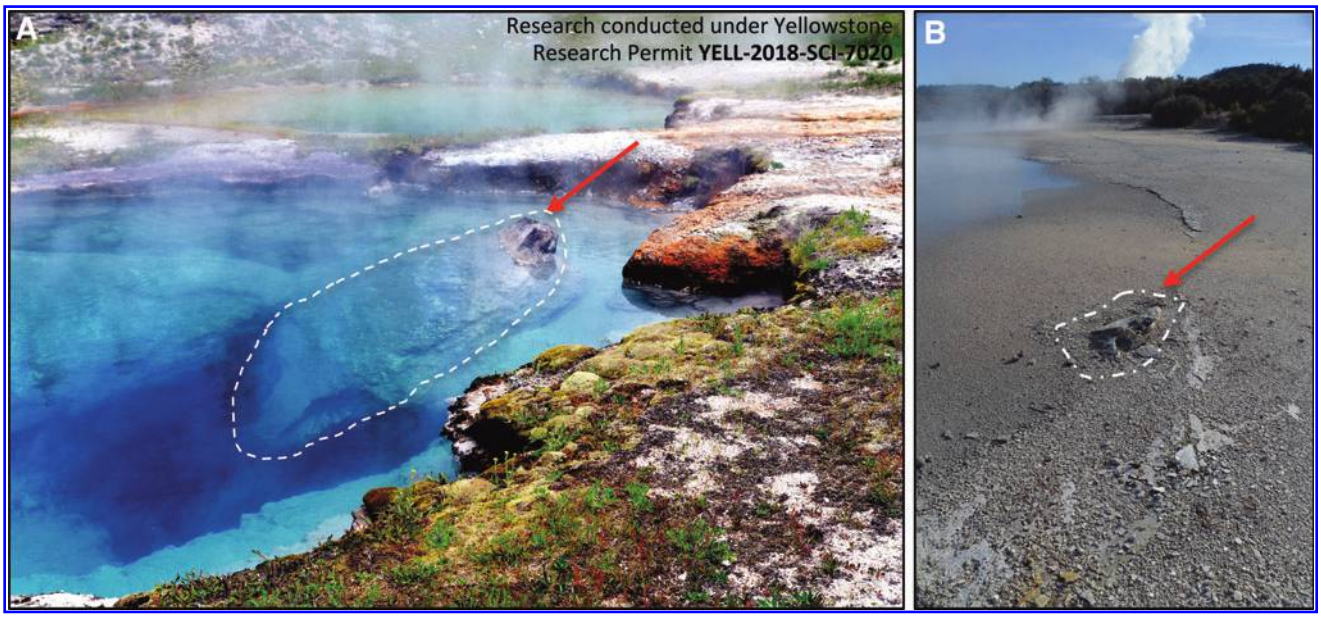

FIG. 28. Analogues for the onset of Dresser mineralized hot spring pools. **(A)** Collapsed block ($\sim$1.5 m long) from the edge of a hot spring pool, YNP, USA. **(B)** Edge of a hot spring pool that has collapsed at a once-active spring-pool edge, but now resedimentation has infilled around the collapsed edge and shifted the margin of the active spring, Rotokawa, NZ (collapsed edge protruding $\sim$50 cm).

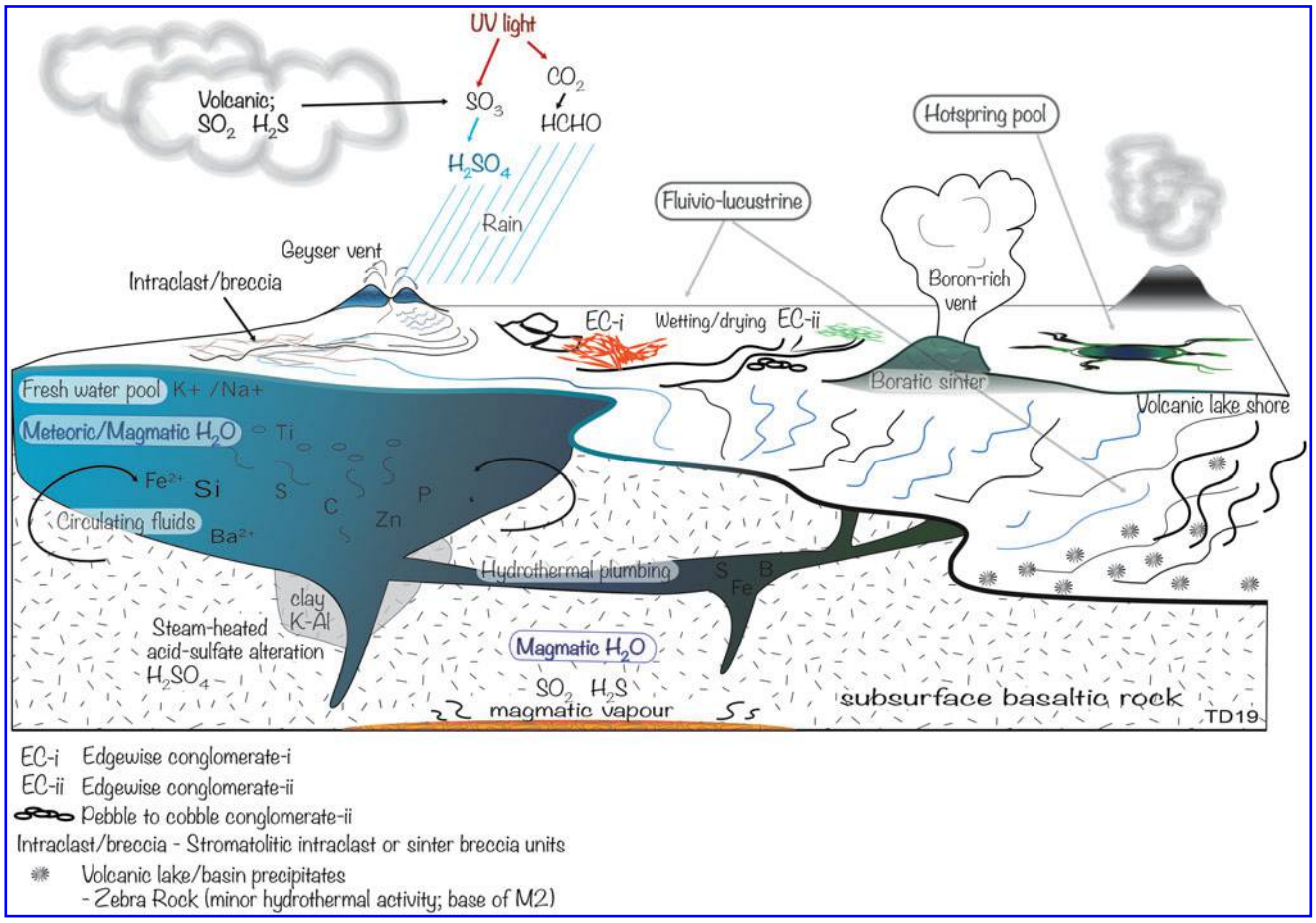

FIG. 29. Schematic diagram of the Dresser Formation hot spring model for M2 in DFc1 depicting the variety of hot spring-related facies. Inferred proximal vent (geysers and boratic springs) and mid- to distal apron (sinter breccia/intraclasts, packed fragmental deposits/edgewise) facies, including related fluvio-lacustrine settings.

Possibly, components of both settings may apply to the precipitation of barite. It has been well documented that barite in DFc1 did not form all at once but it entered in the system during multiple pulses (Van Kranendonk *et al.*, 2008). There could have been several rise-and-fall episodes of crust relative to sea level over time, both locally and regionally, given the intensity of block faulting across the area.

Therefore, although hot spring sites documented here (*e.g.*, sites 1S) show strong evidence for barite mineralizing the shallow subterranean feeders to subaerial geyserite-bearing springs (Figs. 14 and 28; Djokic *et al.*, 2017; *cf.* Renaut and Jones, 1997), further investigations are needed to contrain the depositional details of barite formation.

9. Conclusions

A geothermal field on an exposed land surface is inferred for at least part of M2 of the lower chert-barite sequence (DFc1) of the Dresser Formation (Fig. 29). This interpretation is based on a variety of local lithology within M2 that is consistent with proximal, middle, and distal portions of hot spring discharge aprons, as observed in Phanerozoic geothermal fields.

Key observations include:

(1) M2 deposits within DFc1 display abrupt lateral facies changes consistent with highly variable bio- and litho-facies distributions in modern hot springs, where the ever-changing geothermal environment controls depositional characteristics.

(2) The variety of hot spring deposits in the Dresser Formation, including geyserite and sinter terracettes that accompanied channelized edgewise and pebble conglomerate deposition, combined with a wide variety of stromatolite morphologies (*e.g.*, elongated, domical, conical, pustular, columnar), supports the interpretation that hot springs and associated riverine/fluvial deposits were inhabited by a diverse terrestrial microbial community at $\sim$3.5 Ga.

(3) All known hot spring deposits of the Dresser Formation are located immediately above the terminations of subsurface faults/fractures filled by black chert+barite hydrothermal veins. This is consistent with modern geothermal fields that are mostly situated on faults or fractures that act as conduits for hot, chemical-rich, fluids to reach the surface (Chafetz and Folk, 1984; Bignall and Browne, 1994; Guido and Campbell, 2011).

(4) The association of Dresser sinter terracettes with shrub-like microbialites is similar to travertine pool

deposits such as those from Mammoth Hot Springs, Yellowstone National Park (Pentecost, 1990).

(5) The association of geyserite and boron-rich (tourmaline-bearing) rip-up clasts, as well as the association of geyserite and possible travertine deposits, suggests that a variety of hot spring chemistries were present in DFc1 (*e.g.*, Campbell *et al.*, 2015a; Steller *et al.*, 2019).

(6) Textural and mineralogical data supporting the presence of geyserite in DFc1 are reinforced by REE + Y patterns, consistent with Phanerozoic hot spring deposits and inconsistent with modern and contemporaneous Archean marine precipitates.

Based on these results, a variety of fluid compositions can be inferred for the Dresser hot springs, including acidic (steam-heated acid-sulfate alteration; Van Kranendonk and Pirajno, 2004), alkaline (shrub-like microbialites and terracettes; Djokic *et al.*, 2017; this study), alkali-chloride (Harris *et al.*, 2009; Djokic *et al.*, 2017), and boron-rich compositions (cf. Van Kranendonk *et al.*, 2020).

Fluid chemistry likely varied both temporally and/or spatially, as it does in Phanerozoic systems that evolve through time. Collectively, lithostratigraphic data from the three widespread (sites are 3 km apart) hot spring sites identified in M2 illustrate the diverse nature and extensive distribution of an inhabited geothermal field in the ~3.5 Ga Dresser Formation.

The results presented here underscore the importance of a continued study of the early geological record for astrobiological research. In particular these findings reinforce the long-standing hypothesis that hydrothermal systems are optimal places to search for past life on Mars.

Acknowledgments

Many thanks are due to: the Yellowstone National Park staff and rangers; A. Greig for trace element analyses, Department of Earth Sciences, University of Melbourne. The authors thank K. Privat for technical assistance and use of facilities at the Electron Microscope Unit at UNSW. Trinity Hamilton is acknowledged for fieldwork support at Yellowstone National Park. K. Dadd and A. Gangadine are acknowledged for their support with petrographic imaging. Faye and Geoff Myers, and Haoma Mining provided kind hospitality and support on site. The authors also thank the reviewers for their feedback, which has improved the quality of this research.

Author Disclosure Statement

No competing financial interests exist.

Funding Information

This research was supported by the Australian Research Council Centre of Excellence for Core to Crust Fluids (CCFS), the Australian Research Council Discovery Project DP180103204, the Agouron Institute, the Australian Centre for Astrobiology (ACA), the PANGEA Research Centre, and The School of Biological, Earth and Environmental Sciences (BEES) at the University of New South Wales (UNSW). Student support for T.D. is acknowledged from the Australian Government Research Training Program Scholarship. K.A.C. acknowledges funding from the Royal Society of New Zealand, Marsden Fund. D.M.G. and K.A.C. acknowledge funding from a National Geographic Society field research grant. Yellowstone Research was conducted under Permit YELL-2018-SCI-7020.

Supplementary Material

Supplementary Figure S1
Supplementary Figure S2
Supplementary Figure S3
Supplementary Figure S4
Supplementary Figure S5
Supplementary Figure S6
Supplementary Figure S7
Supplementary Table S1
Supplementary Video S1
Supplementary Video S2

References

Allwood AC, Kamber BS, Walter MR, *et al.* (2010) Trace elements record depositional history of an Early Archean stromatolitic carbonate platform. *Chem Geol* 270:148–163.

Allwood AC, Walter MR, Kamber BS, *et al.* (2006) Stromatolite reef from the Early Archaean era of Australia. *Nature* 441:714–718.

Andres RJ, Rose WI, Kyle PR, *et al.* (1991) Excessive sulfur dioxide emissions from Chilean volcanoes. *J Volcanol Geotherm Res* 46:323–329.

Babechuck M, Kamber BS, Greig A, *et al.* (2010) The behavior of tungsten during mantle melting revisited with implications for planetary differentiation time scales. *Geochim Cosmochim Acta* 74:1448–1470.

Barley ME (1993) Volcanic, sedimentary and tectonostratigraphic environments of the ~3.46 Ga Warrawoona Megasequence: a review. *Precambrian Res* 60:47–67.

Baumgartner RJ, Van Kranendonk MJ, Wacey D, *et al.* (2019a) Nano-porous pyrite and organic matter in 3.5-billion-year-old stromatolites record primordial life. *Geology* 47: 1039–1043.

Bignall G and Browne PRL (1994) Surface hydrothermal alteration and evolution of the Te Kopia thermal area, New Zealand. *Geothermics* 23:645–658.

Bolhar R, Van Kranendonk MJ, and Kamber BS (2005) A trace element study of siderite– jasper banded iron formation in the 3.45 Ga Warrawoona Group, Pilbara Craton—formation from hydrothermal fluids and shallow seawater. *Precambrian Res* 137:93–114.

Bonny SM and Jones B (2008a) Petrography and textural development of inorganic and biogenic lithotypes in a relict barite tufa deposit at Flybye Springs, NT, Canada. *Sedimentology* 55:275–303.

Bonny SM and Jones B (2008b) Controls on the precipitation of barite (BaSO4) crystals in calcite travertine at Twitya Spring, a warm sulphur spring in Canada's Northwest Territories. *Sediment Geol* 203:36–53.

Browne P and Lawless J (2001) Characteristics of hydrothermal eruptions, with examples from New Zealand and elsewhere. *Earth-Sci Rev* 52:299–331.

Buick R (1985) Life and conditions in the early Archaean: evidence from 3500 M.Y. old shallow-water sediments in the Warrawoona Group, North Pole, Western Australia. Un-

published Doctor of Philosophy thesis, Department of Geology, University of Western Australia.

Buick R and Dunlop JSR (1990) Evaporitic sediments of Early Archaean age from the Warrawoona Group, North Pole, Western Australia. *Sedimentology* 37:247–277.

Buick R, Dunlop JSR, and Groves DI (1981) Stromatolite recognition in ancient rocks: an appraisal of irregularly laminated structures in an Early Archaean chert-barite unit from North Pole, Western Australia. *Alcheringa* 5:161–181.

Cady SL and Farmer JD (1996) Fossilization processes in siliceous thermal springs: trends in preservation along thermal gradients. In *Evolution of Hydrothermal Ecosystems on Earth (and Mars?)*, edited by GR Bock and GA Goode. Proceedings of the Ciba Foundation Symposium 202. J. Wiley, Chichester, pp 150–173.

Campbell KA, Buddle TF, and Browne PRL (2004) Late Pleistocene siliceous sinter associated with fluvial, lacustrine, volcaniclastic and landslide deposits at Tahunaatara, Taupo Volcanic Zone, New Zealand. *Earth Environ Sci Trans R Soc Edinburgh* 94:485–501.

Campbell KA, Guido DM, Gautret P, *et al.* (2015a) Geyserite in hot-spring siliceous sinter: window on Earth's hottest terrestrial (paleo) environment and its extreme life. *Earth-Sci Rev* 148:44–64.

Campbell KA, Lynne BY, Handley KM, *et al.* (2015b) Tracing biosignature preservation of geothermally silicified microbial textures into the geological record. *Astrobiology* 15:858–882.

Canet C, Prol-Ledesma RM, Torres-Alvarado I, *et al.* (2005) Silica-carbonate stromatolites related to coastal hydrothermal venting in Bahía Concepción, Baja California Sur, Mexico. *Sediment Geol* 174:97–113.

Cangemi M, Bellanca A, Borin S, *et al.* (2010) The genesis of actively growing siliceous stromatolites: evidence from Lake Specchio di Venere, Pantelleria Island, Italy. *Chem Geol* 276: 318–330.

Cecile M, Goodfellow W, Jones L, *et al.* (1984) Origin of radioactive barite sinter, Flybye springs, Northwest Territories, Canada. *Can J Earth Sci* 21:383–395.

Chafetz HS, Akdim B, Julia R, *et al.* (1998) Mn and Fe-rich black travertine shrubs: bacterially (and nanobacterially) induced precipitates. *J Sediment Res* 68:404–412.

Chafetz HS and Folk RL (1984) Travertines: depositional morphology and the bacterially constructed constituents. *J Sediment Res* 54:289–316.

Chafetz HS and Guidry SA (1999) Bacterial shrubs, crystal shrubs, and ray-crystal shrubs: bacterial vs. abiotic precipitation. *Sediment Geol* 126:57–74.

Christenson B, Németh K, Rouwet D, *et al.* (2015) *Volcanic Lakes*. Springer, Berlin, Heidelberg.

Christiansen RL (2001) The quaternary and pliocene yellowstone plateau volcanic field of Wyoming, Idaho, and Montana. Professional Paper 729-G, USGS, pp 120.

Crowe SA, Paris G, Katsev S, *et al.* (2014) Sulfate was a trace constituent of Archean seawater. *Science* 346:735–739.

Currie AE (2005) Prokaryotic communities of geyserite deposits surrounding a high temperature alkali chloride hot spring. Unpublished Master of Science Thesis, The University of Auckland.

Dawson JB (2008) *The Gregory Rift Valley and Neogene-Recent Volcanoes of Northern Tanzania*. Geological Society, London, Memoirs: 33.

Dekov VM, Lalonde SV, Kamenov GD, *et al.* (2015) Geochemistry and mineralogy of a silica chimney from an inactive seafloor hydrothermal field (East Pacific Rise, 18°S). *Chem Geol* 415:126–140.

Dekov V, Egueh N, Kamenov G, *et al.* (2014) Hydrothermal carbonate chimneys from a continental rift (Afar Rift): Mineralogy, geochemistry, and mode of formation. *Chem Geol* 387:87–100.

Djokic T (2015) Assessing the link between Earth's earliest convincing evidence of life and hydrothermal fluids: The c. 3.5 Ga Dresser Formation of the North Pole Dome, Pilbara Craton, Western Australia. Unpublished Master of Philosophy thesis. School of Biological, Earth and Environmental Sciences, The University of New South Wales.

Djokic T and Van Kranendonk MJ (2018) Textural biosignatures from the Pilbara: an important benchmark for early life on Earth. *PalZ* 92:1–3.

Djokic T, Van Kranendonk MJ, Campbell KA, *et al.* (2017) Earliest signs of life on land preserved in ca. 3.5 Ga hot spring deposits. *Nat Commun* 8:15263.

Douville E, Bienvenu P, Charlou JL, *et al.* (1999) Yttrium and rare earth elements in fluids from various deep-sea hydrothermal systems. *Geochim Cosmochim Acta* 63:627–643.

Drake BD, Campbell KA, Rowland JV, *et al.* (2014) Evolution of a dynamic paleo-hydrothermal system at Mangatete, Taupo Volcanic Zone, New Zealand. *J Volcanol Geoth Res* 282:19–35.

Dunlop J, Milne V, Groves D, *et al.* (1978) A new microfossil assemblage from the Archaean of Western Australia. *Nature* 274:676–678.

Eggins SM, Woodhead JD, Kinsley LPJ, *et al.* (1997) A simple method for the precise determination of ≥40 trace elements in geological samples by ICPMS using enriched isotope internal standardization. *Chem Geol* 134:311–326.

Elderfield HJ (1988) The oceanic chemistry of the rare-earth elements. *Phil Trans R Soc London* 325:105–126.

Ewers GR, Wood DG, Tedder IJ, *et al.* (1992) Epithermal gold mineralisation in the northern Drummond Basin, Queensland. Australian Geological Survey Organisation, Minerals and Land Use Program, Record, 1992/72, p 67.

Fouke BW, Farmer JD, Des Marais DJ, *et al.* (2000) Depositional facies and aqueous-solid geochemistry of travertine-depositing hot springs (Angel Terrace, Mammoth Hot Springs, Yellowstone National Park, USA). *J Sediment Res* 70:565–585.

Fournier RO, Christensen RL, Hutchinson RA, *et al.* (1994) A field-trip guide to Yellowstone National Park, Wyoming, Montana, and Idaho—volcanic, hydrothermal, and glacial activity in the region. *US Geol Surv Bull* 2099:1–46.

Ghosh W, Mallick S, Haldar PK, *et al.* (2012) Molecular and cellular fossils of a mat-like microbial community in geothermal boratic sinters. *Geomicrobiol J* 29:879–885.

Greaves MJ, Elderfield H, and Klinkhammer GP (1989) Determination of the rare earth elements in natural waters by isotope-dilution mass spectrometry. *Anal Chim Acta* 218: 265–280.

Groves DI, Dunlop JS, and Buick R (1981) An early habitat of life. *Sci Am* 245:64–73.

Guido DM and Campbell KA (2009) Jurassic hot-spring activity in a fluvial setting at La Marciana, Patagonia, Argentina. *Geol Mag* 146:617–622.

Guido DM and Campbell KA (2011) Jurassic hot spring deposits of the Deseado Massif (Patagonia, Argentina): char-

acteristics and controls on regional distribution. *J Volcanol Geoth Res* 203:35–47.

Guido DM and Campbell KA (2012) Diverse subaerial and sublacustrine hot spring settings of the Cerro Negro epithermal system (Jurassic, Deseado Massif). Patagonia, Argentina. *J Volcanol Geoth Res* 229:1–12.

Guido DM and Campbell KA (2014) A large and complete Jurassic geothermal field at Claudia, Deseado Massif, Santa Cruz, Argentina. *J Volcanol Geoth Res* 275:61–70.

Guido DM and Campbell KA (2017) Upper Jurassic travertine at El Macanudo, Argentine Patagonia: a fossil geothermal field modified by hydrothermal silicification and acid overprinting. *Geol Mag* 155:1394–1412.

Guido DM and Campbell KA (2019) Plastic silica conglomerate with an extremophile microbial matrix in a hot-water stream paleoenvironment. *Astrobiology* 19:1433–1441.

Guido DM, Channing A, Campbell KA, *et al.* (2010) Jurassic geothermal landscapes and fossil ecosystems at San Agustín, Patagonia, Argentina. *J Geol Soc* 167:11–20.

Guidry SA and Chafetz HS (2003a) Anatomy of siliceous hot springs: examples from Yellowstone National Park, Wyoming, USA. *Sediment Geol* 157:71–106.

Guidry SA and Chafetz HS (2003b) Siliceous shrubs in hot springs from Yellowstone National Park, Wyoming, USA. *Can J Earth Sci* 40:1571–1583.

Hamilton AR, Campbell KA, and Guido DM (2019) Atlas of siliceous hot spring deposits (sinter) and other silicified surface manifestations in epithermal environments. Lower Hutt (NZ): GNS Science. GNS Science report 2019/06, 56 p. DOI: 10.21420/BQDR-XQ16.

Harris AC, White NC, McPhie J, *et al.* (2009) Early Archean hot springs above epithermal veins, North Pole, Western Australia: new insights from fluid inclusion microanalysis. *Econ Geol* 104:793–814.

Haymon RM, Kastner MJE, and Letters PS (1981) Hot spring deposits on the East Pacific Rise at 21 N: preliminary description of mineralogy and genesis. *Earth Planet Sci Lett* 53: 363–381.

Heller PL, Beland PE, Humphrey NF, *et al.* (2001) Paradox of downstream fining and weathering-rind formation in the lower Hoh River, Olympic Peninsula, Washington. *Geology* 29:971–974.

Hickman AH (1983) *Geology of the Pilbara Block and its environs. Geological Survey of Western Australia, Bulletin*, 127.

Hickman AH (1984) Archean diapirism in the Pilbara block, Western Australia. In *Precambrian Tectonics Illustrated*, edited by A Kröner, and R Greiling. E. Schweizwe-bartsche Verlagsbuch-handlung, Stuttgart, pp 113–127.

Hinman NW and Walter MR (2005) Textural preservation in siliceous hot spring deposits during early diagenesis: examples from Yellowstone National Park and Nevada, USA. *J Sediment Res* 75:200–215.

Hocking RM and Cockbain AE (1990) *Regolith. Geology and mineral resources of Western Australia. Western Australia Geological Survey Memoir* 3, pp 591–602.

Hopf S (1993) Behaviour of rare earth elements in geothermal systems of New Zealand. *J Geochem Explor* 47: 333–357.

Jahnert RJ and Collins LB (2012) Characteristics, distribution and morphogenesis of subtidal microbial systems in Shark Bay, Australia. *Mar Geol* 303:115–136.

Jones B and Renaut RW (1997) Formation of silica oncoids around geysers and hot springs at El Tatio, northern Chile. *Sedimentology* 44:287–304.

Jones B and Renaut RW (2003) Hot spring and geyser sinters: the integrated product of precipitation, replacement, and deposition. *Can J Earth Sci* 40:1549–1569.

Jones B and Renaut RW (2012) Facies architecture in depositional systems resulting from the interaction of acidic springs, alkaline springs, and acidic lakes: case study of Lake Roto-a-Tamaheke, Rotorua, New Zealand. *Can J Earth Sci* 49:1217–1250.

Jones B, De Ronde CEJ, Renaut RW, *et al.* (2007) Siliceous sublacustrine spring deposits around hydrothermal vents in Lake Taupo, New Zealand. *J Geol Soc* 164:227–242.

Kamber BS, Greig A, Schoenberg R, *et al.* (2003) A refined solution to Earth's hidden niobium: implications for evolution of continental crust and mode of core formation. *Precambrian Res* 126:289–308.

Kamber BS, Greig A, and Collerson KD (2005) A new estimate for the composition of weathered young upper continental crust from alluvial sediments, Queensland, Australia. *Geochim Cosmochim Acta* 69:1041–1058.

Kazmierczak J and Kempe S (2006) Genuine modern analogues of Precambrian stromatolites from caldera lakes of Niuafo'ou Island, Tonga. *Naturwissenschaften* 93:119–126.

Kelley DS, Baross JA, and Delaney JR (2002) Volcanoes, fluids, and life at mid-ocean ridge spreading centers. *Ann Rev Earth Planet Sci* 30:385–491.

Kremer B, Kazmierczak J, Łukomska-Kowalczyk M, *et al.* (2012) Calcification and silicification: fossilization potential of cyanobacteria from stromatolites of Niuafo 'ou's Caldera Lakes (Tonga) and implications for the early fossil record. *Astrobiology* 12:535–548.

Lewis AJ, Palmer MR, Sturchio NC, *et al.* (1997) The rare earth element geochemistry of acid-sulphate and acid-sulphate-chloride geothermal systems from Yellowstone National Park, Wyoming, USA. *Geochim Cosmochim Acta* 61:695–706.

Lindsay JF, Brasier MD, McLoughlin N, *et al.* (2005) The problem of deep carbon—an Archaean paradox. *Precambrian Res* 143:1–22.

Lynne BY and Campbell KA (2004) Morphologic and mineralogic transitions from opal-A to opal-CT in siliceous sinter diagenesis, Taupo Volcanic Zone, New Zealand. *J Sediment Res* 74:561–579.

Martin H, Smithies R, Rapp R, *et al.* (2005) An overview of adakite, tonalite–trondhjemite–granodiorite (TTG), and sanukitoid: relationships and some implications for crustal evolution. *Lithos* 79:1–24.

Mason B and Moore C (1966) *Principles of Geochemistry*. John Wiley and Sons, New York.

McLennan SM (1989) Rare earth elements in sedimentary rocks: Influence of provenance and sedimentary processes. *Geochemistry and Mineralogy of Rare Earth Elements, Reviews in Mineralogy* 21:169–200.

Nijman W, de Bruijne K, and Valkering ME (1999) Growth fault control of Early Archaean cherts, barite mounds and chert-barite veins, North Pole Dome, Eastern Pilbara, Western Australia. *Precambrian Res* 95:247–274.

Otálora F, Mazurier A, García-Ruiz JM, *et al.* (2018) A crystallographic study of crystalline casts and pseudomorphs from the 3.5 Ga Dresser Formation, Pilbara Craton (Australia). *J Appl Crystallogr* 51:1050–1058.

Pentecost A (1990) The formation of travertine shrubs: Mammoth Hot Springs, Wyoming. *Geol Mag* 127:159–168.

Peryt TM (2012) *Coated Grains*. Springer-Verlag, Berlin.

Philippot P, Van Zuilen M, Lepot K, *et al.* (2007) Early Archaean microorganisms preferred elemental sulfur, not sulfate. *Science* 317:1534–1537.

Pirajno F (2009) *Hydrothermal Processes and Mineral Systems*. Springer, Dordrecht, Netherlands.

Poole GH (2013) Modeling hydrothermal alteration facies of earth's oldest hydrothermal setting: the 3.5 Ga North Pole Dome, Western Australia. Unpublished Honours thesis, School of Biological, Earth & Environmental Sciences, The University of New South Wales, Sydney, Australia.

Power JF, Carere CR, Lee CK, *et al.* (2018) Microbial biogeography of 925 geothermal springs in New Zealand. *Nat Commun* 9:2876.

Reading HG (2009) *Sedimentary Environments: Processes, Facies and Stratigraphy*. John Wiley & Sons, Chichester.

Renaut RW and Jones B (1997) Controls on aragonite and calcite precipitation in hot spring travertines at Chemurkeu, Lake Bogoria, Kenya. *Can J Earth Sci* 34:801–818.

Renaut RW and Owen RB (1988) Opaline cherts associated with sublacustrine hydrothermal springs at Lake Bogoria, Kenya Rift Valley. *Geology* 16:699–702.

Renaut R, Jones B, Tiercelin J-J, *et al.* (2002) Sublacustrine precipitation of hydrothermal silica in rift lakes: evidence from Lake Baringo, central Kenya Rift Valley. *Sediment Geol* 148:235–257.

Rodgers KA, Browne PRL, Buddle TF, *et al.* (2004) Silica phases in sinters and residues from geothermal fields of New Zealand. *Earth Sci Rev* 66:1–61.

Ruff SW and Farmer JD (2016) Silica deposits on Mars with features resembling hot spring biosignatures at El Tatio in Chile. *Nat Commun* 7:13554.

Ruff SW, Campbell KA, Van Kranendonk MJ, *et al.* (2020) The case for ancient hot springs in Gusev Crater, Mars. *Astrobiology* 20:000-000.

Runnegar B, Dollase WA, Ketcham RA, *et al.* (2001) Early Archean sulfates from Western Australia first formed as hydrothermal barites not gypsum evaporates. [abstract 166-0]. In *GSA Annual Meeting*, Boston, Massachusetts.

Shen Y, Farquhar J, Masterson A, *et al.* (2009) Evaluating the role of microbial sulfate reduction in the early Archean using quadruple isotope systematics. *Earth Planet Sci Lett* 279: 383–391.

Sillitoe RH (1993) Epithermal models: genetic types, geometrical controls and shallow features. In *Mineral Deposit Modeling*, edited by RV Kirkham, WD Sinclair, RI Thorpe, and JM Duke. Special Paper of the Geological Association of Canada 40, pp 403–417.

Sillitoe RH (2015) Epithermal paleosurfaces. *Miner Deposita* 50:767–793.

Skok J, Mustard J, Ehlmann B, *et al.* (2010) Silica deposits in the Nili Patera caldera on the Syrtis Major volcanic complex on Mars. *Nat Geosci* 3:838.

Smith DJ, Jenkin GRT, Naden J, *et al.* (2010) Anomalous alkaline sulphate fluids produced in a magmatic hydrothermal system—Savo, Solomon Islands. *Chem Geol* 275: 35–49.

Smithies RH, Champion DC, and Van Kranendonk MJ (2007) The oldest well-preserved volcanic rocks on Earth: geochemical clues to the early evolution of the Pilbara Supergroup and implications for the growth of a Paleoarchean continent. In *Earth's Oldest Rocks*, edited by MJ Van Kranendonk, RH Smithies, and V Bennet. *Developments in Precambrian Geology, Vol. 15*, Elsevier, Amsterdam, pp 339–367.

Soto MF, Hochstein MP, Campbell K, *et al.* (2019) Sporadic and waning hot spring activity in the Tokaanu Domain, Hipaua-Waihi-Tokaanu geothermal field, Taupo Volcanic Zone, New Zealand. *Geothermics* 77:288–303.

Steller LH, Nakamura E, Ota T, *et al.* (2020) Boron isotopes in the Puga Geothermal System, India, and their implications for the habitat of early life. *Astrobiology* 20:000–000.

Sun ZL, Zhou HY, Yang QH, *et al.* (2012) Growth model of a hydrothermal low-temperature Si-rich chimney: example from the CDE hydrothermal field, Lau Basin. *Sci China Earth Sci* 55:1716–1730.

Tadbiri S (2017) Structural and kinematic analysis of the 3.5 Ga hydrothermal chert- barite vein network of the stromatolitic Dresser Formation, North Pole Dome, Western Australia. Unpublished Master of Philosophy thesis, School of Biological, Earth and Environmental Sciences, The University of New South Wales.

Tămaș ClG and Milési J-P (2003) Hydrothermal breccia pipe structures: general features and genetic criteria-II Phreatic breccia. Studia UBB, *Geologia* 48:55–66.

Taylor SR and McLennan SM (1985) The continental crust: Its composition and evolution. Oxford, Blackwells Scientific.

Teece B, George SC, Djokic T, *et al.* (2020) Biomolecules from fossilized hot spring sinters: implications for the search for life on Mars. Astrobiology 20:000-000.

Trewin NH (1996) The Rhynie cherts: an early Devonian ecosystem preserved by hy- drothermal activity. In *Evolution of Hydrothermal Ecosystems on Earth (and Mars?)*, edited by GR Bock, and GA Goode. Proceedings of the Ciba Foundation Symposium 202. J. Wiley, Chichester, pp 131–145.

Ueno Y, Yamada K, Yoshida N, *et al.* (2006) Evidence from fluid inclusions for microbial methanogenesis in the early Archaean era. *Nature* 440:516–519.

Uysal IT, Gasparon M, Bolhar R, *et al.* (2011) Trace element composition of near-surface silica deposits—a powerful tool for detecting hydrothermal mineral and energy resources. *Chem Geol* 280:154–169.

Van Kranendonk MJ (2000) *Geology of the North Shaw 1: 100 000 Sheets: Sheets 2755*. Geological Survey of Western Australia.

Van Kranendonk MJ (2006) Volcanic degassing, hydrothermal circulation and the flourishing of early life on Earth: a review of the evidence from c. 3490-3240 Ma rocks of the Pilbara Supergroup, Pilbara Craton, Western Australia. *Earth Sci Rev* 74:197–240.

Van Kranendonk MJ (2011a) Morphology as an indicator of biogenicity for 3.5-3.2 Ga fossil stromatolites from the Pilbara Craton, Western Australia. In *Advances in Stromatolite Geobiology*, edited by J Reitner, N-V Quéric, and G Arp. Springer-Verlag Berlin Heidelberg, pp 537–554.

Van Kranendonk MJ and Pirajno F (2004) Geochemistry of metabasalts and hydrothermal alteration zones associated with c. 3.45 Ga chert and barite deposits: implications for the geological setting of the Warrawoona Group, Pilbara Craton, Australia. *Geochem Explor Environ Anal* 4:253–278.

Van Kranendonk MJ, Webb GE, and Kamber BS (2003) Geological and trace element evidence for a marine sedimentary environment of deposition and biogenicity of 3.45

Ga stromatolitic carbonates in the Pilbara Craton, and support for a reducing Archaean ocean. *Geobiology* 1:91–108.

Van Kranendonk MJ, Hickman A, and Smithies RH (2007) The East Pilbara Terrane of the Pilbara Craton, Western Australia: Formation of a continental nucleus through repeated mantle plume magmatism. In *Earth's Oldest Rocks*, edited by MJ Van Kranendonk, RH Smithies, and V Bennet. Elsevier, Amsterdam, pp 307–337.

Van Kranendonk MJ, Philippot P, Lepot K, *et al.* (2008) Geological setting of Earth's oldest fossils in the ca. 3.5Ga Dresser Formation, Pilbara Craton, Western Australia. *Precambrian Res* 167:93–124.

Van Kranendonk MJ, Djokic T, Poole G, *et al.* (2018) Depositional setting of the fossiliferous, c. 3480 Ma Dresser Formation, Pilbara Craton: a review. In Earth's Oldest Rocks, edited by MJ Van Kranendonk, V Bennett, and E Hoffmann. Elsevier, USA, pp 985–1006.

Van Kranendonk MJ, Baumgartner RJ, Djokic T, *et al.* (2020). Elements for the origin of life on land: A deep-time perspective from the Pilbara Craton of Western Australia. *Astrobiology* 20.

Wacey D, Noffke N, Saunders M, *et al.* (2018) Volcanogenic pseudo-fossils from the ~3.48 Ga Dresser Formation, Pilbara, Western Australia. *Astrobiology* 18:539–555.

Walter MR, editor (1976) *Stromatolites: Developments in Sedimentology, Vol. 20*. Elsevier, Amsterdam.

Walter MR, Bauld J, and Brock TD (1972) Siliceous algal and bacterial stromatolites in hot spring and geyser effluents of Yellowstone National Park. *Science* 178:402–405.

Walter MR, Buick R, and Dunlop JSR (1980) Stromatolites, 3400–3500 Myr old from the North Pole area, Western Australia. *Nature* 284:443–445.

Walter MR, Des Marais D, Farmer JD, *et al.* (1996) Lithofacies and biofacies of mid-Paleozoic thermal spring deposits in the Drummond Basin, Queensland, Australia. *Palaios* 11:497–518.

Walter M, McLoughlin S, Drinnan A, *et al.* (1998) Palaeontology of Devonian thermal spring deposits, Drummond basin, Australia. *Alcheringa* 22:285–314.

Watts-Henwood N, Campbell KA, Lynne BY, *et al.* (2017) Snapshot of hot-spring sinter at Geyser Valley, Wairakei, New Zealand, following anthropogenic drawdown of the geothermal reservoir. *Geothermics* 68:94–114.

Wilson CJ and Rowland JV (2016) The volcanic, magmatic and tectonic setting of the Taupo Volcanic Zone, New Zealand, reviewed from a geothermal perspective. *Geothermics* 59: 168–187.

Weed WH (1889) On the formation of siliceous sinter by the vegetation of thermal springs. *Am J Sci* 37:351–359.

White DE, Thompson GA, and Sandberg CH (1964) Rocks, structure, and geologic history of Steamboat Springs thermal area, Washoe County, Nevada. *U.S. Geol Surv Prof Paper* 458-B, 63.

Address correspondence to:
Tara Djokic
Australian Centre for Astrobiology
PANGEA Research Centre
School of Biological, Earth and Environmental Sciences
University of New South Wales
Kensington 2052
New South Wales
Australia

E-mail: tara.djokic@unswalumni.com

Submitted 20 March 2019
Accepted 3 March 2020

Abbreviations Used

Ba = barite
br = branch
Cp = clumped stubby pustules
EC = edgewise conglomerate
EDS = energy dispersive spectroscopy
EMP-WDS = electron microprobe-wavelength dispersive spectroscopy
EMU = Electron Microscopy Unit
EPS = exopolymeric substance
Lc = layered columnar
M1–M4 = members 1–4
MOR = mid-ocean ridge
MUQ = Mud of Queensland
NPD = North Pole Dome
PAAS = Post-Archean Average Shale
ppl = plane polarized light
REE+Y = rare earth element and yttrium
SEM = scanning electron microscopy
xpl = crossed polarized light
YNP = Yellowstone National Park

This article has been cited by:

1. Brian Jones, Robin W. Renaut. 2021. Multifaceted incremental growth of a geyser discharge apron – evidence from Geysir, Haukadalur, Iceland. *Sedimentary Geology* **58A**, 105905. [Crossref]